Current-Induced Crystallisation in Heusler Alloy Films for Memory Potentiation in Neuromorphic Computation

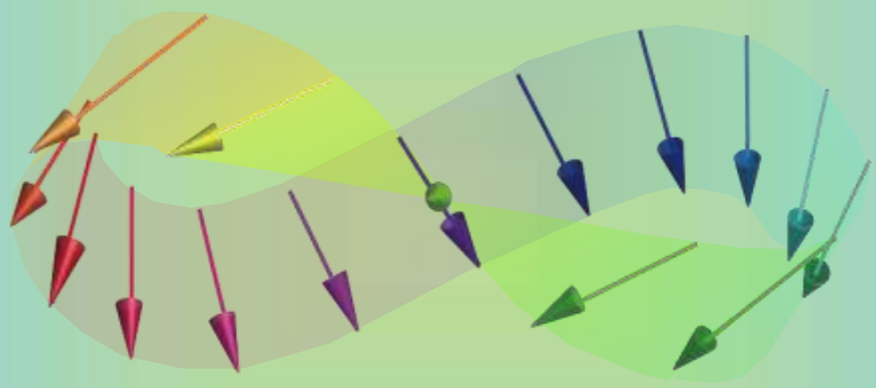

W. Frost,[1] K. Elphick,[1] M. Samiepour,[1] Z. Zhou,[1]
D. C. Lloyd,[1] T. Seki,[2] T. Kubota,[2] R. Ramos,[2]
E. Saitoh,[2] K. Takanashi [2] and A. Hirohata [1]

1 THE UNIVERSITY of York

2 TOHOKU UNIVERSITY

Roadmap on Heusler Alloys

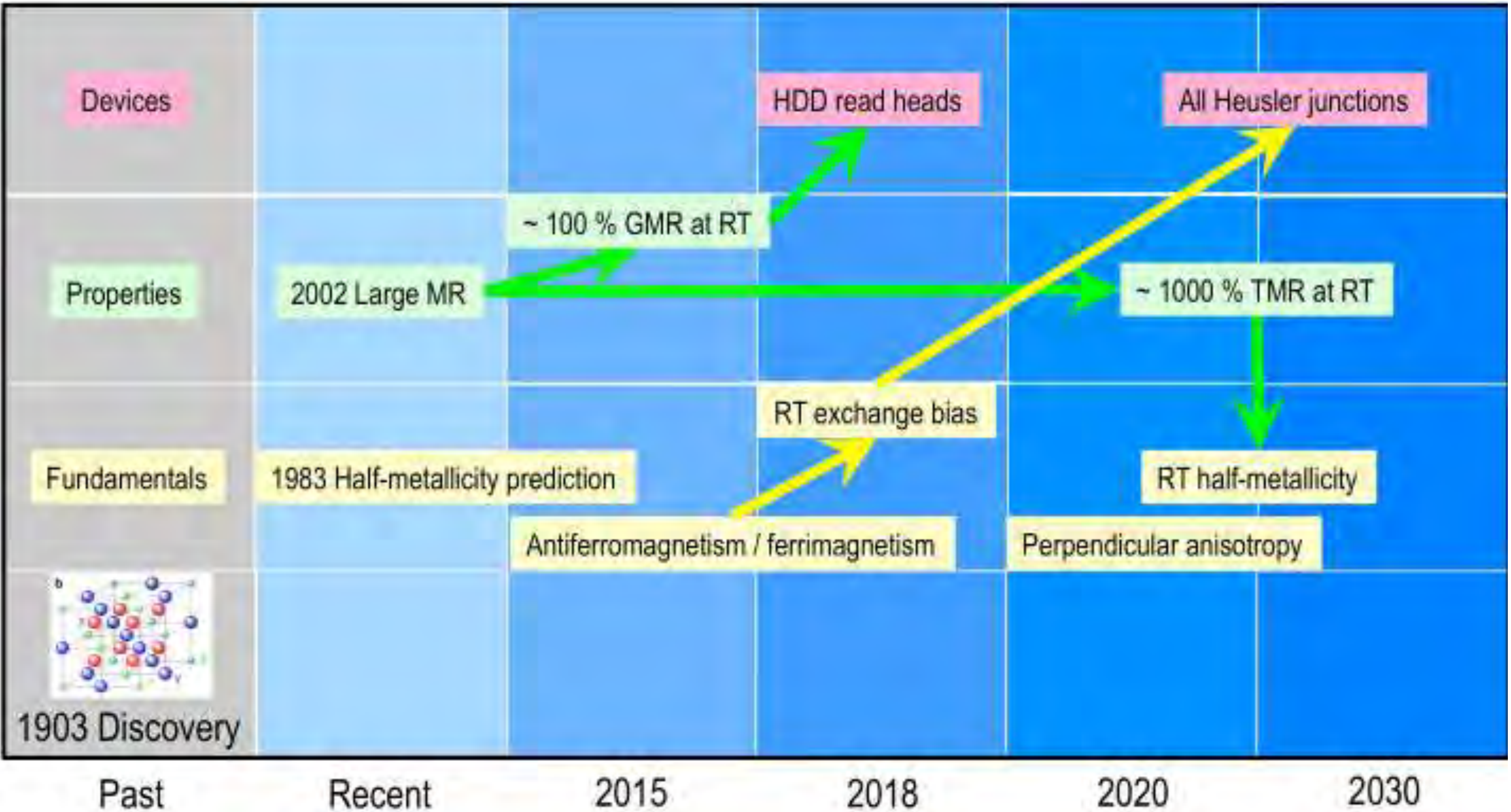

* A. Hirohata *et al.*, *IEEE Trans. Magn.* **51**, 07160747 (2015).

In Situ Crystallisation Process

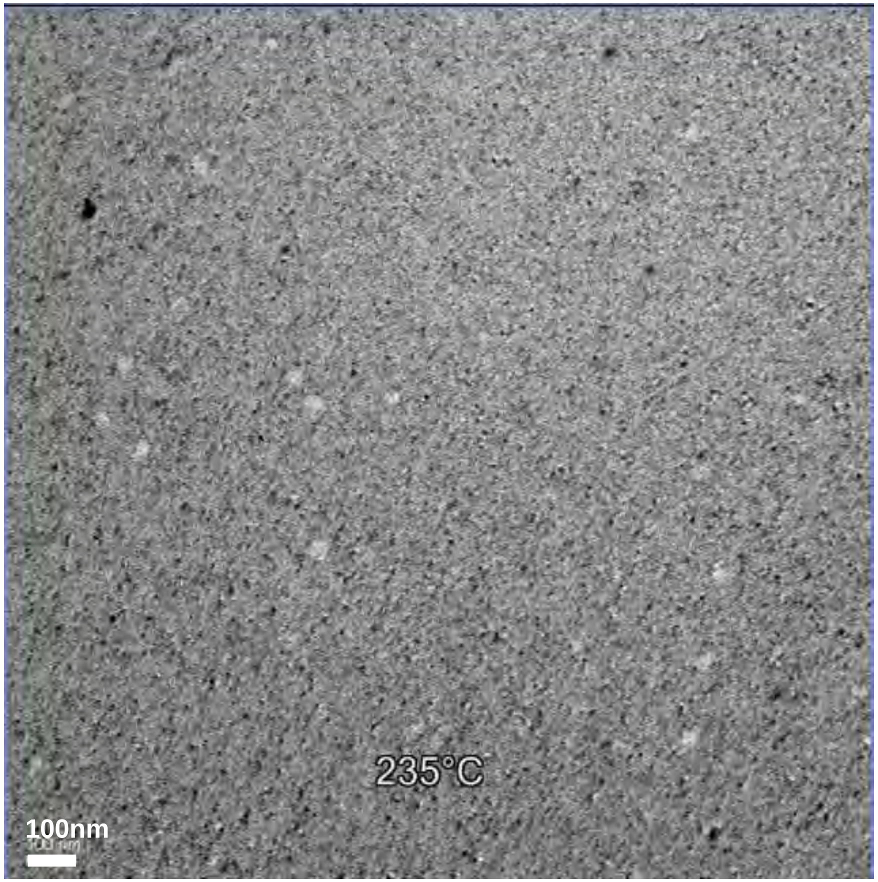

Bright Field TEM
(235°C for 3 hours)

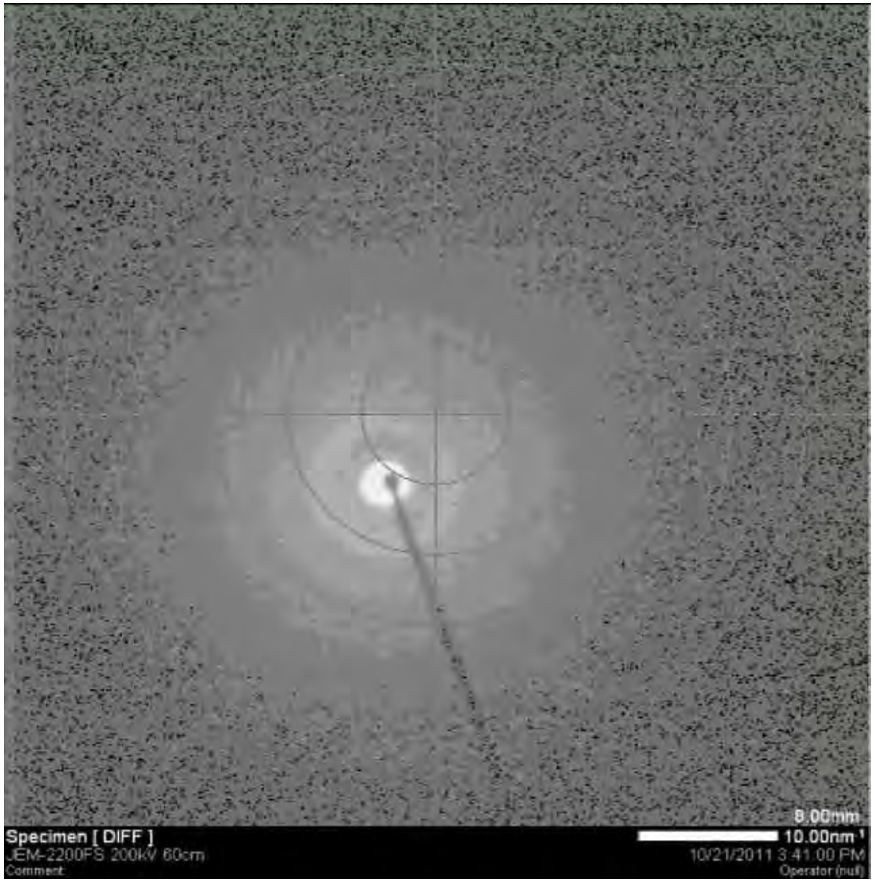

Electron diffraction pattern
(235°C for 3 hours)

* J. Sagar *et al.*, *Appl. Phys. Lett.* **105**, 032401 (2014).

Structural Analysis of Individual Grains

Initial grain nucleation :

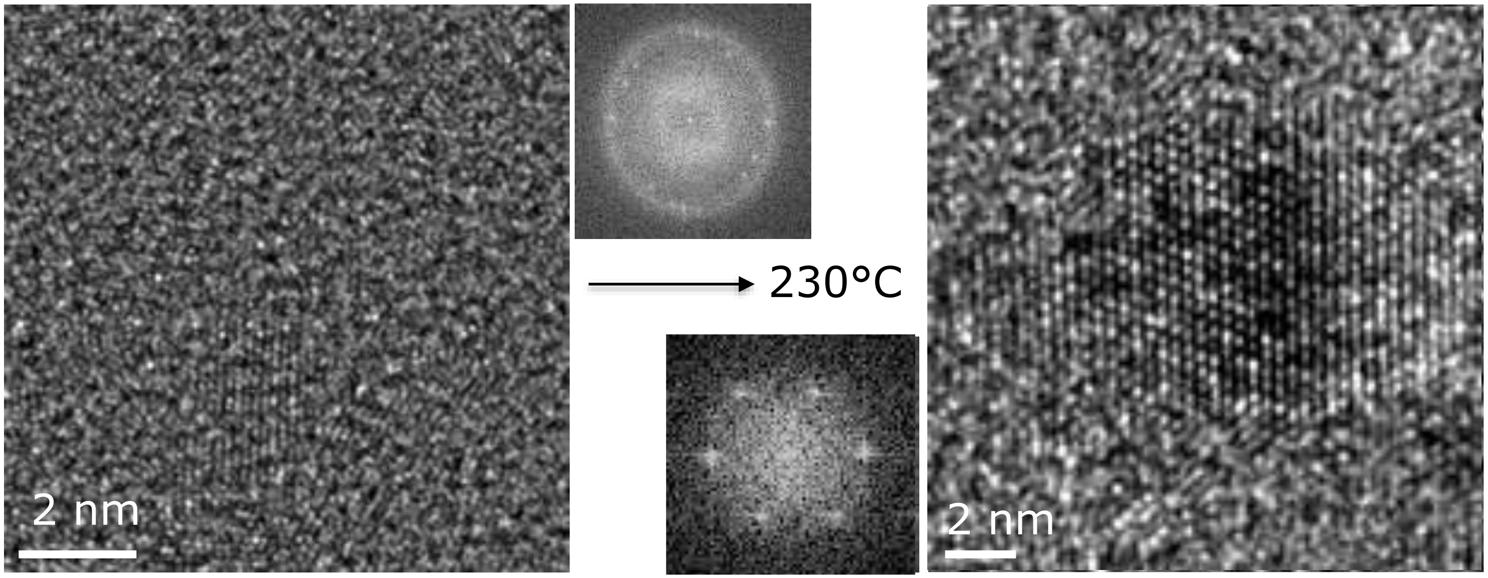

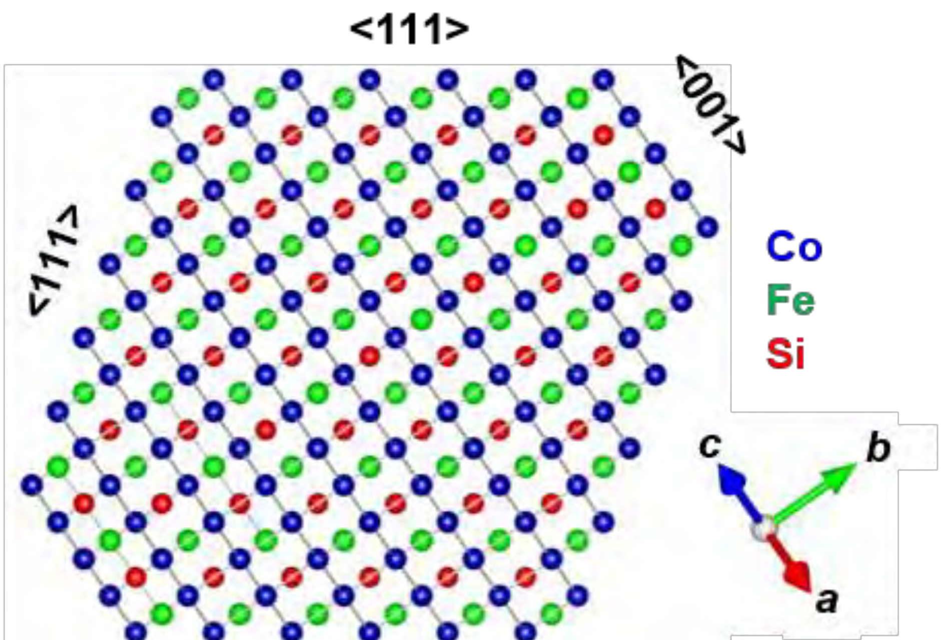

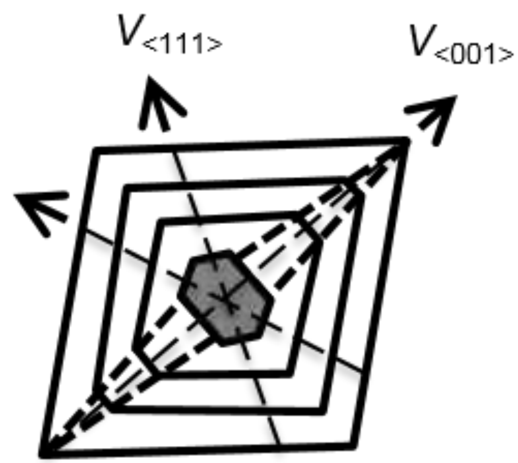

Low Temperature Deposition

$Co_2Fe(Al,Si)$ / W / $Co_2Fe(Al,Si)$ trilayers : *

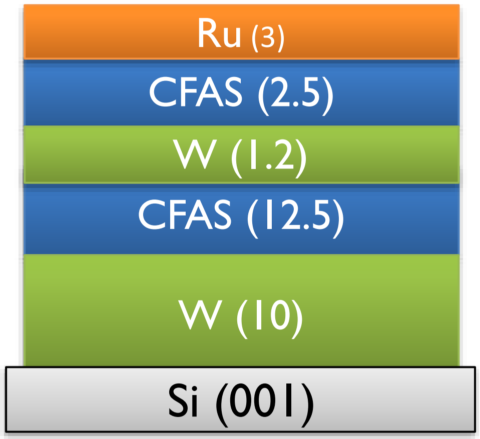

T_S (K)	2θ (°)	D (nm)
292	39.01	8.28
295	39.32	6.60
303	39.72	3.96
315	39.95	3.56
335	40.04	3.32

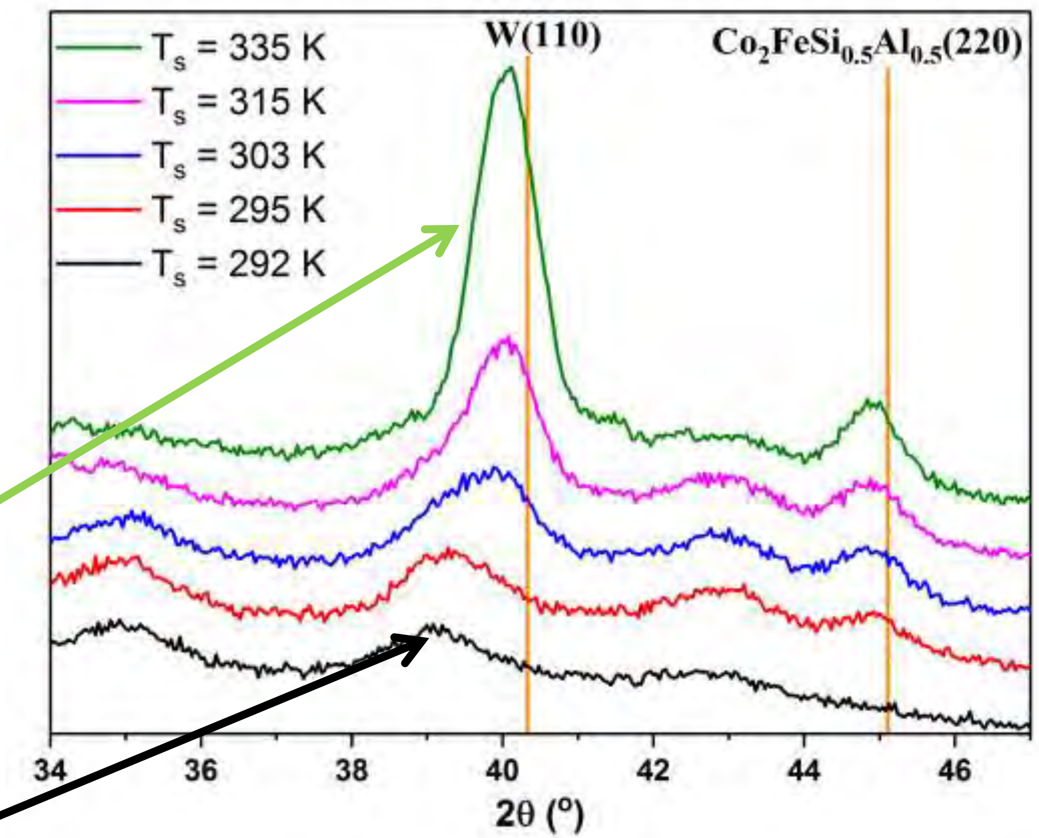

* W. Frost *et al.*, *J. Magn. Magn. Mater.* **484**, 100 (2019).

Current-Induced Crystallisation

$Co_2Fe(Al,Si)$ / Ag / $Co_2Fe(Al,Si)$ trilayers : *

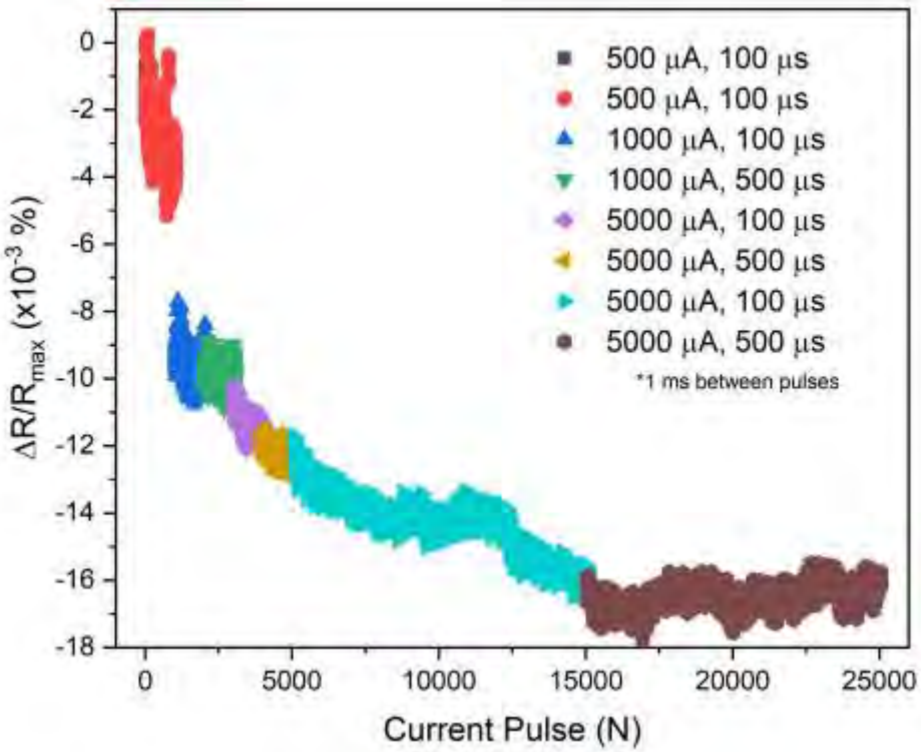

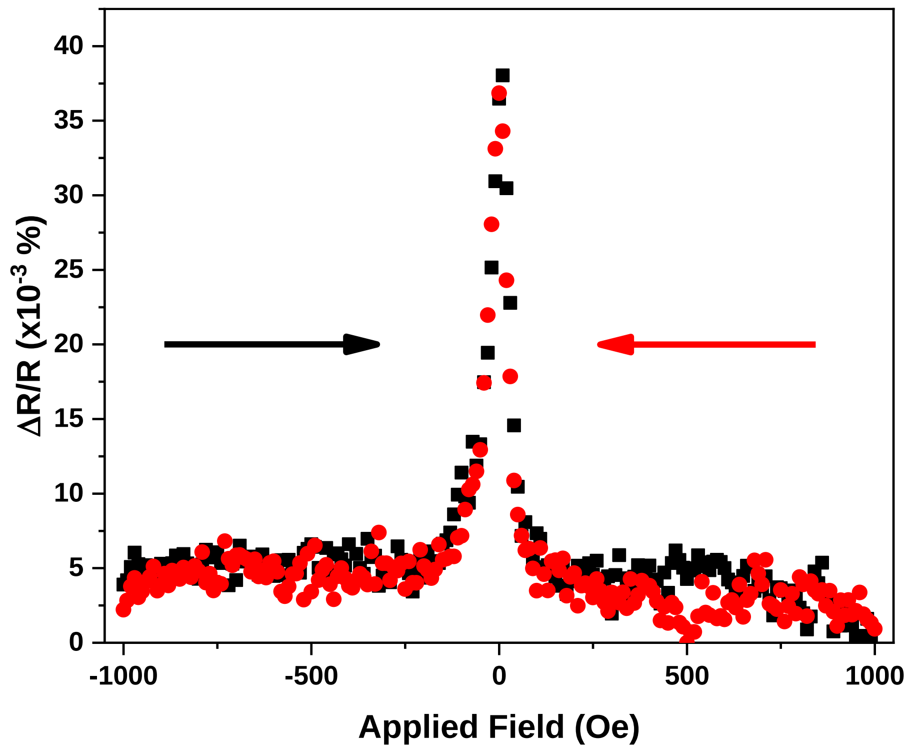

- Resistance change after a series of pulse current applications of 500 μA up to 5 mA for 100 μs up to 500 μs in a GMR device of CFAS/Ag/CFAS.
- Assuming the CFAS disc with the diameter of 100 nm and the thickness of 10 nm,
  - Heating required to increase the temperature by 53 K : ~ 3.31×10^{-11} J.
  - Joule heating by an electrical current of 1 μA at a voltage of 10 μV for 1 s : ~ 1×10^{-11} J.
  - Current-induced crystallised by 10 steps by a pulsed current of 100 ms or less.

* W. Frost *et al.*, *Sci. Rep.* **11**, 18372 (2021).

Crystallinity of $Co_2Fe(Al,Si)$

High-resolution transmission electron micrographs : *

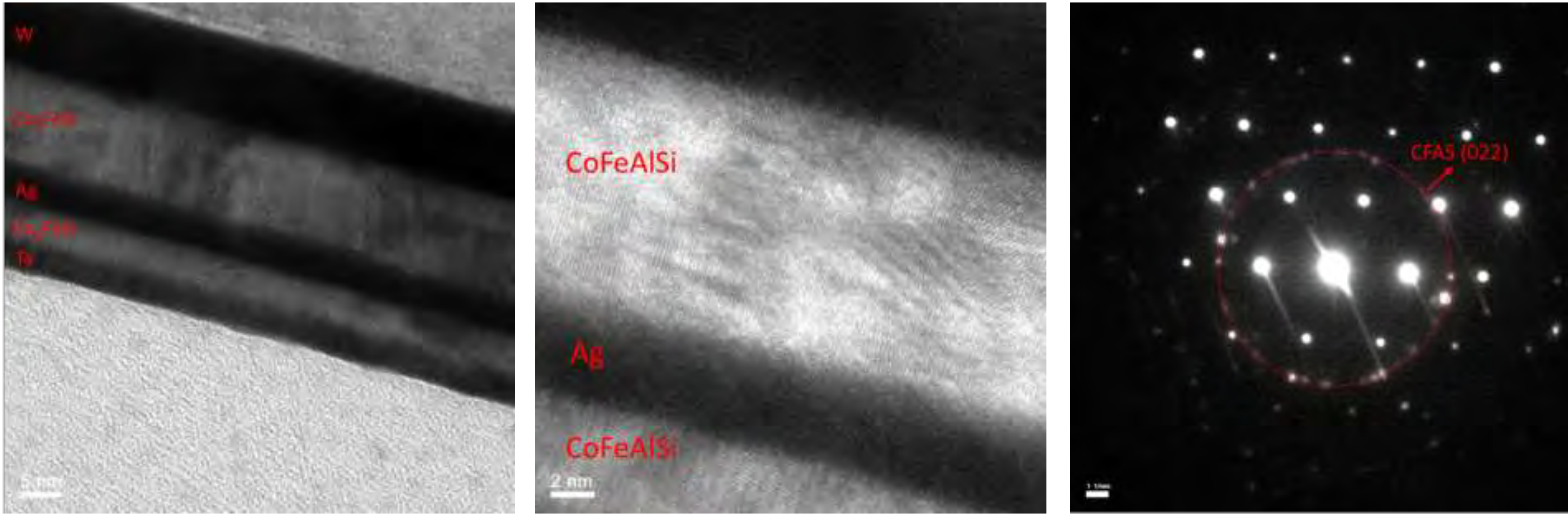

- Cross-sectional TEM images of the GMR device with 300k and 800k magnification.
- Diffraction pattern confirms $Co_2Fe(Al,Si)$ (220) crystallisation.
- Lattice constant is estimated to be 0.57 nm, which is 96.6% of that estimated by the corresponding XRD.

* W. Frost *et al.*, *Sci. Rep.* **11**, 18372 (2021).

Current-Induced Crystallisation for Neuromorphic Computing

$Co_2Fe(Al,Si)$ / Ag / $Co_2Fe(Al,Si)$ trilayers : *

- The current-induced crystallisation leads to the reduction in the corresponding resistivity.
- This acts as memory potentiation for an artificial GMR synapse.
- This offers more realistic neuromorphic computation with higher efficiency.
- Further improvement in GMR ratios is necessary.

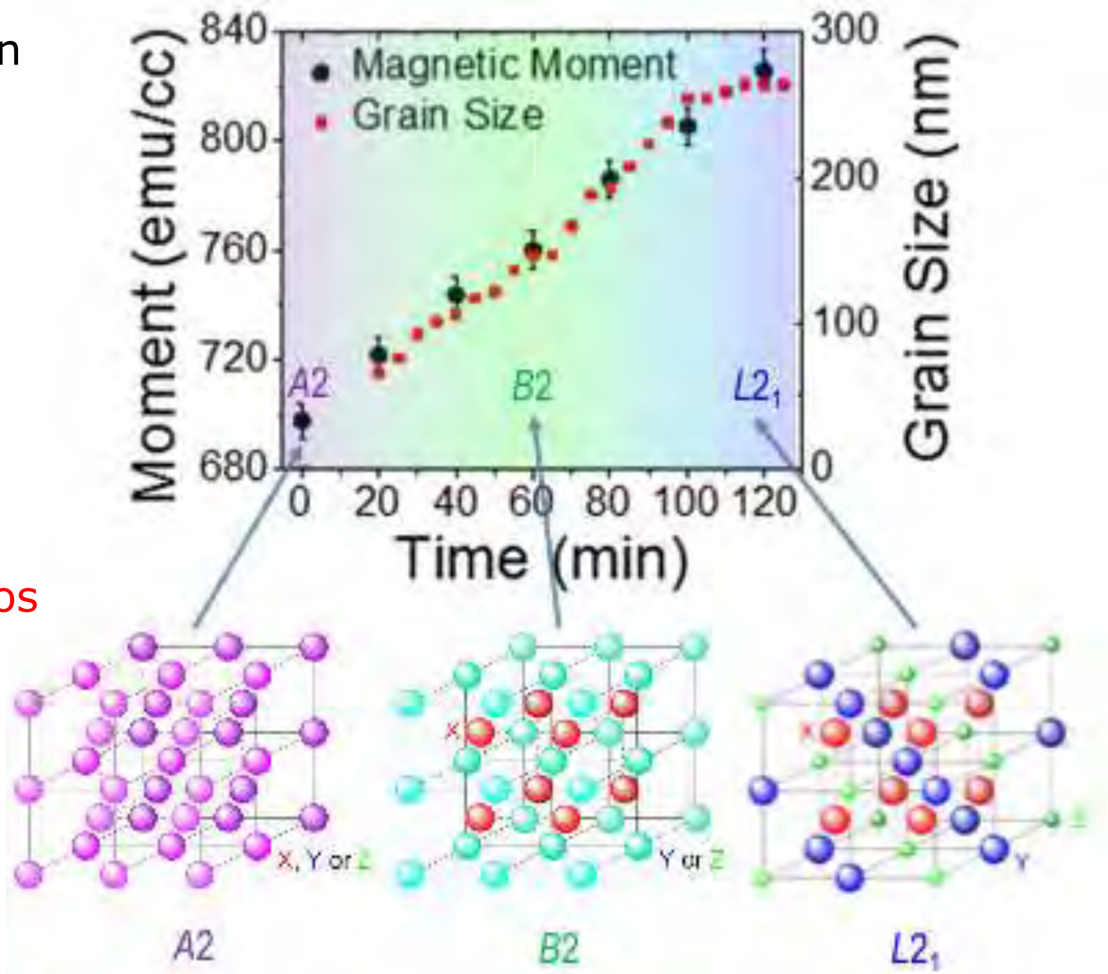

* W. Frost *et al.*, *Sci. Rep.* **11**, 18372 (2021).

Heusler-Based Giant Magnetoresistive Junctions

$Co_2Fe_{0.4}Mn_{0.6}Si$ / $Ag_{0.78}Mg_{0.22}$ / $Co_2Fe_{0.4}Mn_{0.6}Si$ junctions :

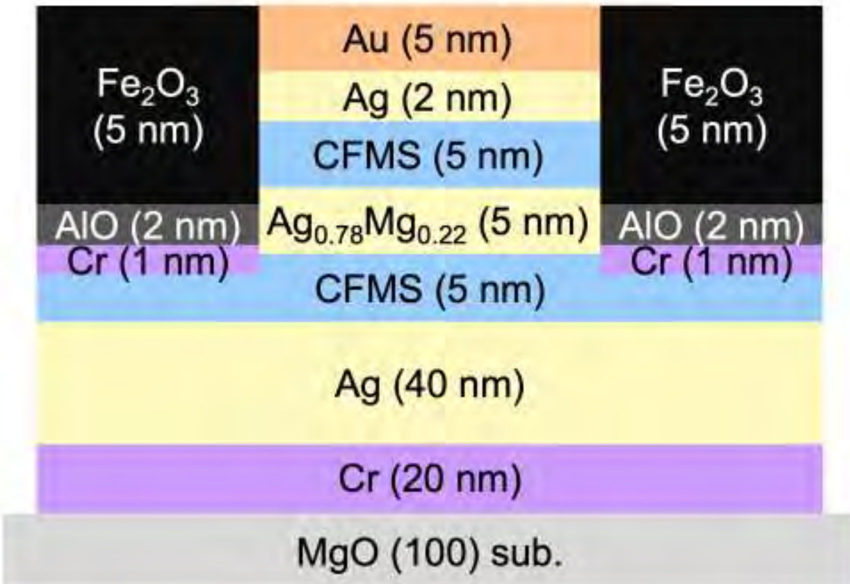

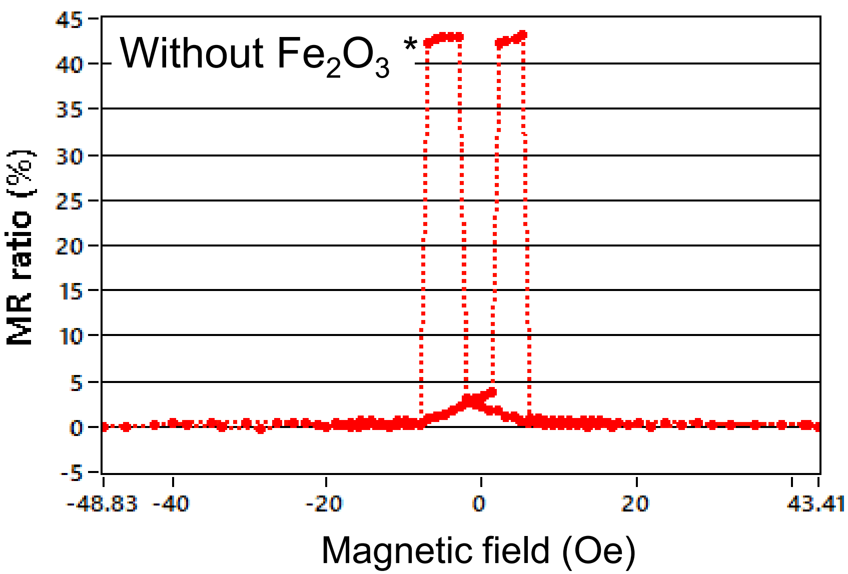

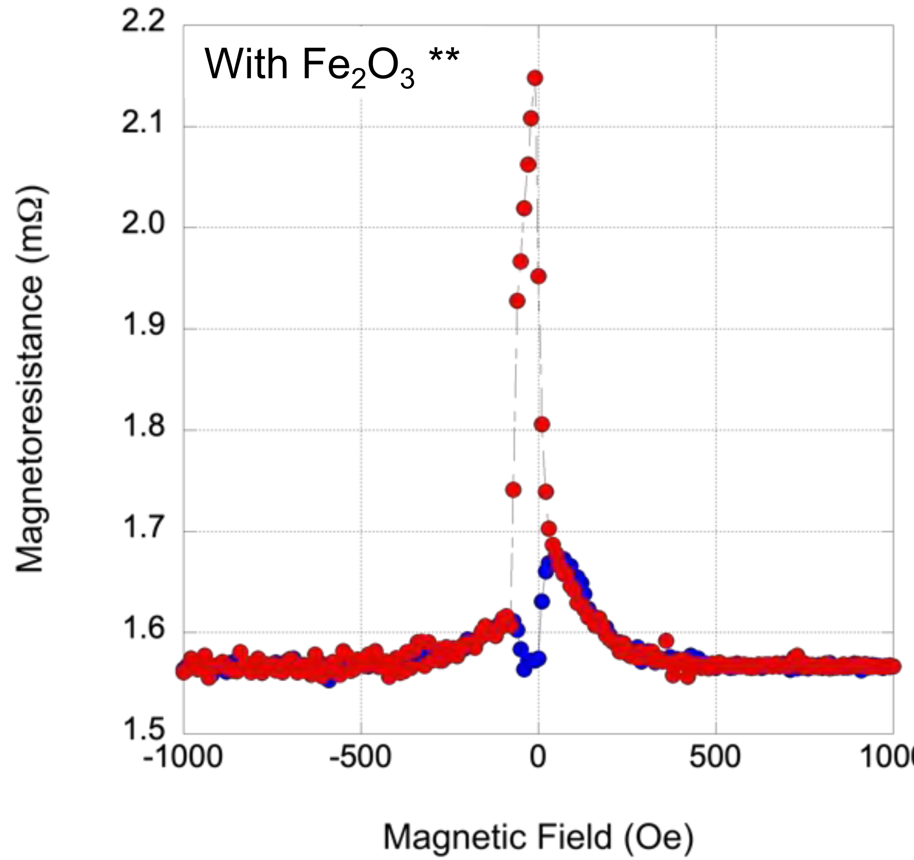

* T. Kubota *et al.*, *Phys. Rev. Mater.* **1**, 044402 (2017);
** W. Frost *et al.*, *Appl. Phys. Lett.* **118**, 172405 (2021).

Current-Induced Crystallisation in Post-Annealed Junction

$Co_2Fe_{0.4}Mn_{0.6}Si$ / $Ag_{0.78}Mg_{0.22}$ / $Co_2Fe_{0.4}Mn_{0.6}Si$ trilayers : *

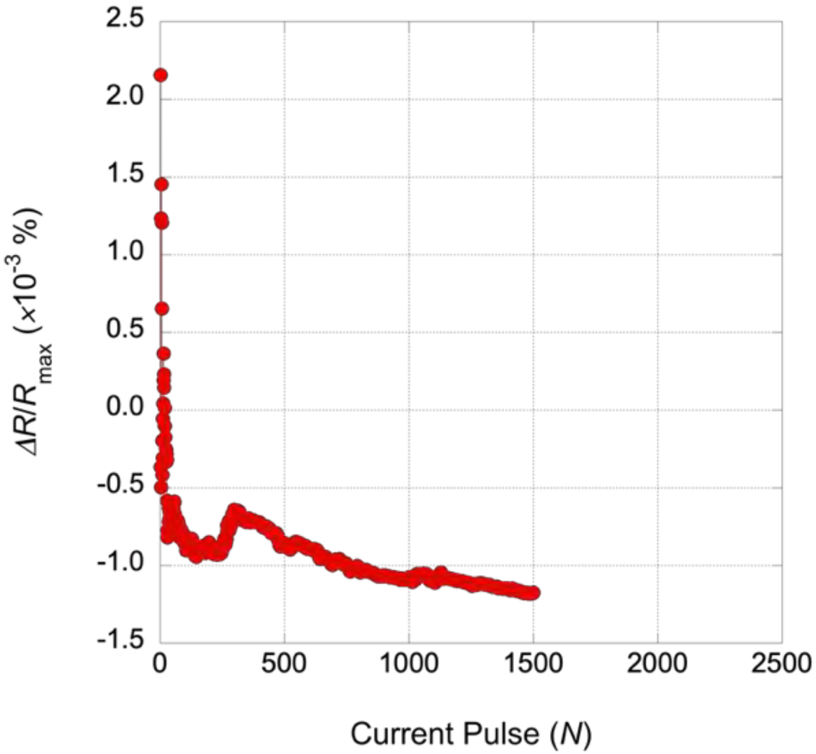

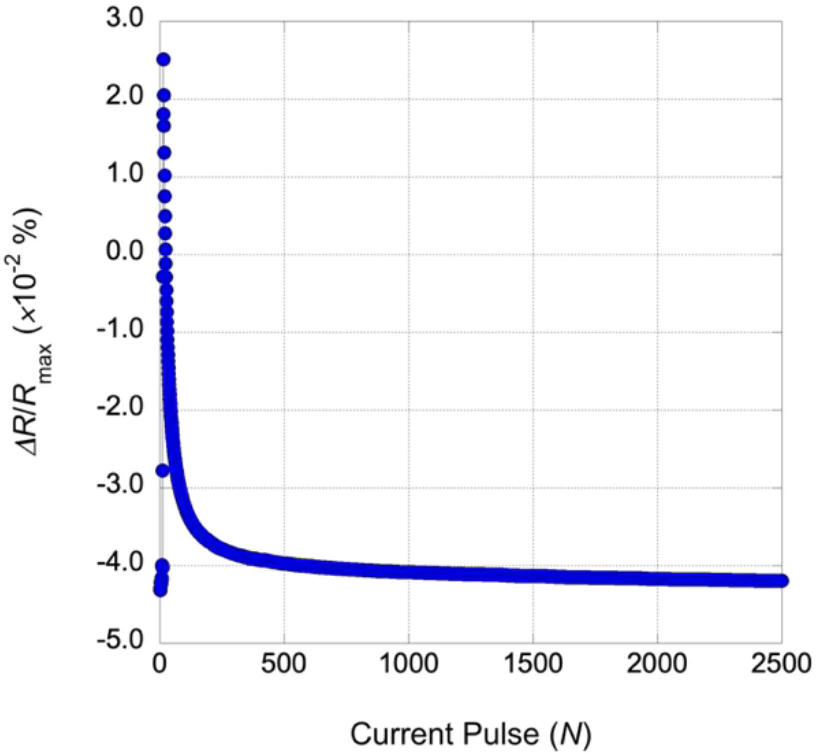

- Resistance change after a series of pulse current applications of 500 μA for 100 μs and 200 μs in a GMR device of $Co_2Fe_{0.4}Mn_{0.6}Si$/Ag-Mg/$Co_2Fe_{0.4}Mn_{0.6}Si$.
- The changes are ~25% as compared with the full current-induced crystallisation for $Co_2FeAl_{0.5}Si_{0.5}$/Ag/$Co_2FeAl_{0.5}Si_{0.5}$.
- Interfaces may be improved by the current applications.

* W. Frost *et al.*, *Sci. Rep.* **11**, 18372 (2021).

Current-Induced Crystallisation in Post-Annealed Junction

$Co_2Fe_{0.4}Mn_{0.6}Si$ / $Ag_{0.78}Mg_{0.22}$ / $Co_2Fe_{0.4}Mn_{0.6}Si$ trilayers : *

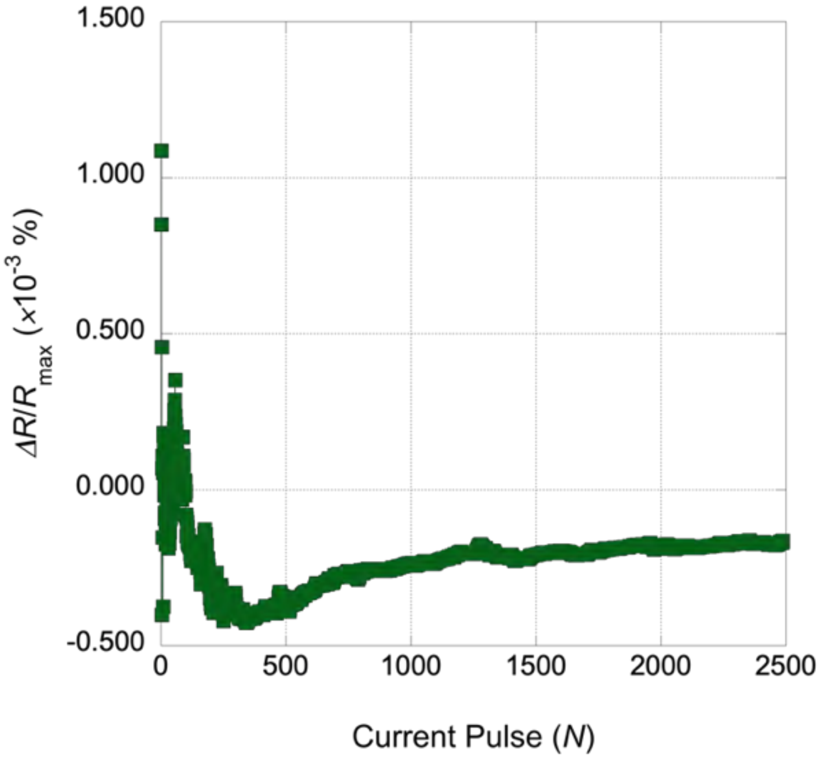

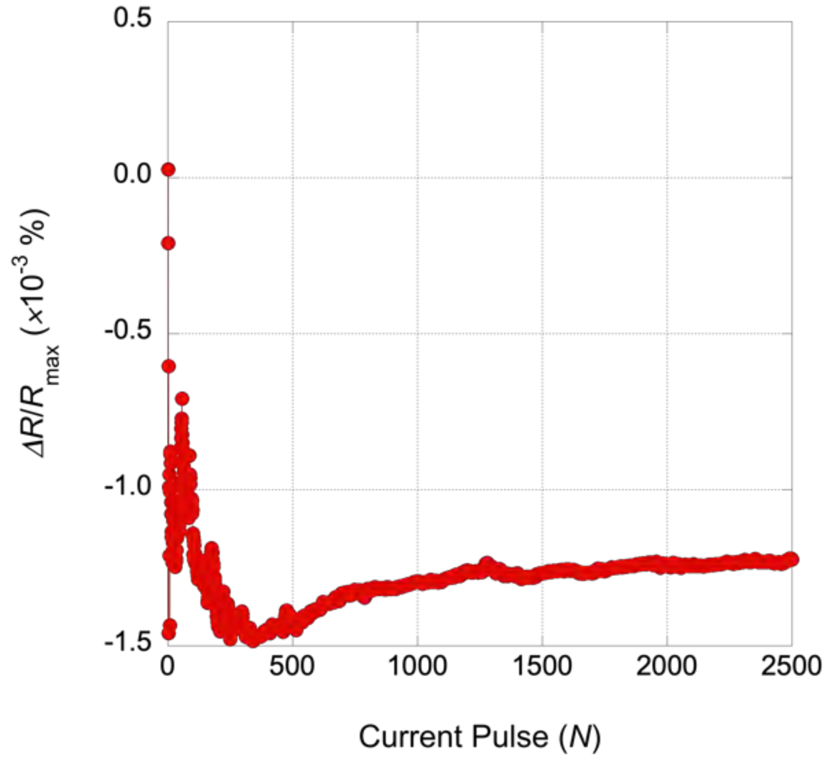

- Resistance change after a series of pulse current applications of 600 μA for 100 μs and 250 μs in a GMR device of $Co_2Fe_{0.4}Mn_{0.6}Si/Ag\text{-}Mg/Co_2Fe_{0.4}Mn_{0.6}Si$.
- The changes are ~25% as compared with the full current-induced crystallisation for $Co_2FeAl_{0.5}Si_{0.5}/Ag/Co_2FeAl_{0.5}Si_{0.5}$.
- Interfaces may be improved by the current applications.

* W. Frost *et al.*, *Sci. Rep.* **11**, 18372 (2021).

Current-Induced Crystallisation

Potentiation for neuromorphic computation :

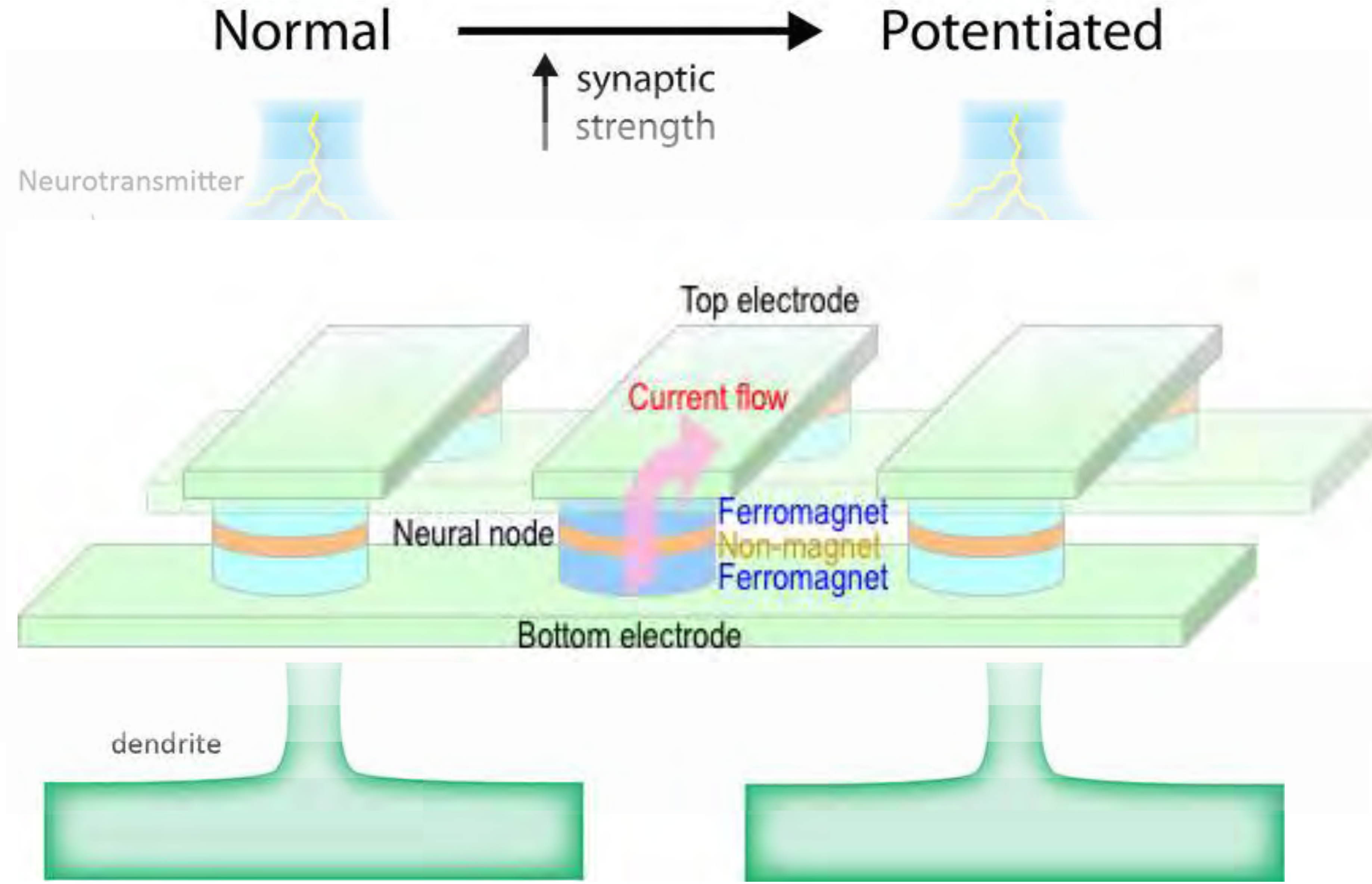

* https://qbi.uq.edu.au/brain-basics/brain/brain-physiology/long-term-synaptic-plasticity

Summary

- Machine learning was used to predict new half-metallic Heusler alloys.
- First-principles calculations were performed on selected Heusler alloys, NiCrMnSi and CoIrMn*Z* (*Z* = Al, Si, Ga and Ge).
- CoIrMnAl films were successfully crystallised into the *Y* phase.
- The lattice constants of the films post-annealed at 500~600ºC were almost the same with the predicted values.
- The corresponding saturation magnetisation and Curie temperature were ~70% of the predicted values.
- Further materials development using machine learning can demonstrate better properties for greater integration and capacity of storages and memories.

Group Members

Thank you very much for your attention.

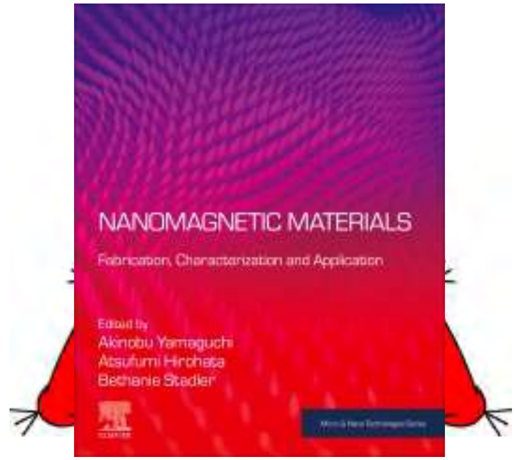

Atsufumi Hirohata

Department of Electronic Engineering
University of York
+44 (0)1904 32 3245
atsufumi.hirohata@york.ac.uk

york spintronics

extreme CRM cost

itc

eit European Institute of Innovation & Technology

The EIT is a body of the European Union

EPSRC Engineering and Physical Sciences Research Council

THE ROYAL SOCIETY

JST

SEVENTH FRAMEWORK PROGRAMME

SEAGATE

JEOL Solutions for Innovation

Development in Spintronics

Electrical spin generation	1957 RKKY	1975 Jullière	1988 GMR	1995 RT-TMR Spin-valve 1996 STT theory 1999 STT experiment 1999 Spin injection	2001 Giant TMR theory 2004 Giant TMR 2003 Spin oscillator 2000 Conductance mismatch 2004 LLG equation	2016 Neuromorphic operation	
Spin-orbit effects	1960 DMI theory 1958 SOT theory 1958 Skyrmionl theory	1971 Spin Hall theory			2004 Domain motion by a current 2004 Spin Hall experiment 2006 Inverse spin Hall 2009 Skyrmions		
Electric field application			1989 FM DMS	1990 Spin FET concept	2000 Voltage-control FM		
Electromagnetic wave application				1995 Photoexcitation 1998 Spin STM	2002 Spin pumping 2002 FMR	2010 Magnonics	
Spin-band splitting				1993 Spin injection 1999 Spin LED			
Influence of thermal gradient					2008 Spin Seebeck	2017 Spin Nernst	
Geometrical phase	1959 AB effect		1981 AAS effect 1984 Berry phase	1992 Persistent current theory 1999 Ballistic MR			
Mechanical rotation	1015 Barnett effect					2011 Spin mechatronics theory 2016 Hydrodynamic spin current 2018 MOKE detection	
Materials	1903 Heusler alloy discovery		1983 Half-metallic Heusler alloy 1988 DMS		2005 Topological insulator		
Products	1956 HDD	1972 MRAM concept		1997 GMR-HDD 1995 GMR sensors	2002 MRAM 2008 TMR-HDD	2016 TMR sensors 2011 Racetrack memory prototype 2019 STT-MRAM	

1970 1980 1990 1G 2000 2G 2010 3G 2020

* A. Hirohata *et al.*, *J. Magn. Magn. Mater.* **509**, 166711 (2020).

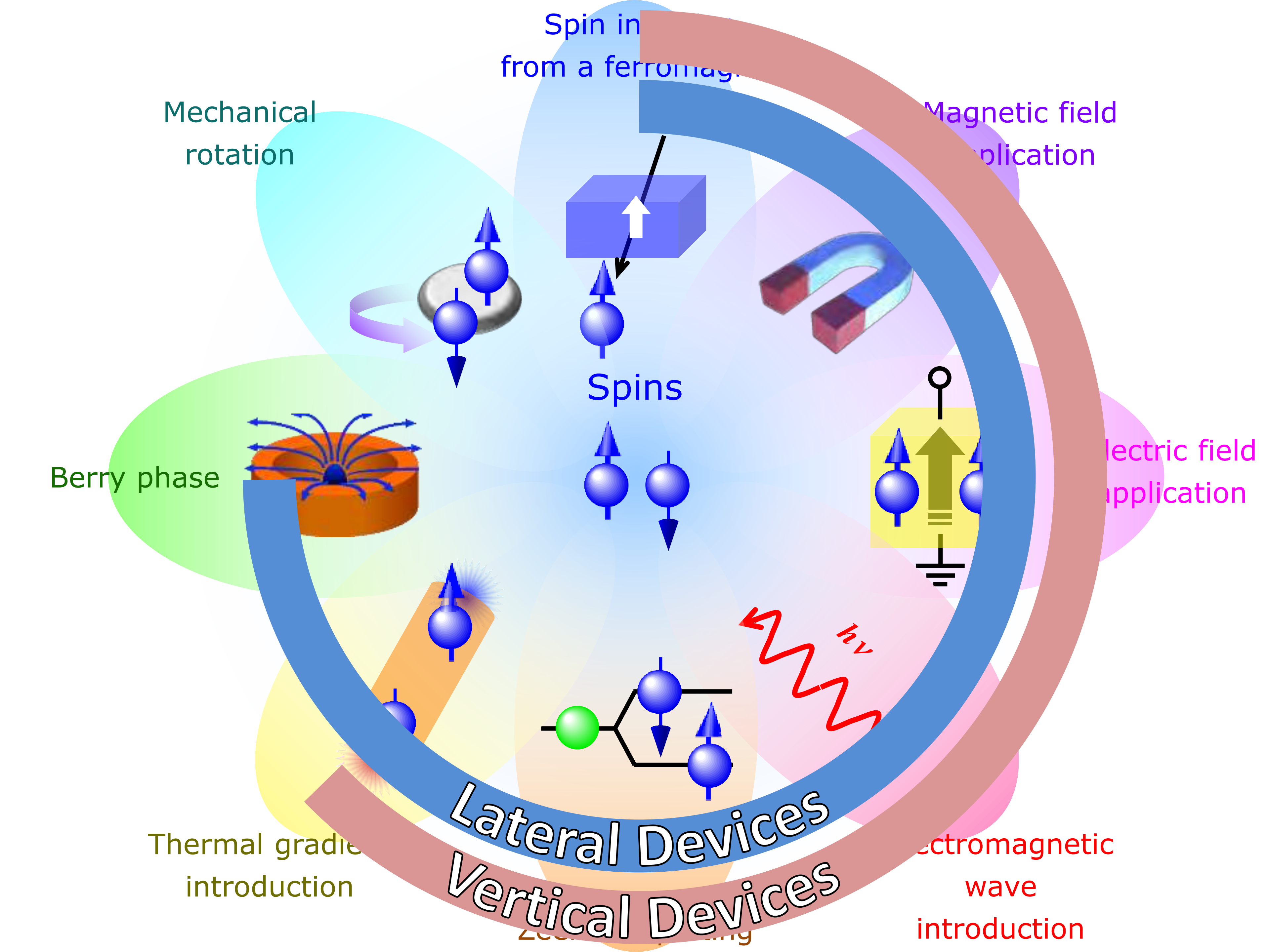
Mechanical rotation
Magnetic field
Spins
Berry phase
hν
Lateral Devices
Vertical Devices
wave
introduction

Possible Heusler Alloys

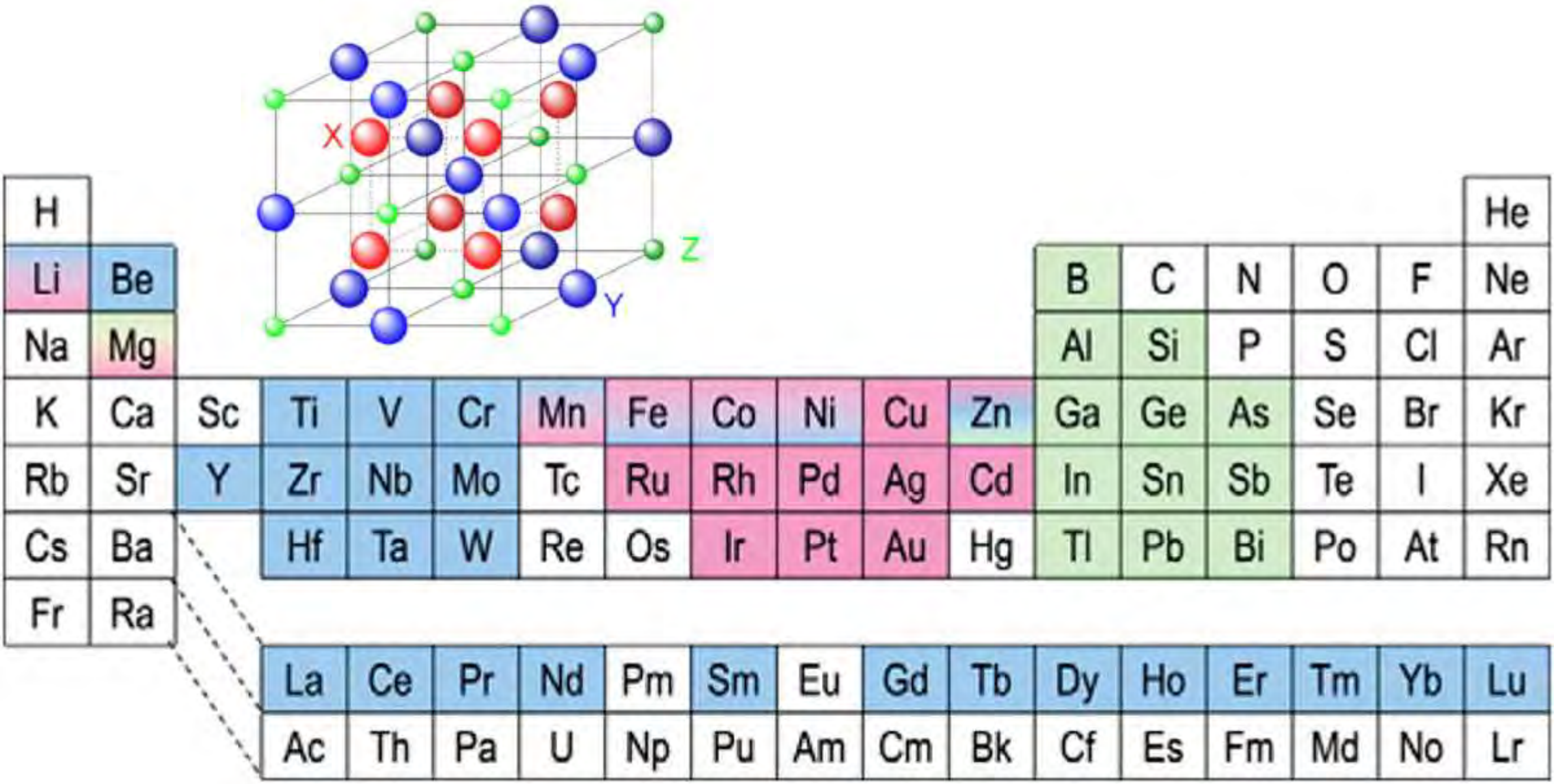

15 × 30 × 14 = 6,300 combinations !

* K. Elphick *et al.*, *Sci. Technol. Adv. Mater.* **22**, 235 (2020).

Machine Learning for Materials Science

Machine learning explosion in materials science : *

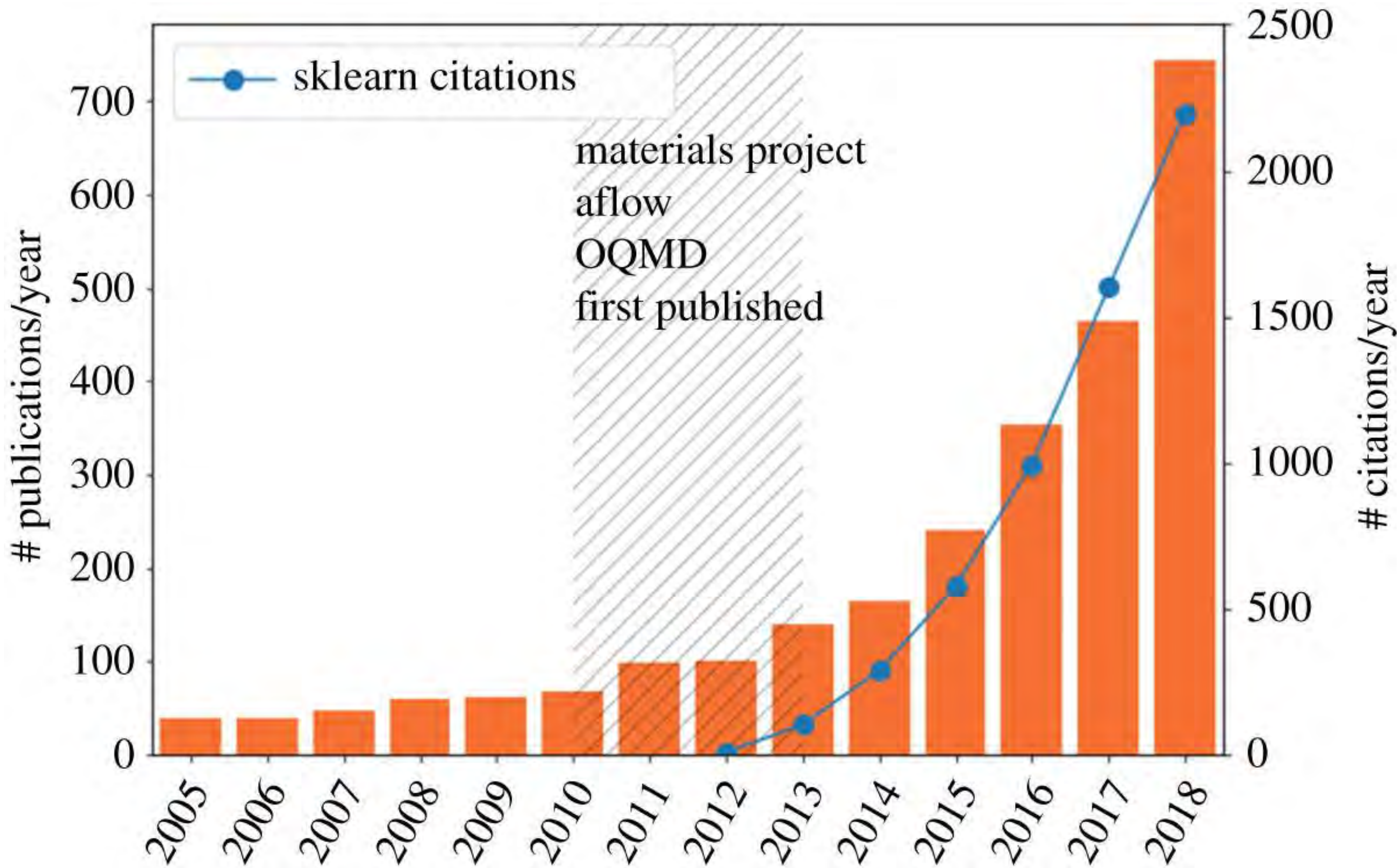

* T. Hey *et al.*, *Phil. Trans. R. Soc. A* **378**: 20190054 (2020).

npj Computational Materials www.nature.com/npjcompumats

REVIEW ARTICLE OPEN

Recent advances and applications of machine learning in solid-state materials science

Jonathan Schmidt[1], Mário R. G. Marques[1],

CHEMISTRY OF MATERIALS

Editorial

Cite This: Chem. Mater. 2019, 31, 9579–9581 pubs.acs.org/cm

Five High-Impact Research Areas in Machine Learning for Materials Science

Discover Materials

Discover

Review

Big data and machine learning for materials science

Jose F. Rodrigues Jr[1] · Larisa Florea[2] · Maria C. F. de Oliveira[1] · Dermot Diamond[3] · Osvaldo N. Oliveira Jr[4]

Received: 9 February 2021 / Accepted: 1 April 2021

Computational Materials Science 193 (2021) 110360

Contents lists available at ScienceDirect

Computational Materials Science

journal homepage: www.elsevier.com/locate/commatsci

Check for updates

Machine learning in materials science: From explainable predictions to autonomous design

Ghanshyam Pilania

Materials Science and Technology Division, Los Alamos National Laboratory, Los Alamos, NM 87544, USA

Flow of Machine Learning

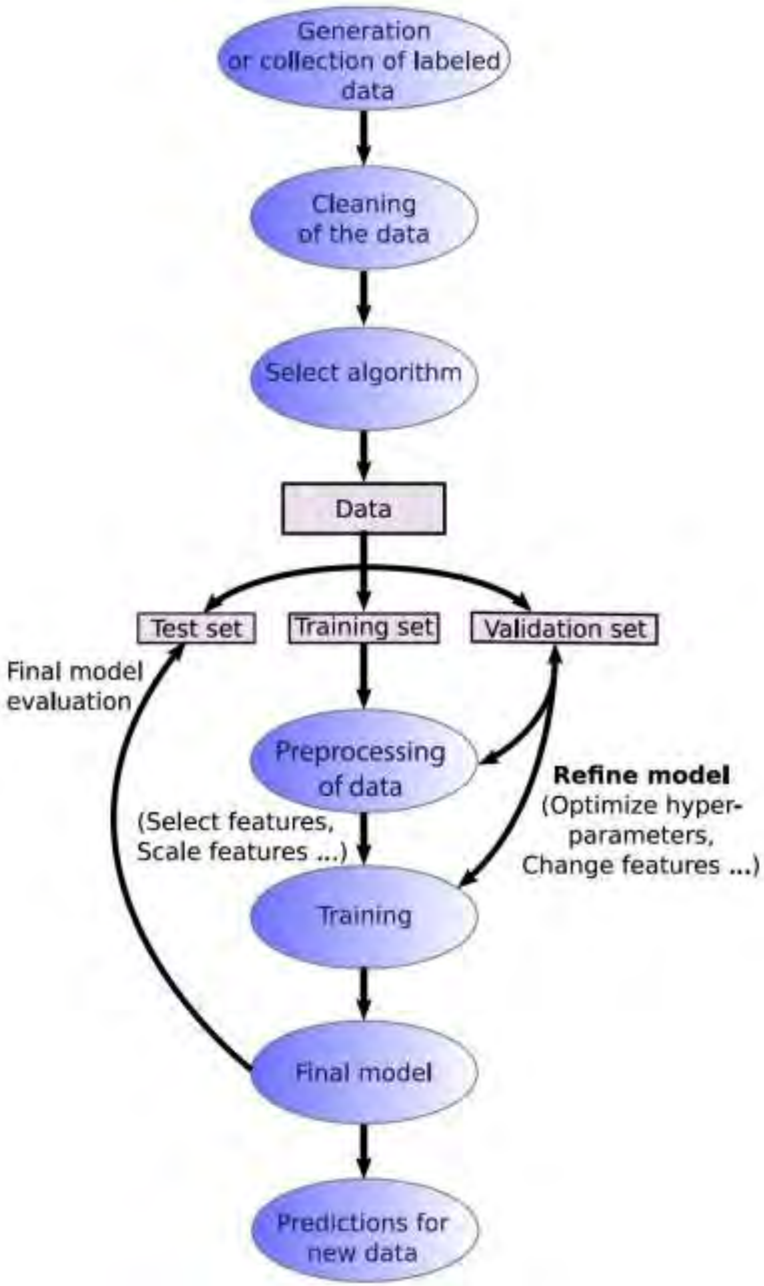

* J. Schmidt *et al.*, *npj Computational Materials* **5**, 83 (2019).

Search for New Materials

Using machine learning, we investigate new ferromagnets :

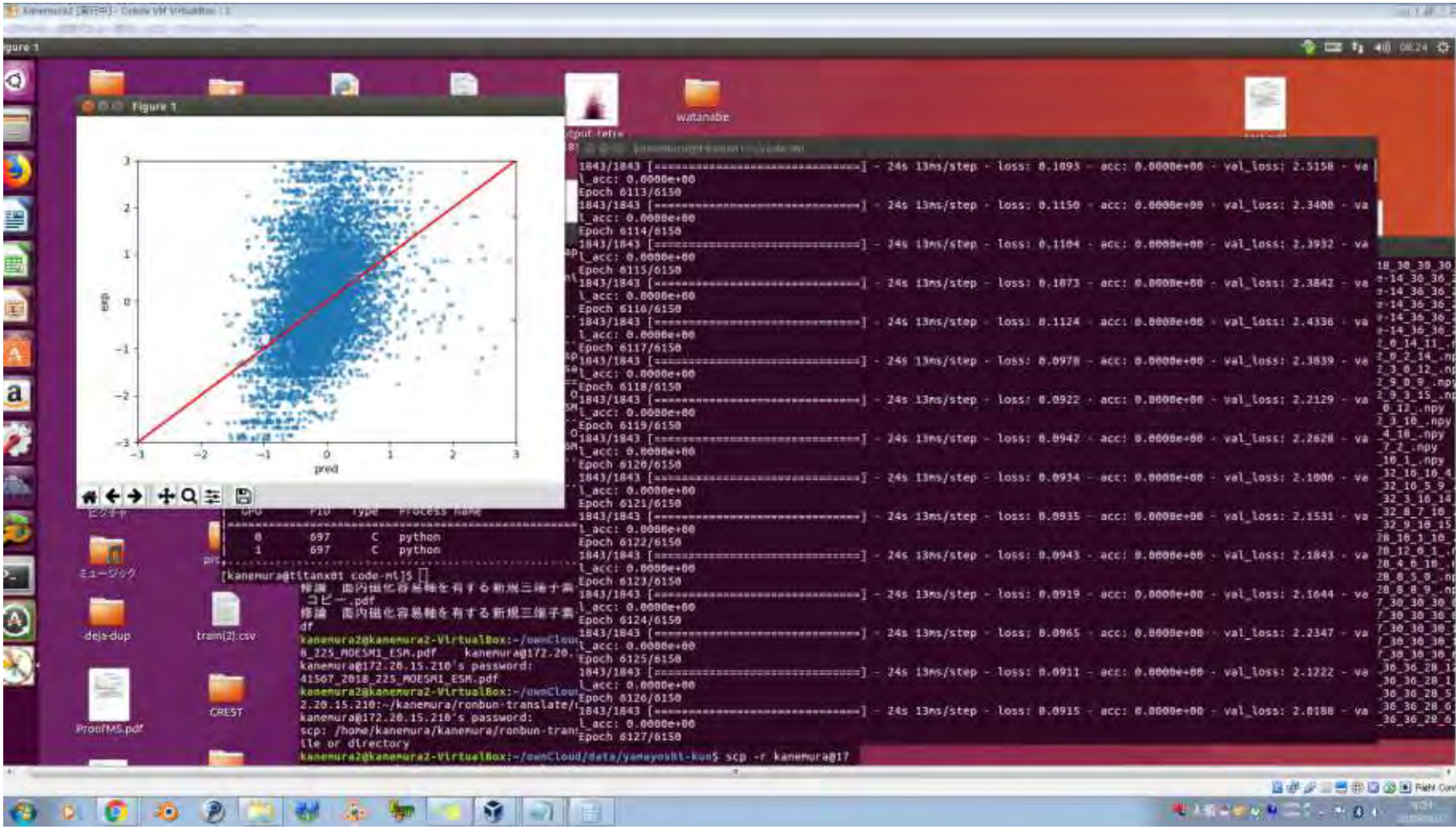

Data Set Convergence

Data set improvement for cubic and tetragonal crystals :

- Data converges when the final total energy and one before is $< 10^{-4}$ eV.

  $\rightarrow$ Data convergence / divergence.

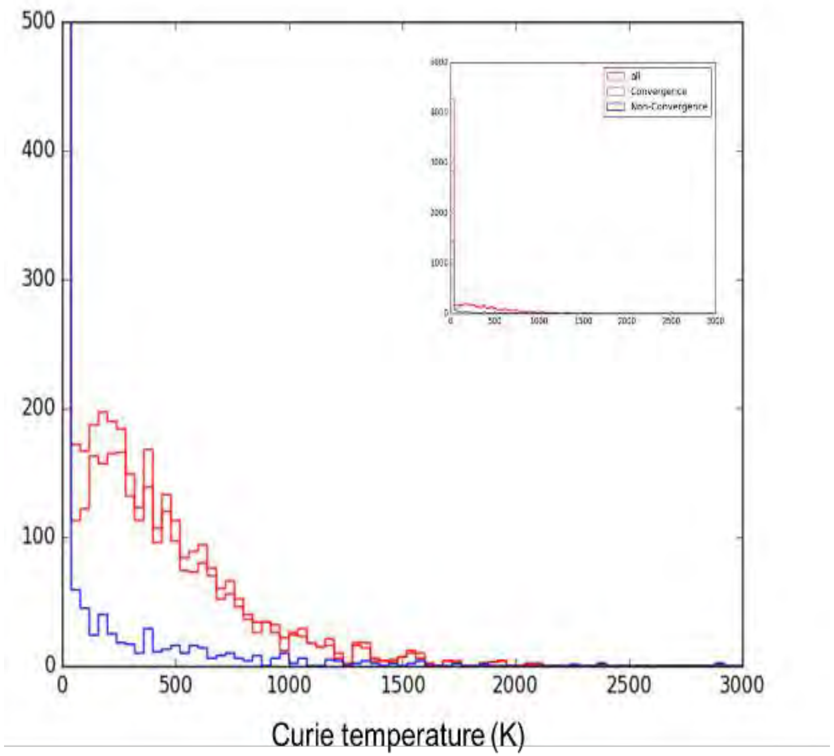

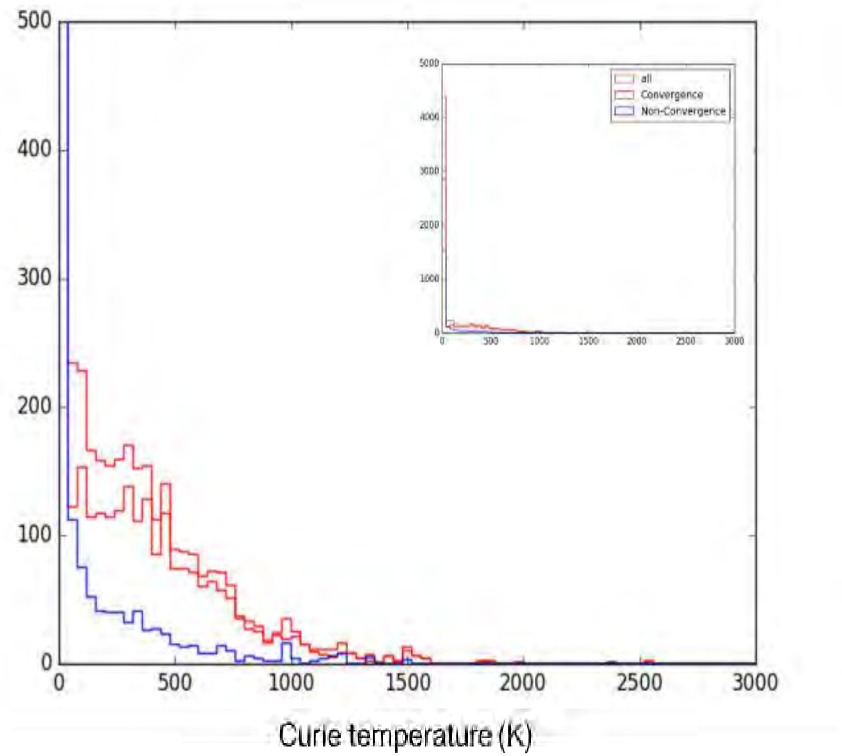

Data Set Improvement

Data set improvement for cubic crystals :

- Select converged data only

  → Correlation coefficient improves by 5~10 %.

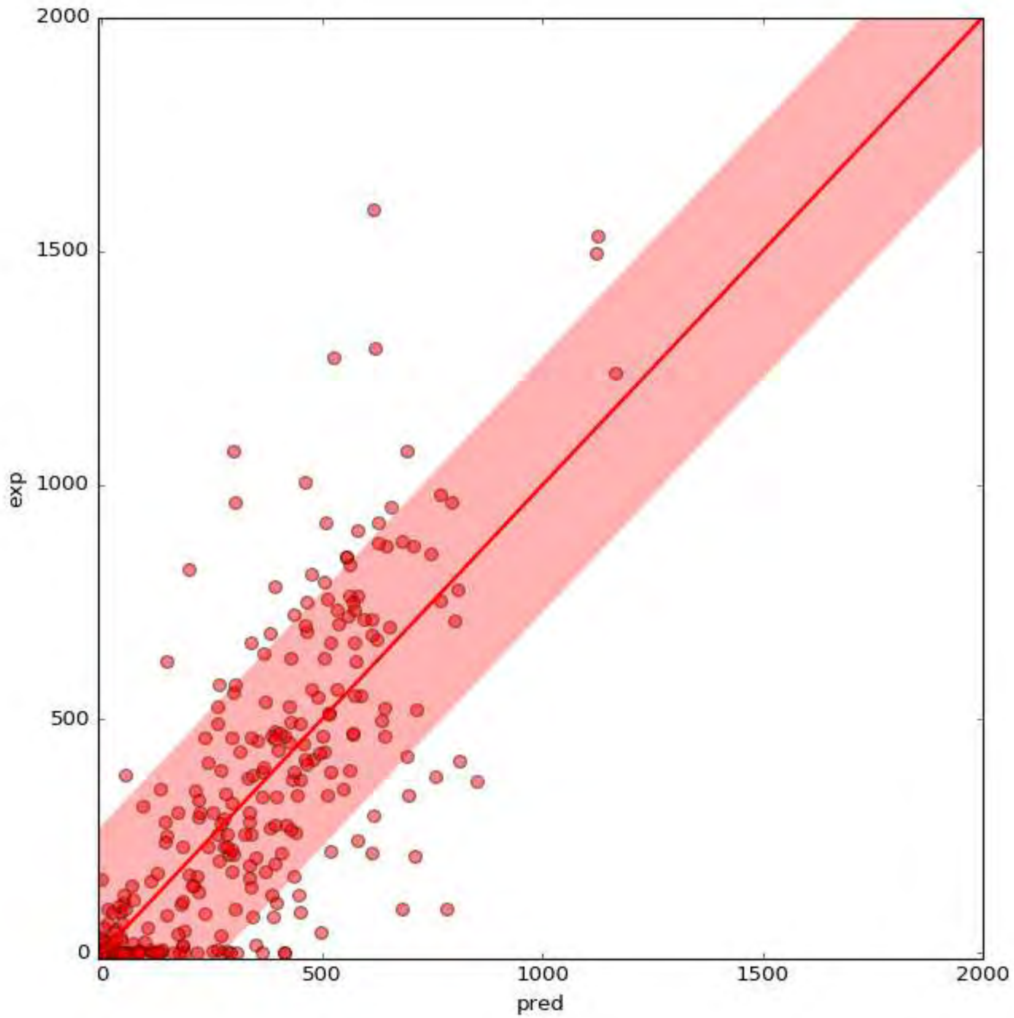

	Cubic	Tetragonal
Converged data only	0.79	0.82
Both converged and diverged data	0.69	0.77

Random Forest

Descriptors for random forest :

- Predicted magnetic property
  - → Default data set.
  - → Use a magnetic moment as a descriptor.
  - → Use density of states (DOS).
  - → Use both DOS and moment.

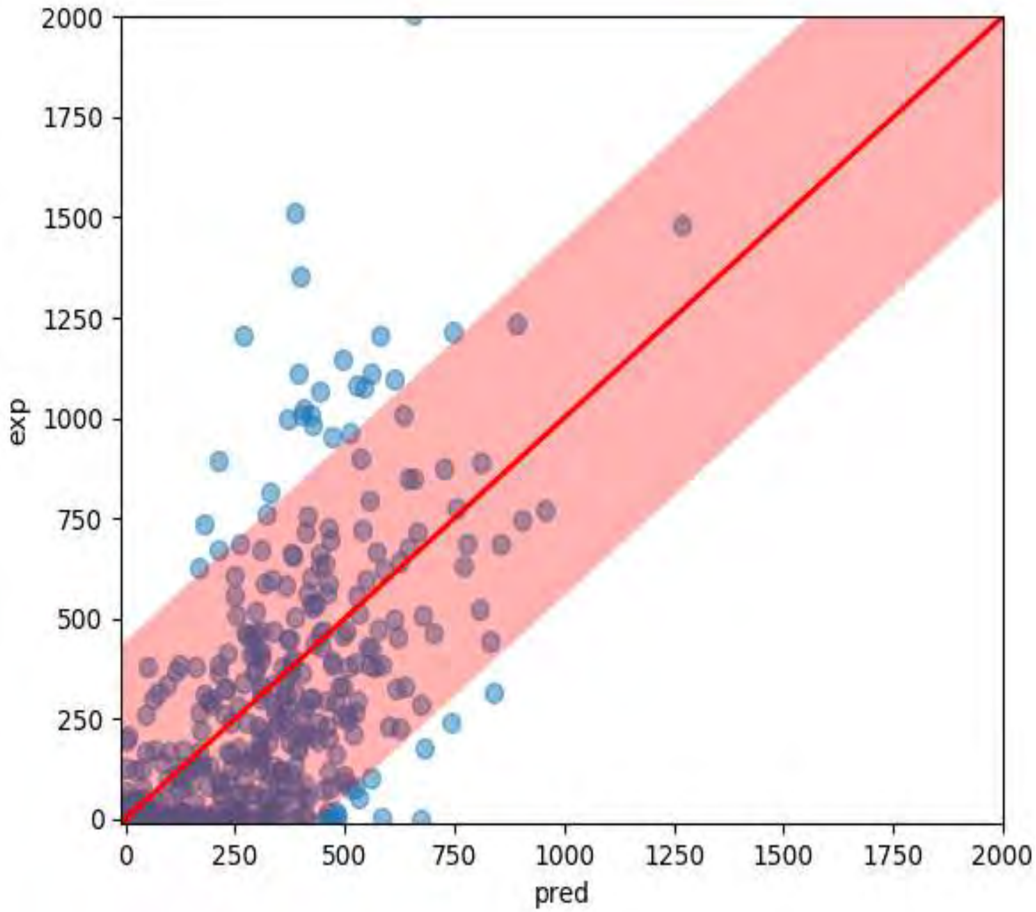

Deep Learning

Convolutional neural network (CNN) :

- Predicted total energy

  → CNN advantageous over random forest.

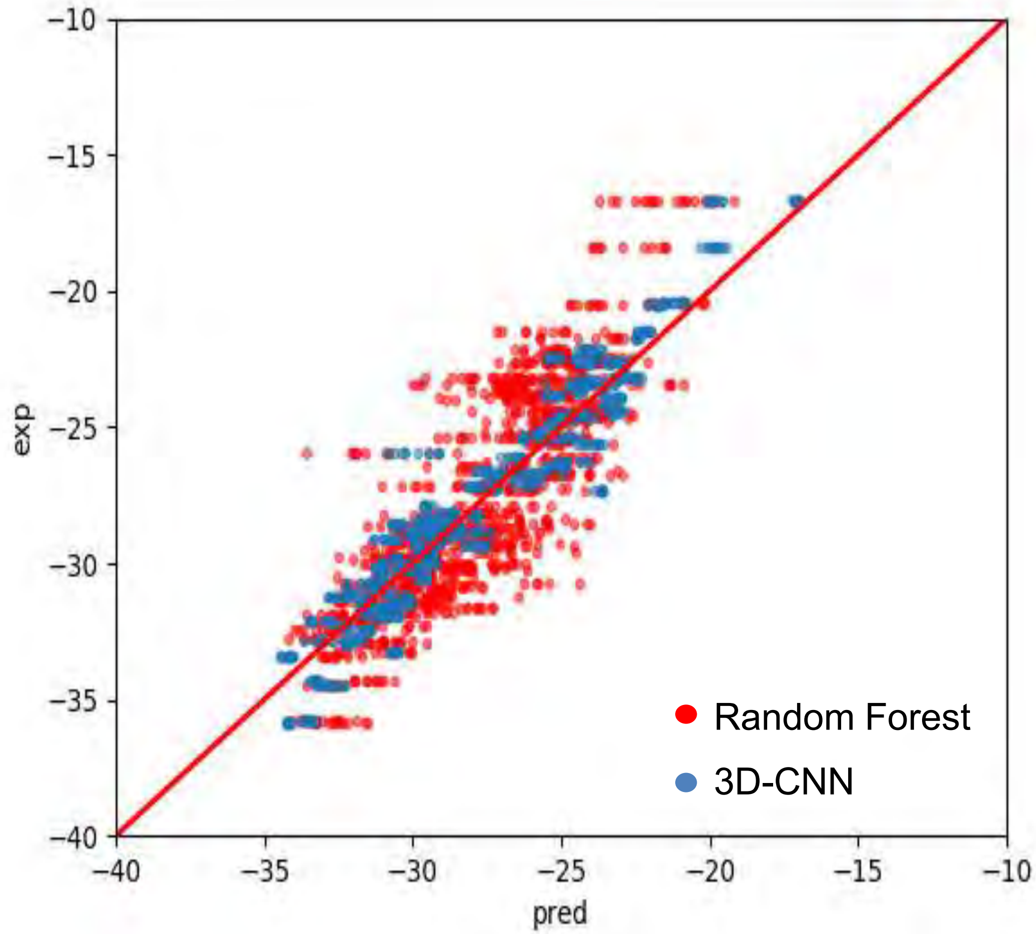

First Principles Calculations on CoIrMnAl

Similar calculations were performed on CoIrMn*Z* (*Z* = Al, Si, Ga and Ge) : *

- VASP used in combination with the projector augmented wave method.
- GGA used as an exchange correlation potential.
  - Energy cutoff : 500 eV for the plane waves.
  - *k*-mesh of 16 × 16 × 16.
  - Energy and the force tolerance : 10 μeV and 10 meV Å^{-1}, respectively.

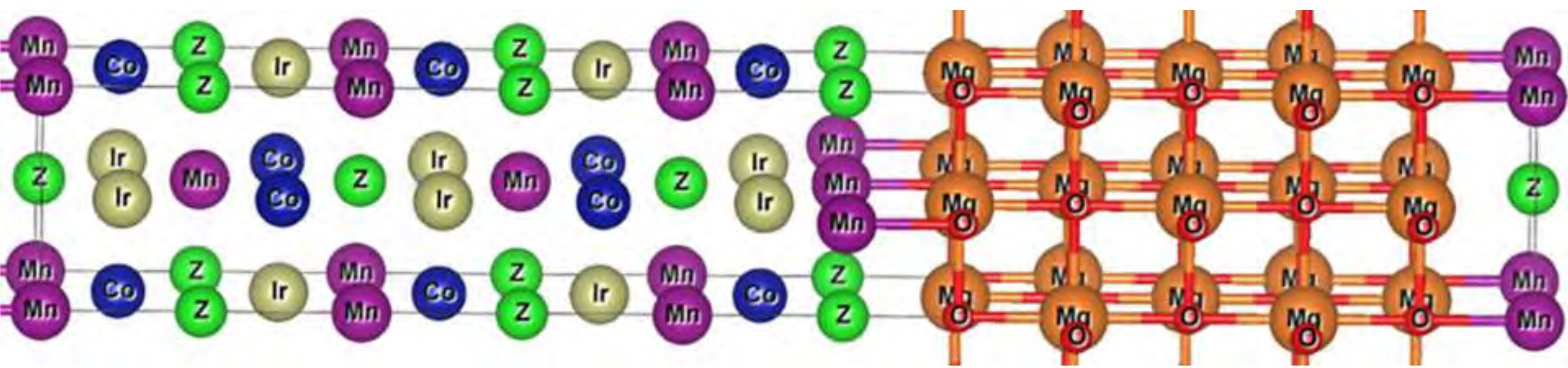

* T. Roy *et al.*, *J. Magn. Magn. Mater.* **498**, 166092 (2020).

First Principles Calculations on CoIrMnAl

Similar calculations were performed on CoIrMn*Z* (*Z* = Al, Si, Ga and Ge) : *

- VASP used in combination with the projector augmented wave method.
- GGA used as an exchange correlation potential.
    - Energy cutoff : 500 eV for the plane waves.
    - *k*-mesh of 16 × 16 × 16.
    - Energy and the force tolerance : 10 μeV and 10 meV $Å^{-1}$, respectively.

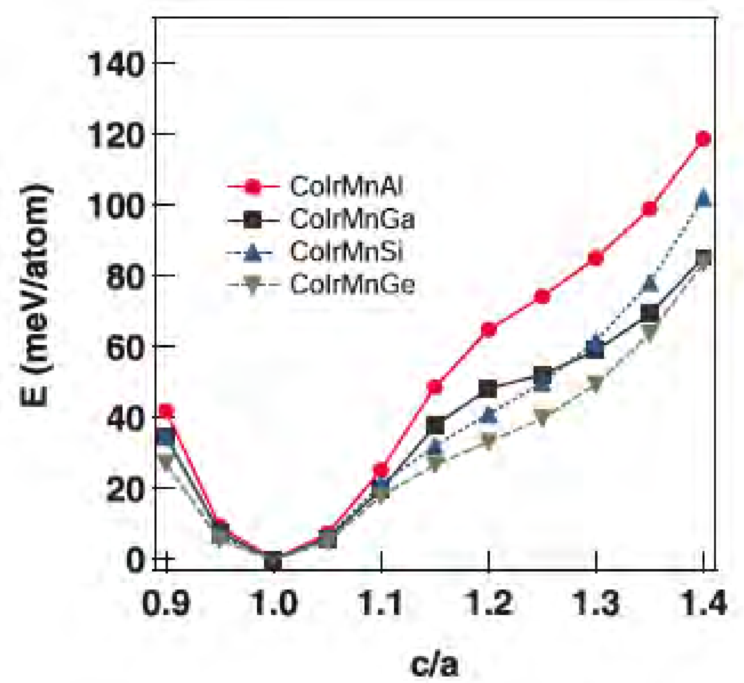

Material	a (Å)	μ_{total} (μ_B)	μ_{Co} (μ_B)	μ_{Ir} (μ_B)	μ_{Mn} (μ_B)	μ_Z (μ_B)	T_C (K)
CoIrMnAl	5.905	4.03	0.95	0.16	2.95	−0.02	584
CoIrMnSi	5.860	5.00	1.32	0.32	3.29	0.00	1020
CoIrMnGa	5.931	4.09	0.97	0.14	3.00	−0.07	517
CoIrMnGe	5.964	5.00	1.31	0.29	3.32	−0.01	956
Co_2MnSi	5.630	5.00	1.02	–	2.99	−0.03	1204
	5.65[b]	5.00[c]					985[b]

* T. Roy *et al.*, *J. Magn. Magn. Mater.* **498**, 166092 (2020).

Density of States of CoIrMn*Z*

Calculated density of states (DOS) on CoIrMn*Z* (*Z* = Al, Si, Ga and Ge) : *

- Spin-polarised and atom-resolved DOS of CoIrMn*Z*.

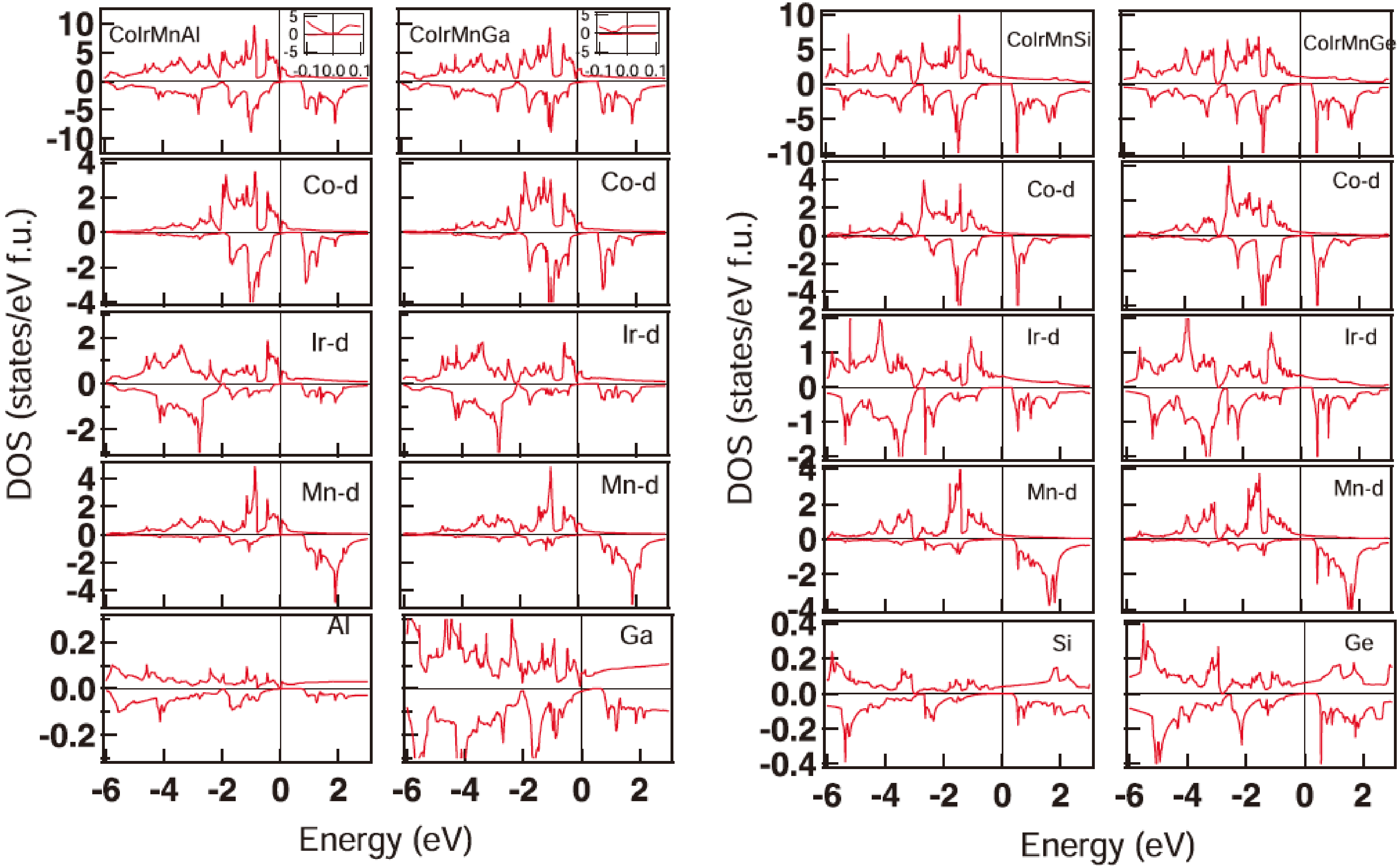

Fermi energy (E_F) = 0.

* T. Roy *et al.*, *J. Magn. Magn. Mater.* **498**, 166092 (2020).

CoIrMnAl Film Deposition

CoIrMnAl films were sputtered : *

- Base pressure : 2 × 10^{-7} Pa.
- MgO (001) // CoIrMnA (50 nm) / Ta (3 nm) grown at room temperature.
- Co : Ir : Mn : Al = 28.1 : 27.6 : 20.7 : 23.6 (at %) measured by an inductively coupled plasma mass spectrometry.
- Post-annealed at 300 ≤ T_a ≤ 600ºC.

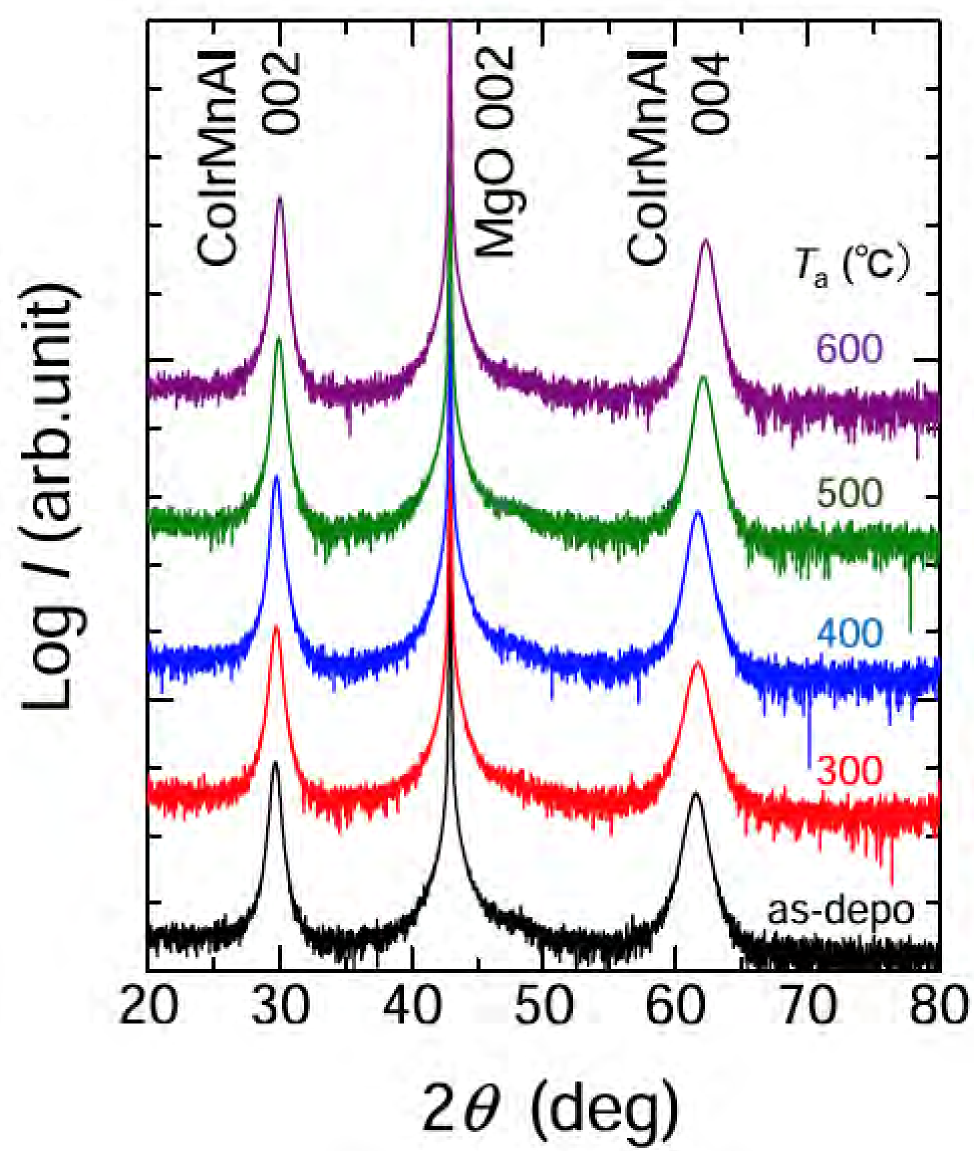

* R. Monma *et al.*, *J. Alloys Comp.* **868**, 159175 (2020).

Magnetisation Curves of CoIrMnAl

Vibrating sample magnetometry (VSM) measurements : *

- Clear magnetisation hysteretic curves measured at room temperature for the films post-annealed at T_a under an in-plane magnetic field.

  → Possible half-metallicity at room temperature.

- Magnetisation curves also measured at elevating temperatures.

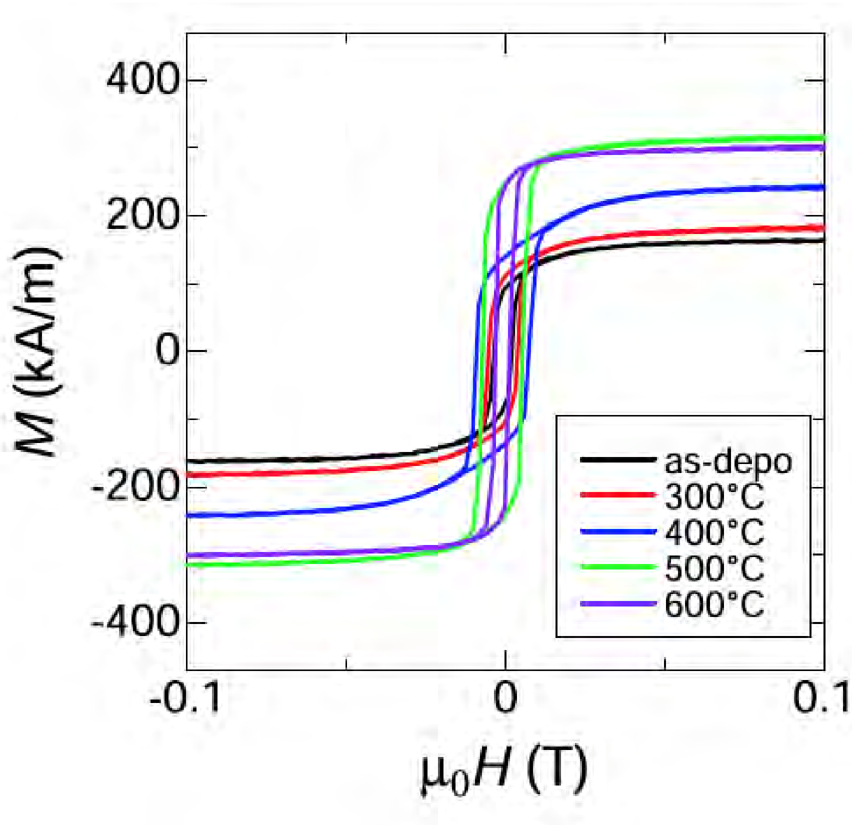

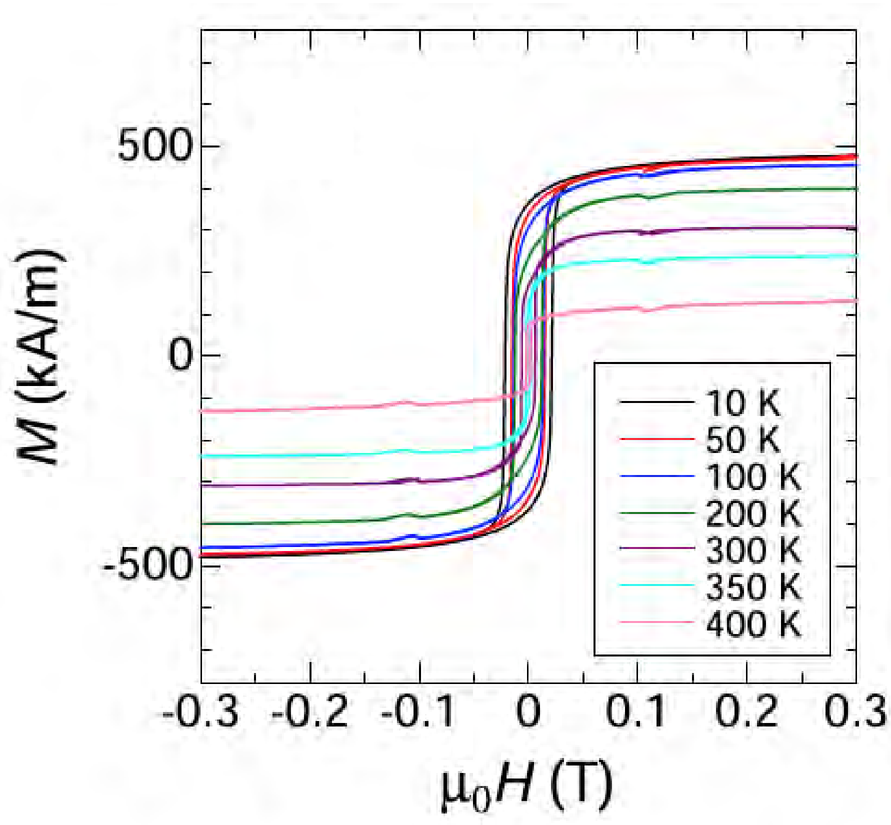

* R. Monma *et al.*, *J. Alloys Comp.* **868**, 159175 (2020).

Structural Analysis of CoIrMnAl

TEM imaging on CoIrMnAl film :

- ~5 nm interfacial roughness at the MgO / CoIrMnAl interface possibly due to the damage induced by sputtering.

  → Possible half-metallicity at room temperature.

- Epitaxial growth observed up to ~17 nm.

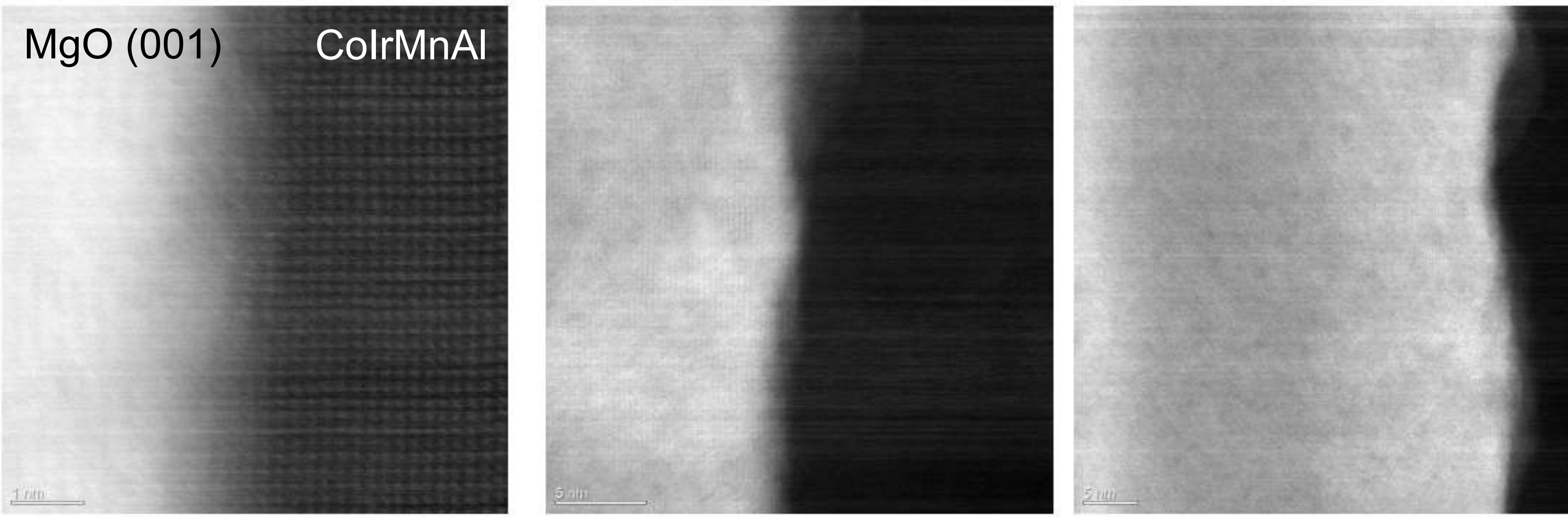

DOS of CoIrMnAl and CoIrMnSi on MgO

DOS calculated for CoIrMn*Z* (*Z* = Al and Si) grown on MgO (001) : *

- Spin-polarised DOS of CoIrMnAl/MgO and CoIrMnSi/MgO interfaces.
- Both cases confirm the metallic nature of the majority spin channel.
- A band gap is formed in the minority spin channel only for the CoIrMnAl / MgO interface.

  → Half-metallic ferromagnet.

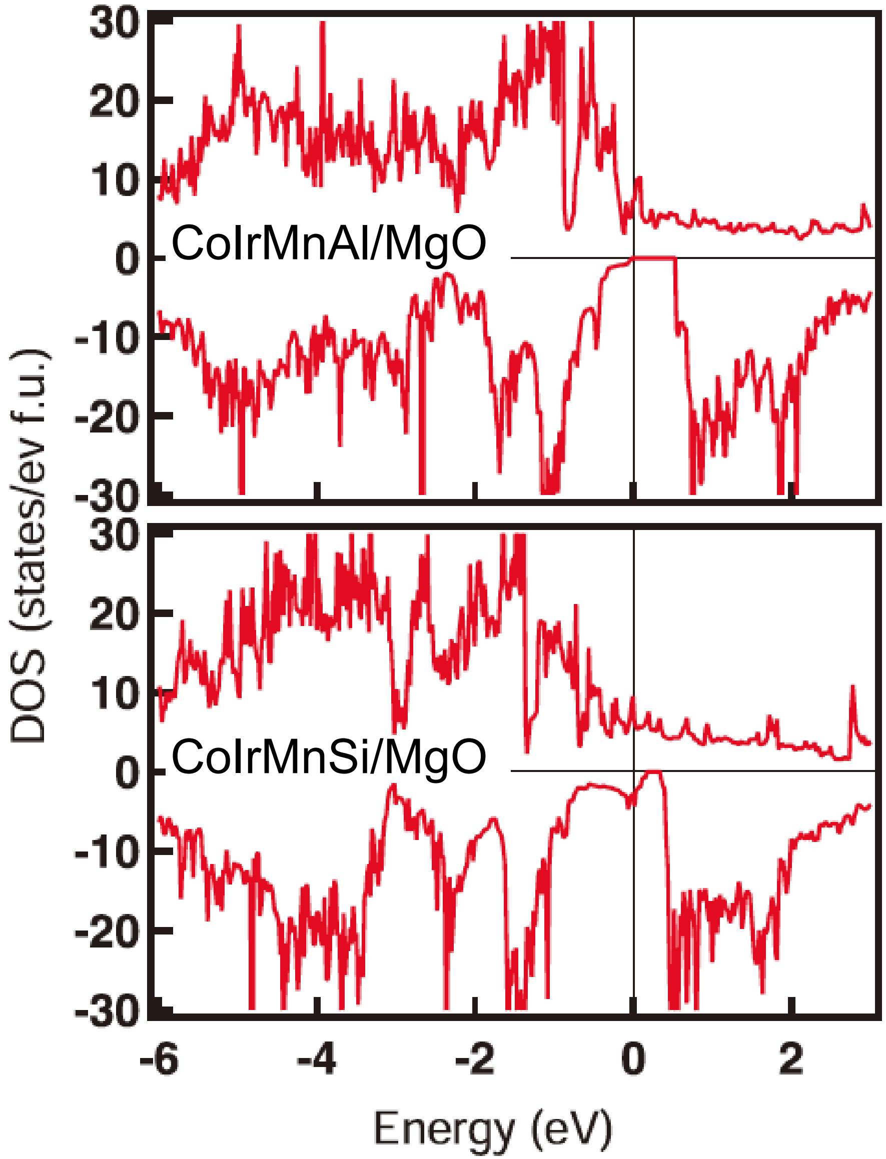

* T. Roy *et al.*, *J. Magn. Magn. Mater.* **498**, 166092 (2020).

Spin Transport at CoIrMnAl and CoIrMnSi / MgO

Spin transmittance was calculated across CoIrMn*Z* (*Z* = Al and Si) / MgO (001) : *

- Transmittance in CoIrMn*Z* / MgO / CoIrMn*Z* (001) as a function of in-plane wave vectors k_x and k_y at E_F in parallel magnetisation of majority spin electrons.

CoIrMnAl / MgO / CoIrMnAl (001)

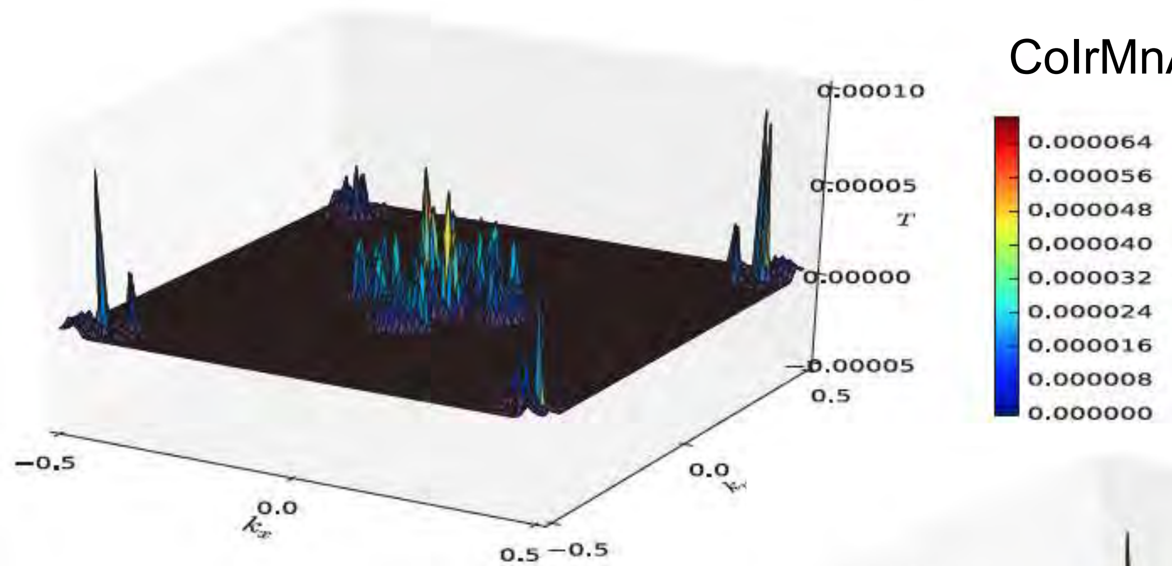

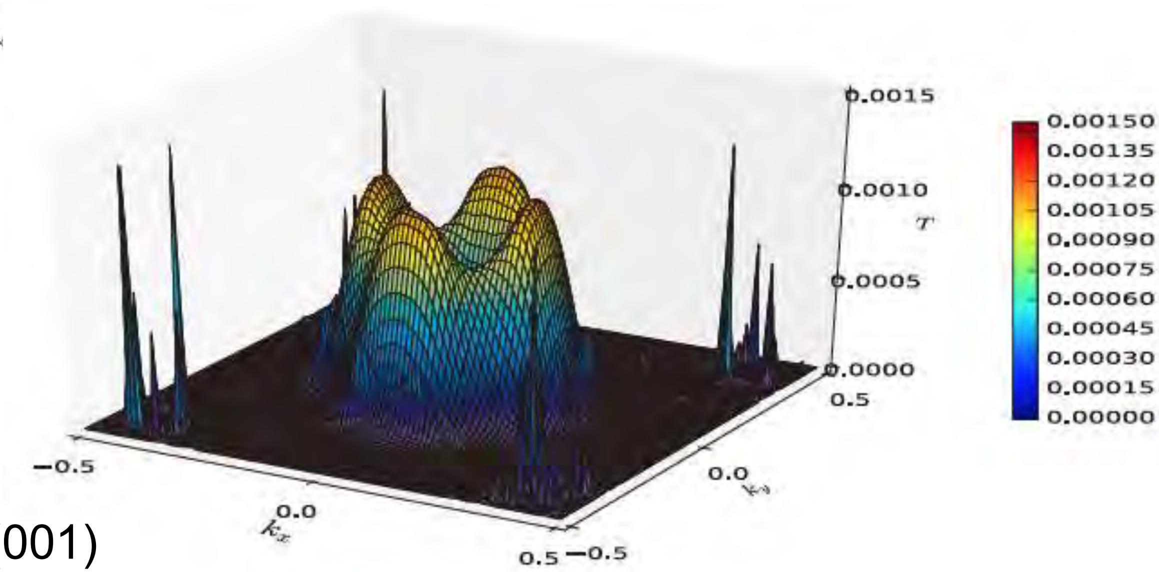

CoIrMnSi / MgO / CoIrMnSi (001)

* T. Roy *et al.*, *J. Magn. Magn. Mater.* **498**, 166092 (2020).

Crystalline Ordering of CoIrMnAl

Comparison between TEM images and QSTEM simulations on CoIrMnAl film :

- Fully ordered *Y* phase confirmed in the epitaxially grown region.

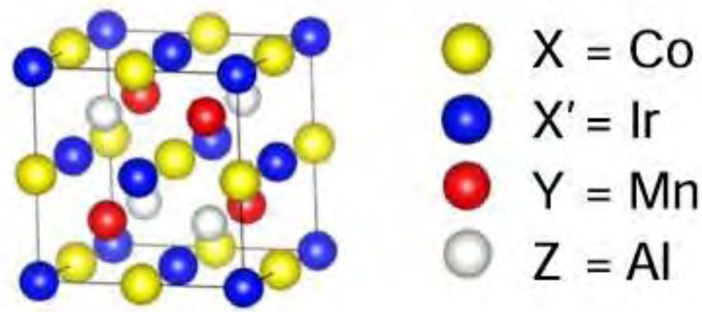

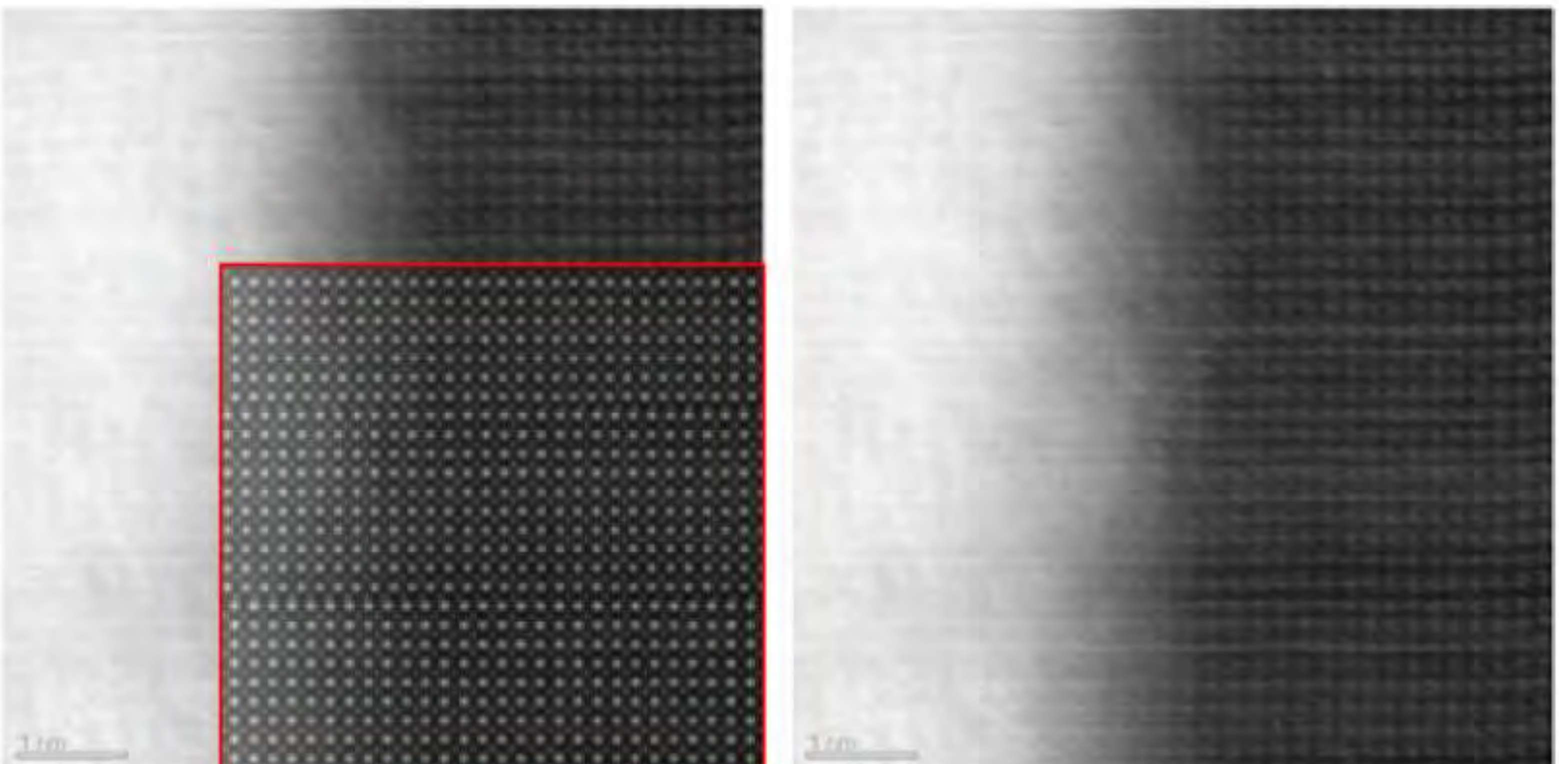

Magnetic Random Access Memory

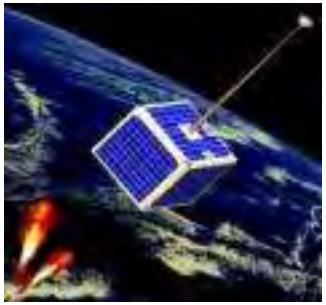

Latest MRAM

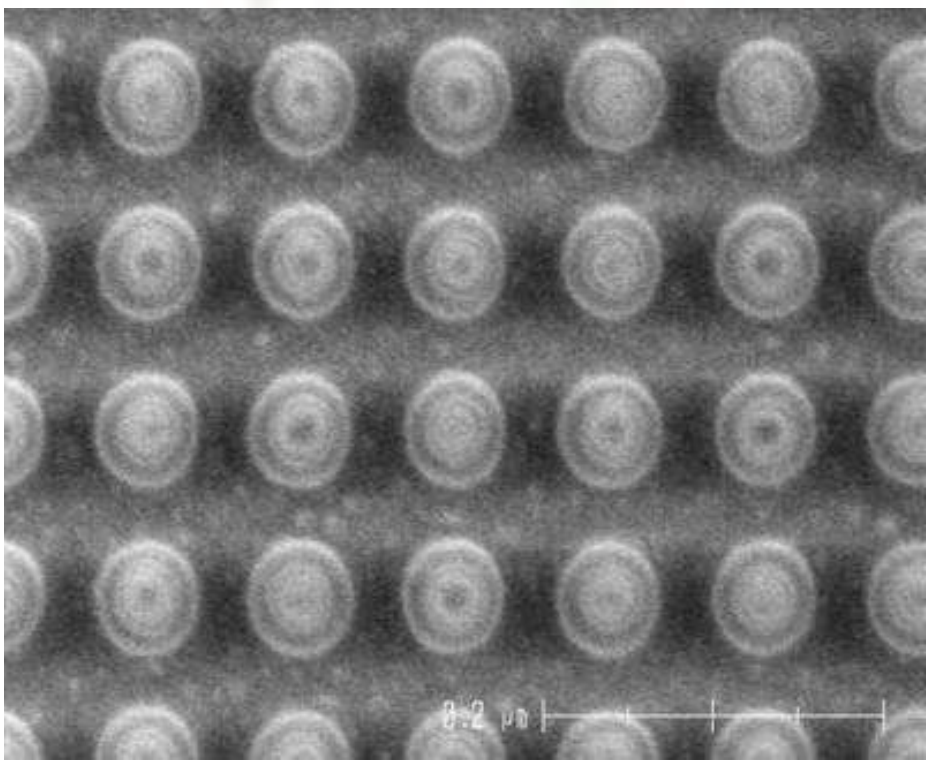

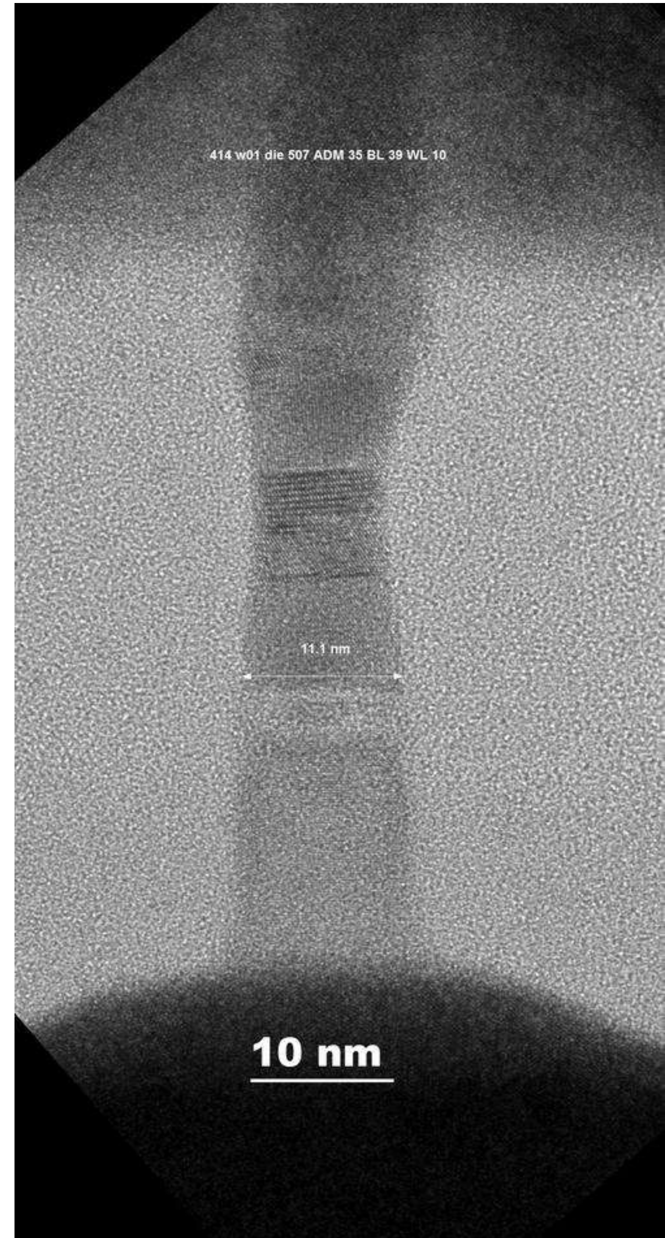

* News from EverSpin, IBM and Toshiba.

Aim of This Study

To develop a new non-destructive imaging method for spintronic devices :

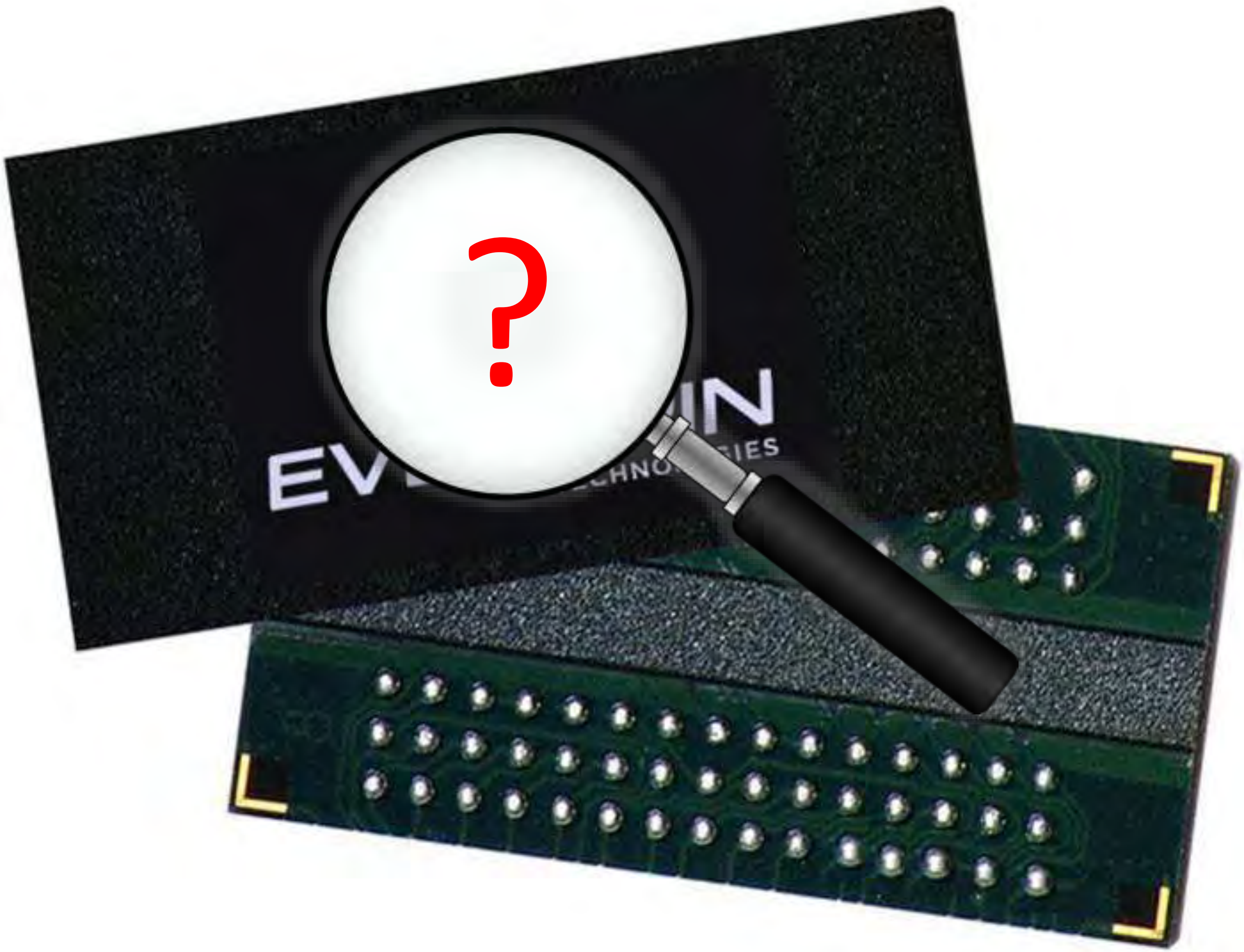

* https://www.everspin.com/; ** A. Hirohata *et al.*, *Nature Commun.* **7**, 12701 (2016).

Magnetic Tunnel Junctions

Heusler-alloy-based MTJ grown and patterned : *

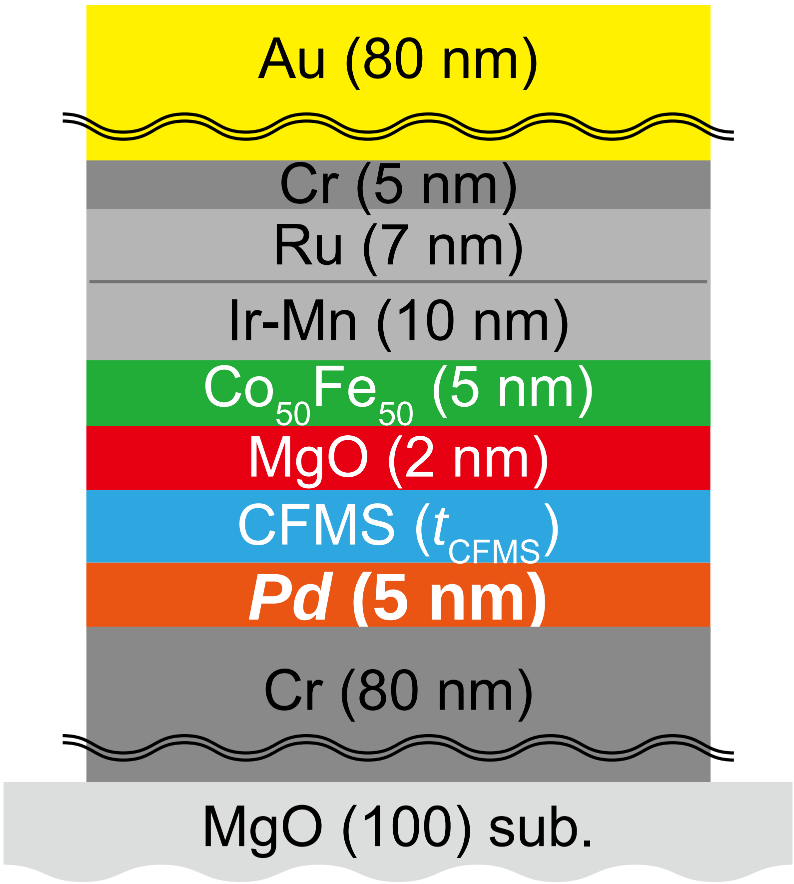

* The Cr/Au electrode deposited after fabricating the pillar shapes.

- t_{CFMS} = 5, 30 (nm)
- T_{anneal} for CFMS = 400ºC
- T_{anneal} for all the stacking = 400ºC

* E. Jackson *et al.*, *Sci. Rep.* **8**, 7585 (2018).

Tunnelling Magnetoresistance

Two distinctive TMR were obtained :

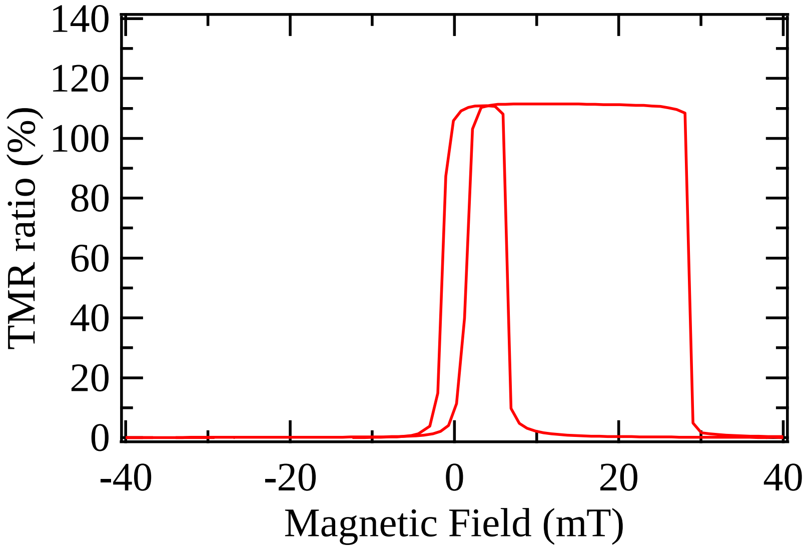

TMR ratio = 110%
RA = 3.8 × 10^4 Ω•μm²

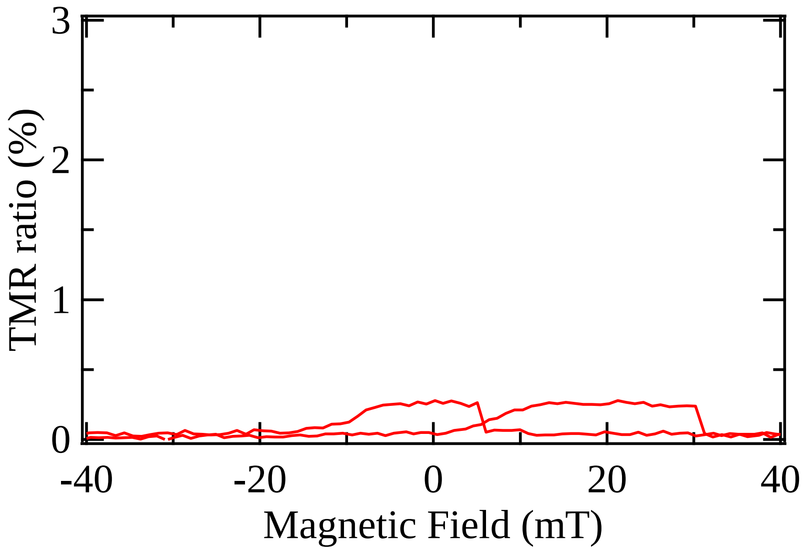

TMR ratio = 0.3%
RA = 5.3 × 10^3 Ω•μm²

* E. Jackson *et al.*, *Sci. Rep.* **8**, 7585 (2018).

CASINO Simulations

Impact voltages between 9 and 12 keV used to penetrate 80 nm Au :

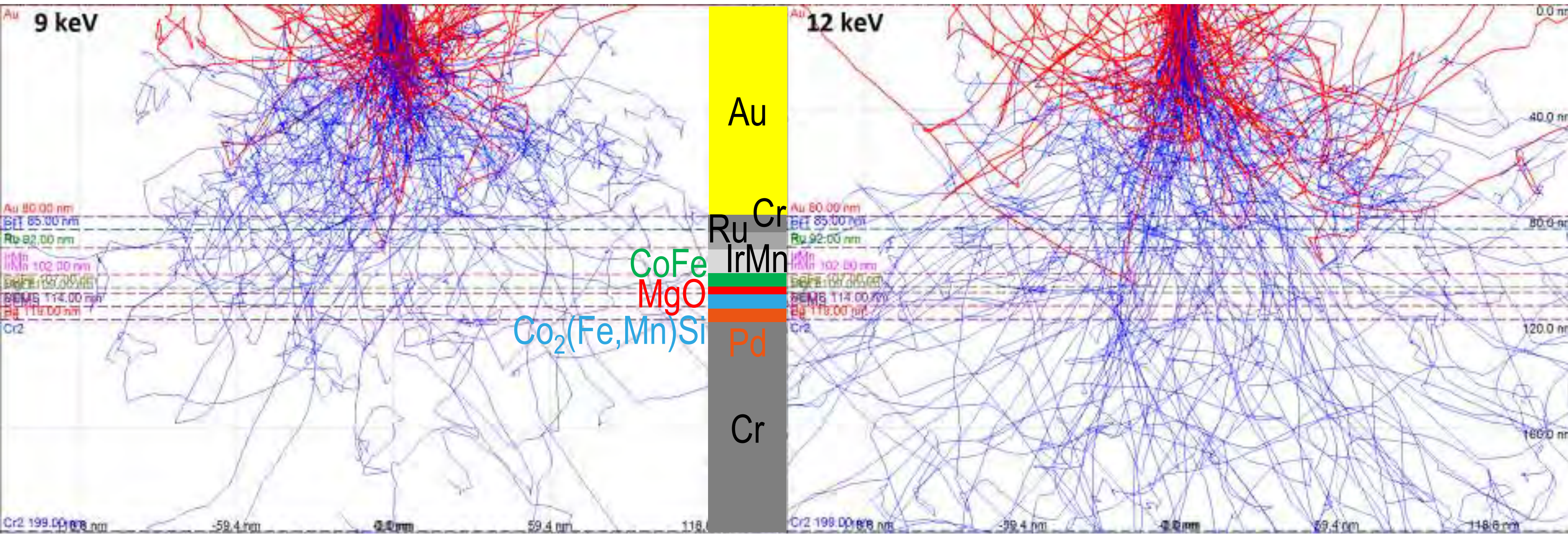

Majority of BSE are generated at the Au top layer.

→ Any defects in Pd / $Co_2(Fe,Mn)Si$ / MgO / CoFe interfaces ?

BSE Imaging on Magnetic Tunnel Junctions

Subtracted images between 11 and 10.5 keV on 15 x 15 µm pillars :

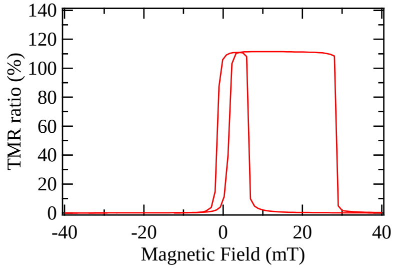

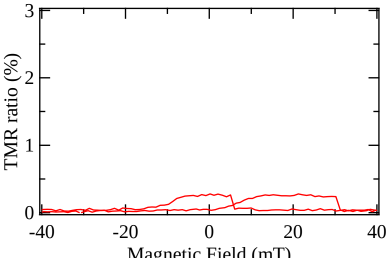

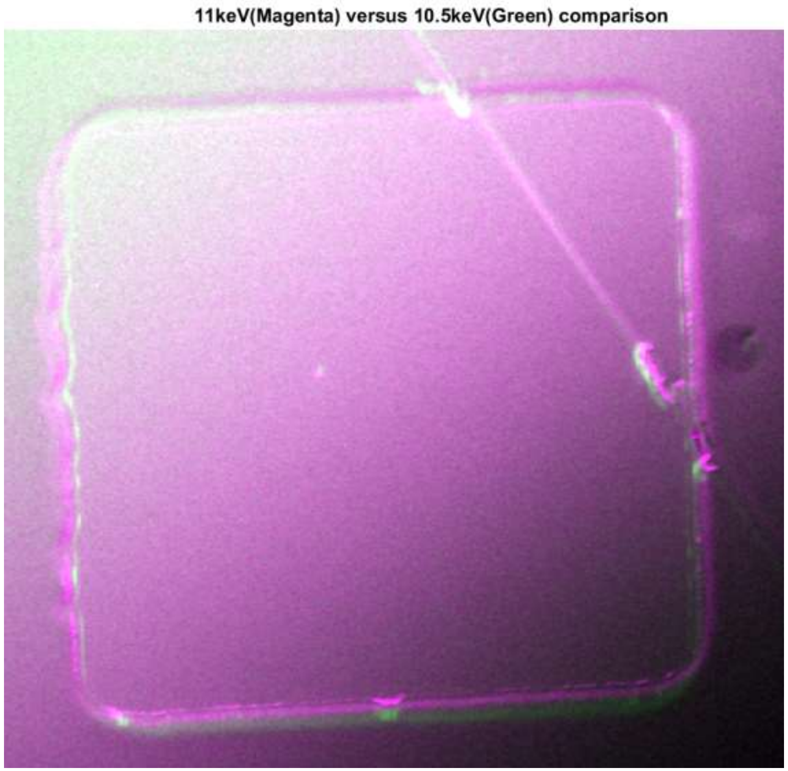

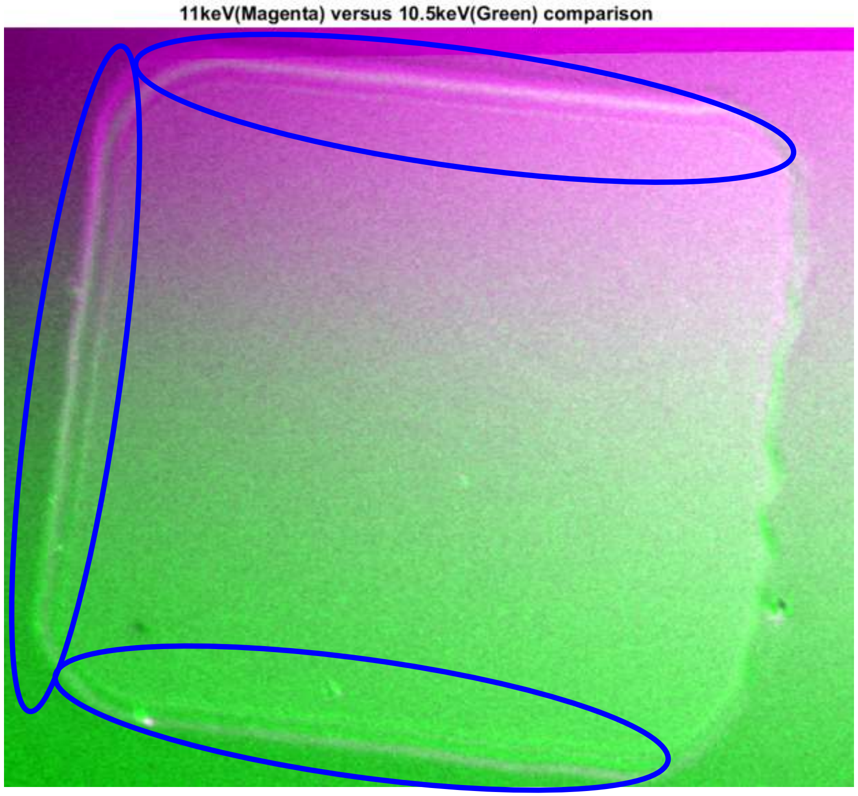

Redeposition ?

EDX Mapping on a High-TMR junction

Energy dispersive X-ray spectroscopy used to identify material distributions:

Base(4)

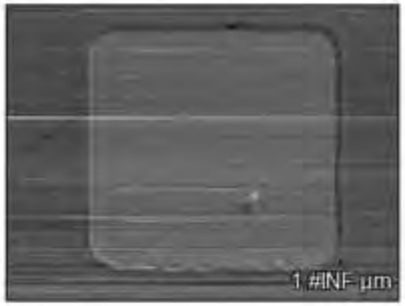

Base(2)

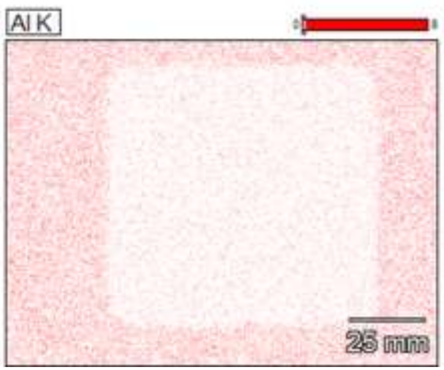

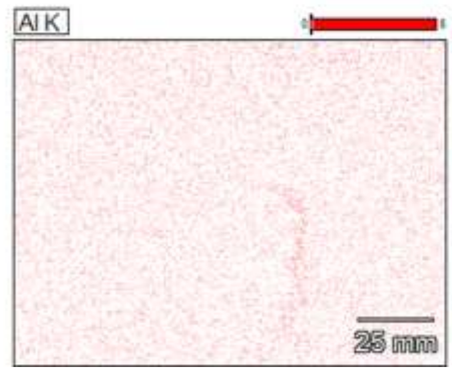

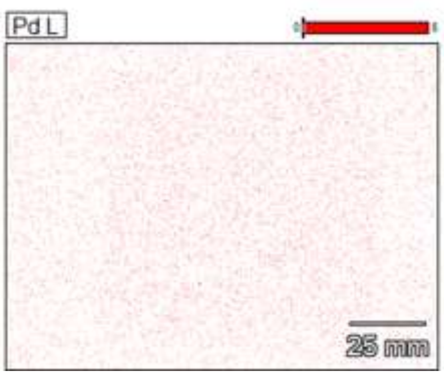

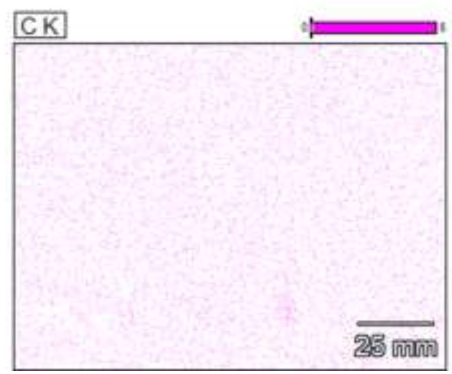

First Principles Calculations on NiCrMnSi

New ferromagnetic Heusler alloys predicted : *

- Vienna *ab-initio* simulation package(VASP) was used in combination with the projector augmented wave method.
- Generalised gradient approximation (GGA) was used as an exchange correlation potential.
  - Energy cutoff : 500 eV for the plane waves.
  - *k*-mesh of 8 × 8 × 8.
  - Energy and the force tolerance : 10 μeV and 10 meV Å^{-1}, respectively.

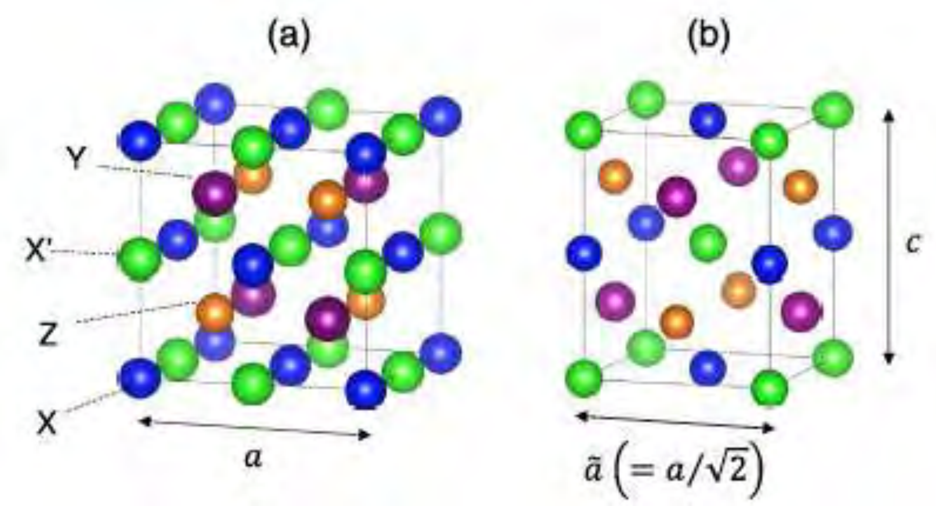

XX′YZ	Structure	$\Delta E_{XX'YZ}$ (eV f.u.$^{-1}$)	a (Å)	c/a
NiCrMnSi	cubic	−1.033	5.710	
	tetragonal	−1.151	5.285	1.270
MnNiCrSi	cubic	−0.974	5.681	
	tetragonal	−1.118	5.213	1.254
MnCrNiSi	cubic	−0.402	5.658	
	tetragonal	−0.794	5.046	1.457

* Y. Onodera *et al.*, *Jpn. J. Appl. Phys.* **59**, 073003 (2020).

Magnetic Calculations

Half-metallic ferromagnetic Heusler alloys predicted : *

- Magnetic interactions were calculated using Green's function based on the spin-polarised relativistic Korringa-Kohn-Rostoker method (SPR-KKR).
  - Heisenberg exchange coupling constant within a real space approach.
  - Curie temperature (T_C) estimated using the Heisenberg exchange coupling constant with mean-field approximation.
- Full-potential method and GGA were used for the self-consistent-field calculations.
  - 824 irreducible *k*-points for the Brillouin zone integration.
  - Angular momentum expansion up to three used for each atom.
  - 90 energy points on the complex energy path used.

Material	T_c (K)	P (%)	a (nm)	c/a	m_{tot} (μ_B/f.u.)
NiCrMnSi	1200	88	0.528	1.27	0.95 (0.13, −1.79, 2.61)
Co_2MnSi	1204	100	0.563	1.00	5.00 (1.02, 2.99)

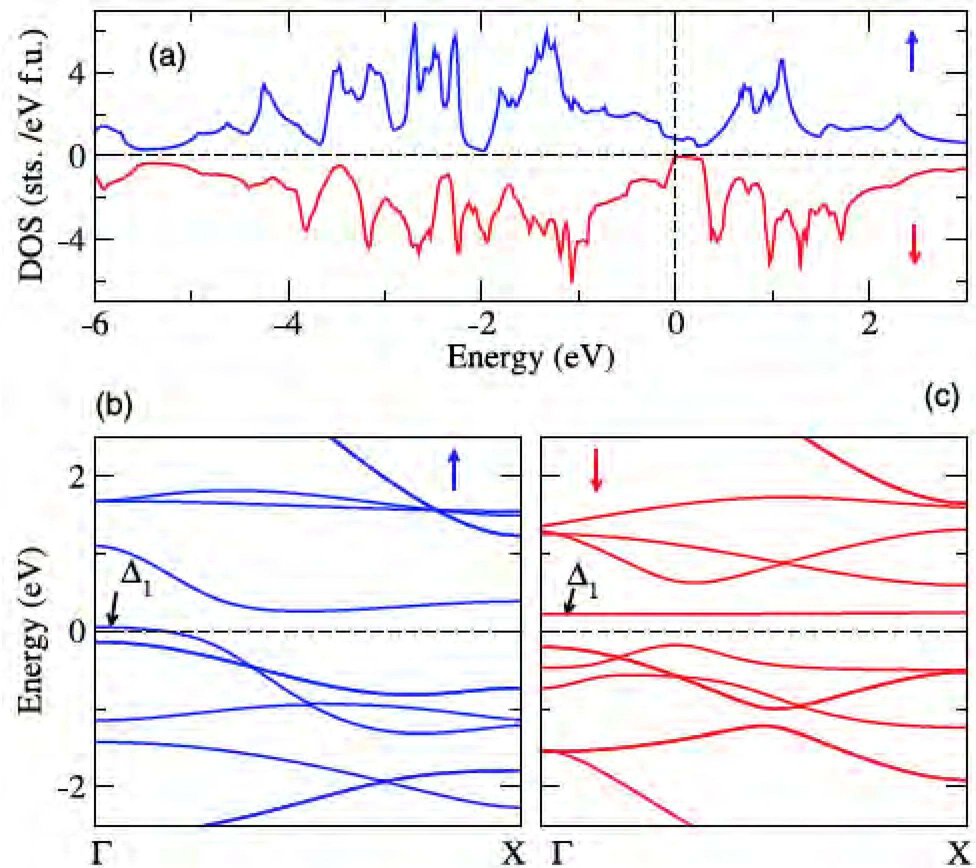

* Y. Onodera *et al.*, *Jpn. J. Appl. Phys.* **59**, 073003 (2020).

NiCrMnSi Film Deposition

NiCrMnSi films were sputtered : *

- Base pressure : 2 × 10^{-7} Pa.
- MgO (001) // NiCrMnSi (100 nm) / Ta (3 nm) grown at room temperature.
- Ni : Cr : Mn : Si = 25.9 : 29.5 : 23.0 : 21.6 (at %) measured by an inductively coupled plasma mass spectrometry.
- Post-annealed at
  $500 \leq T_a \leq 800$ ºC.

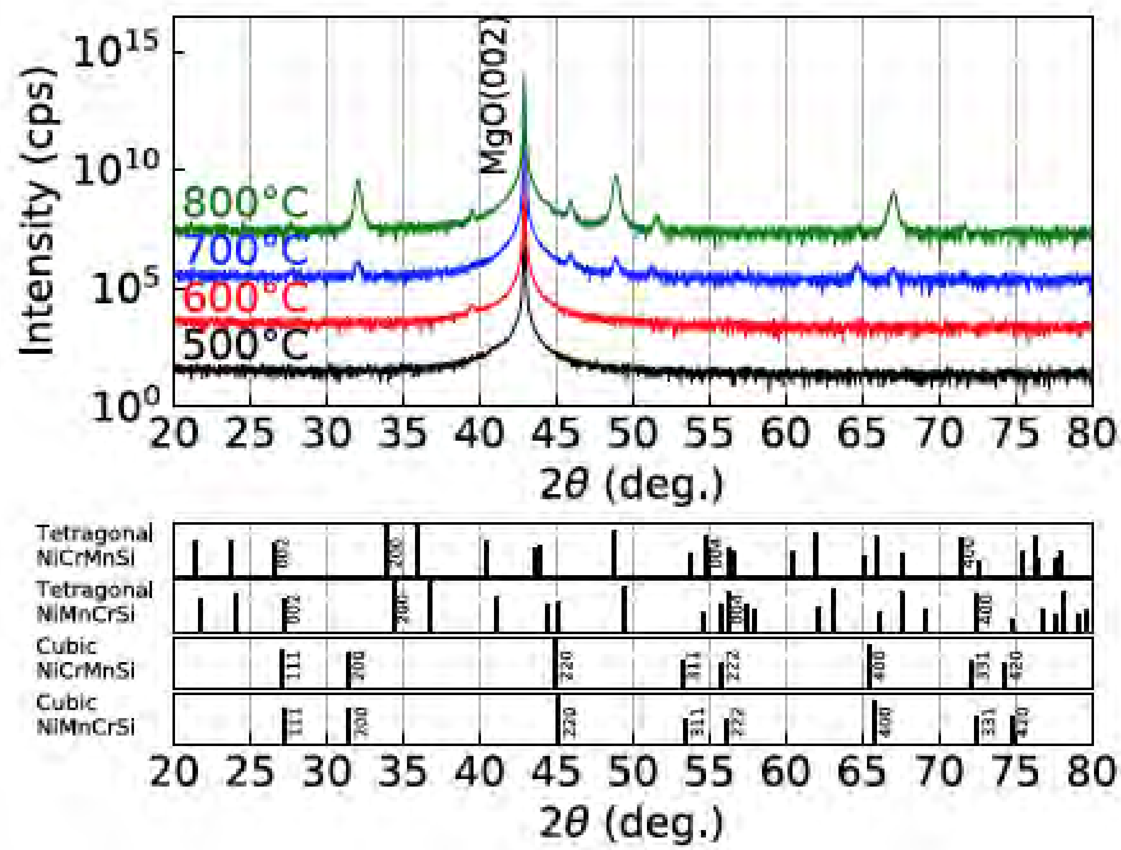

* Y. Onodera *et al.*, *Jpn. J. Appl. Phys.* **59**, 073003 (2020).

Structural Analysis on NiCrMnSi

Transmission electron micrographs (TEM) : *

- The sample deposited at 500ºC shows short-range crystallisation phases but polycrystalline nature.
- The sample grown at 700ºC shows clear grains.
    - Diffraction spots observed.
    - Multiple crystalline phases with overlapped each other.

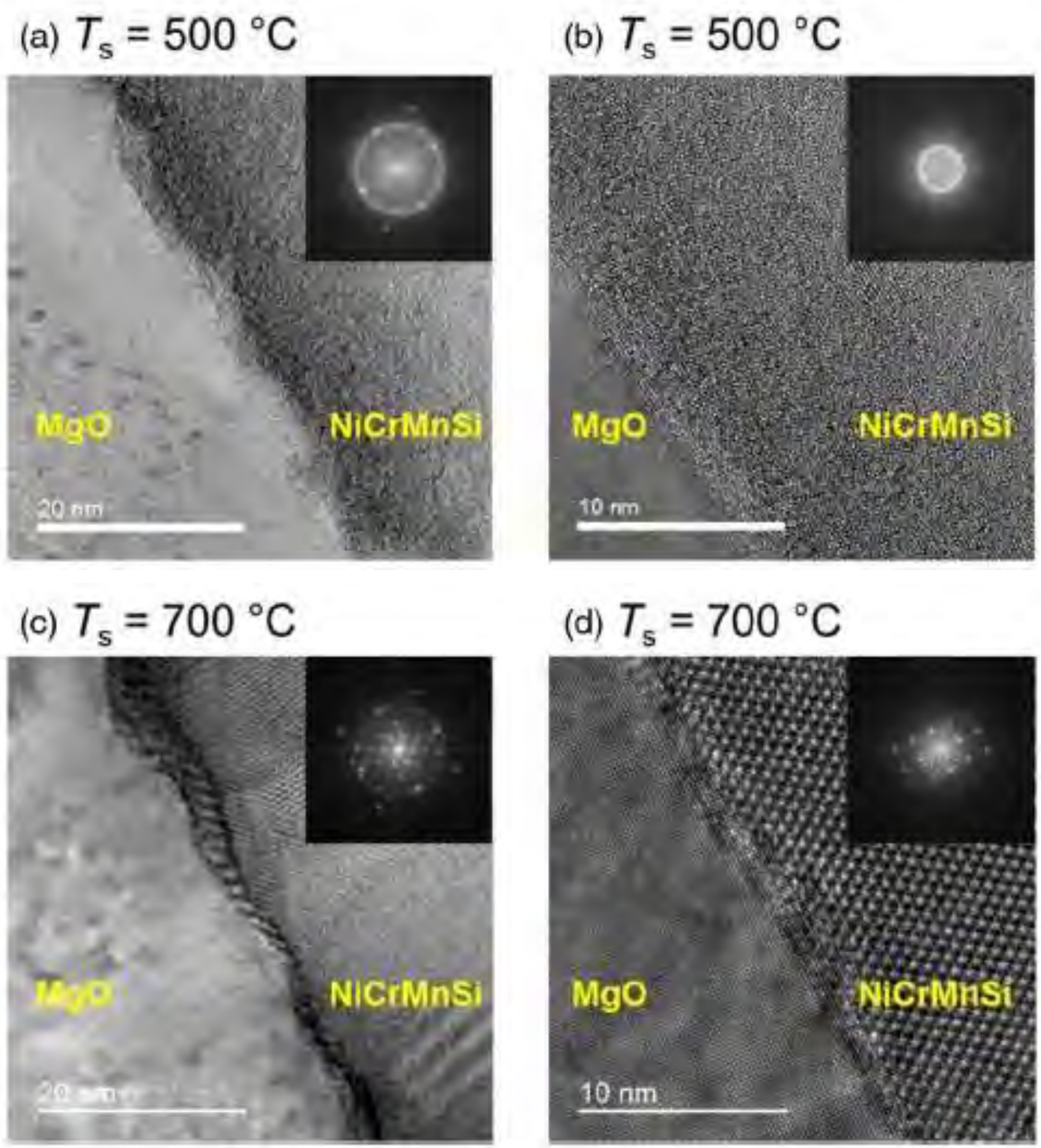

* Y. Onodera *et al.*, *Jpn. J. Appl. Phys.* **59**, 073003 (2020).

Compositional Analysis on NiCrMnSi

Energy dispersive X-ray spectroscopy (EDX) mapping : *

- The sample deposited at 500ºC shows homogeneous distribution of all elements throughout the film.
- The sample grown at 700ºC shows segregation for Ni and Cr atoms.

  → The Ni-rich Cr-rich phases spatially separated.

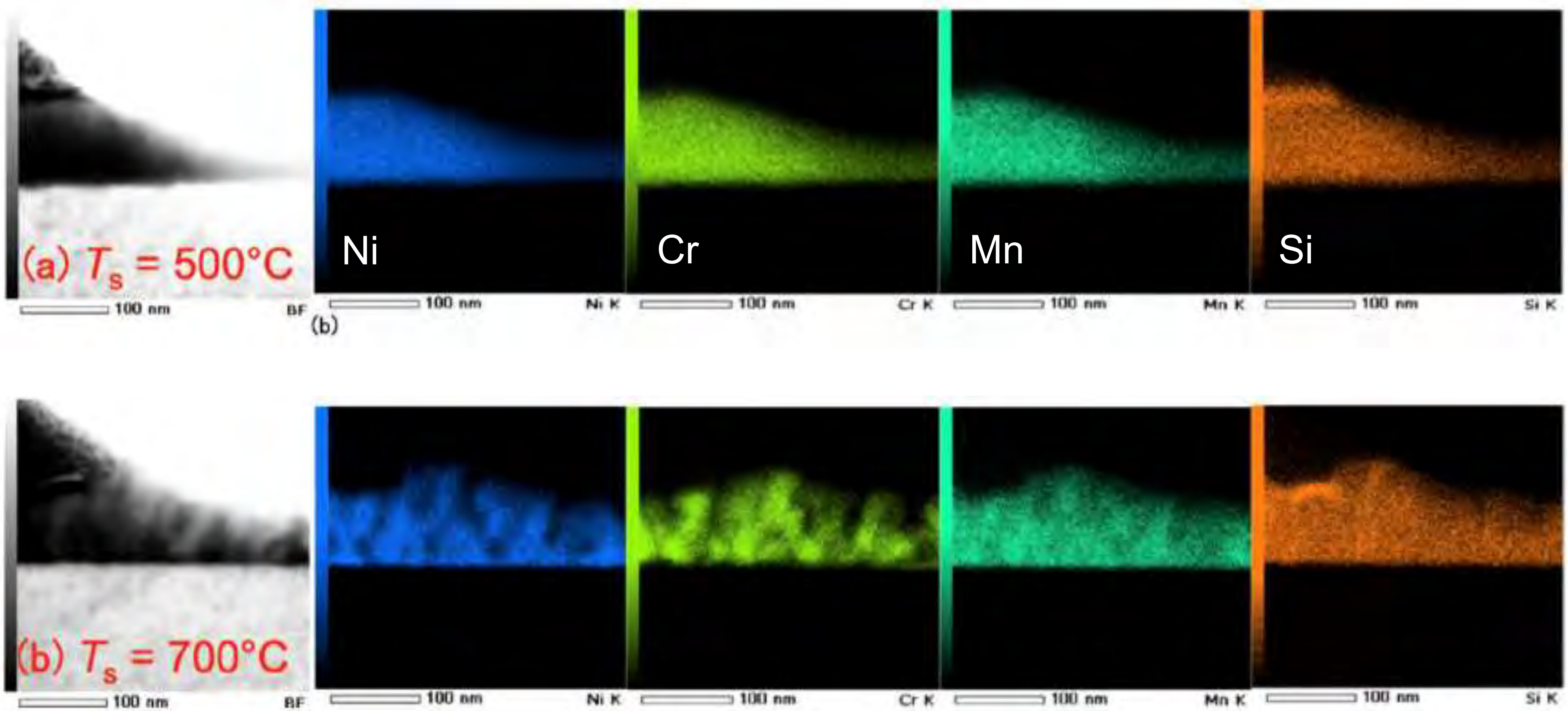

* Y. Onodera *et al.*, *Jpn. J. Appl. Phys.* **59**, 073003 (2020).

Magnetisation Curves of NiCrMnSi

Magneto-optical Kerr effect (MOKE) measurements : *

- Polar MOKE shows out-of-plane magnetisation curves.
- No ferromagnetism was observed for all the samples.

  → Paramagnetism or antiferromagnetism at room temperature.

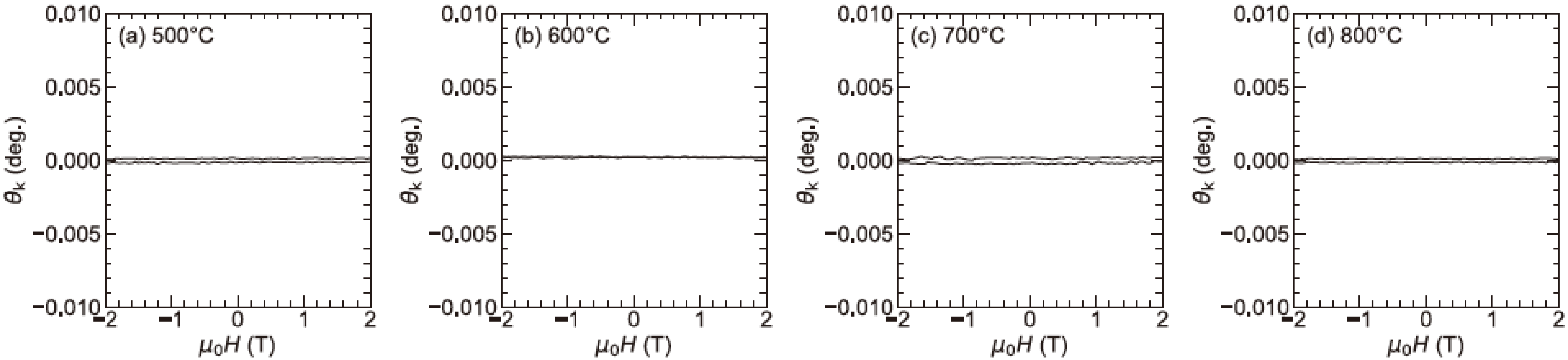

* Y. Onodera *et al.*, *Jpn. J. Appl. Phys.* **59**, 073003 (2020).

Low Temperature Crystsallisation

Layer-by-layer crystallisation on (110) surface :

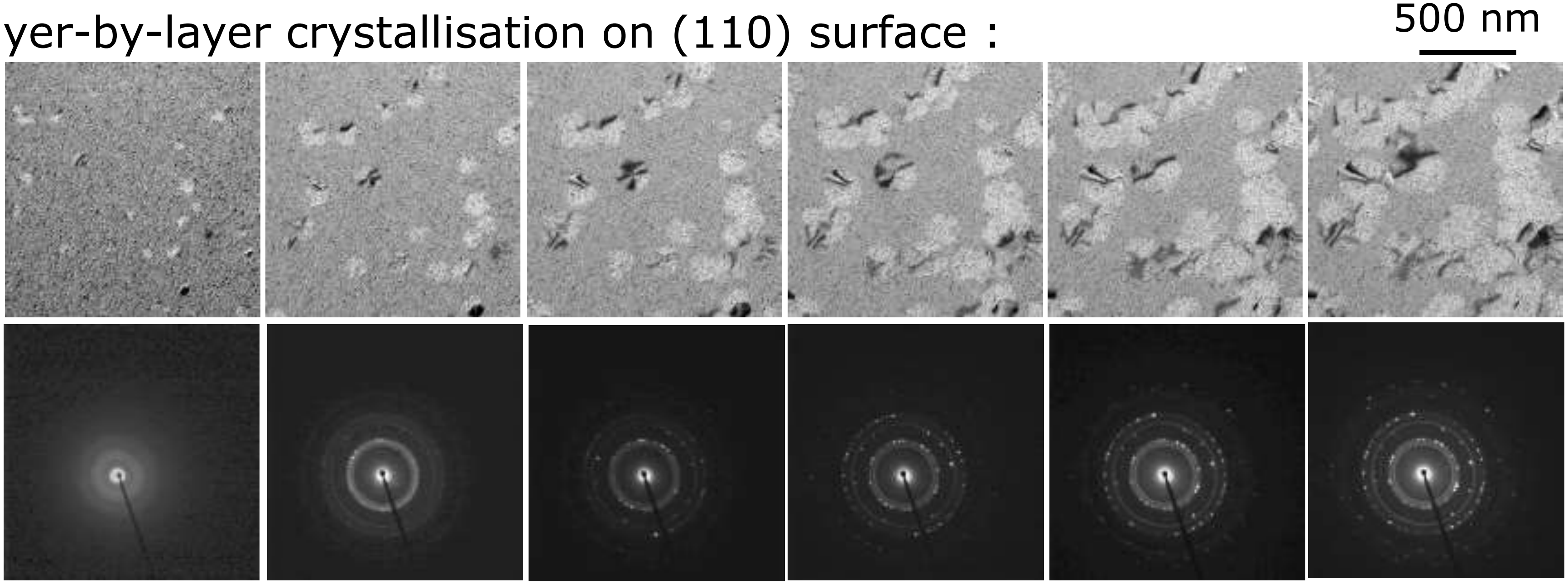

20 → 120 mins

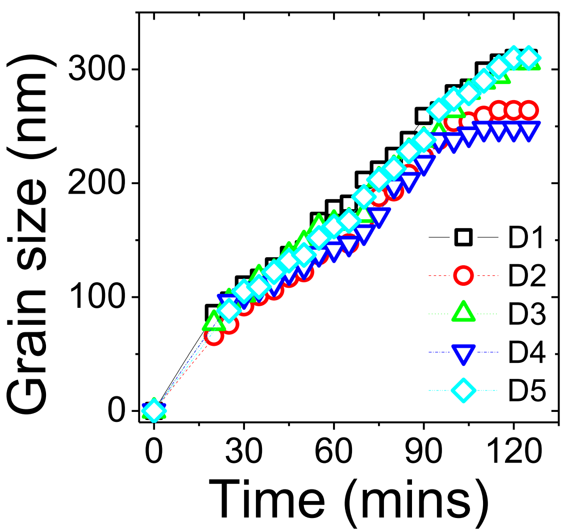

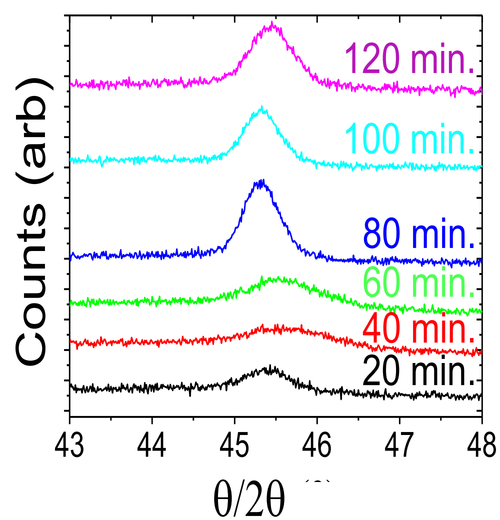

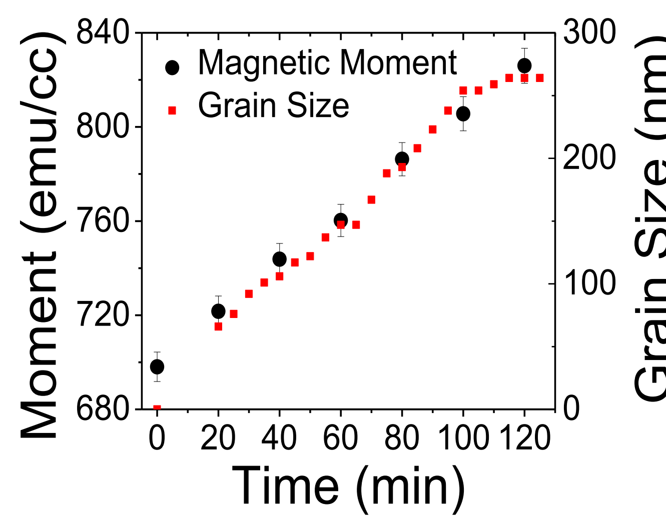

* J. Sagar *et al.*, *Appl. Phys. Lett.* **105**, 032401 (2014).

Magnetic Characterisation

$Co_2Fe(Al,Si)$ / W / $Co_2Fe(Al,Si)$ trilayers : *

- AF coupling is not achieved in CFAS/W/CFAS.
- Low T_S film has strong intergranular exchange coupling.
- This gives a highly square, low H_C loop.
- Higher T_S → 50% of the reversal is via domain rotation.
- The remainder is via nucleation and domain wall pinning.
- The is similar to CoFe and would be suitable for a GMR device.

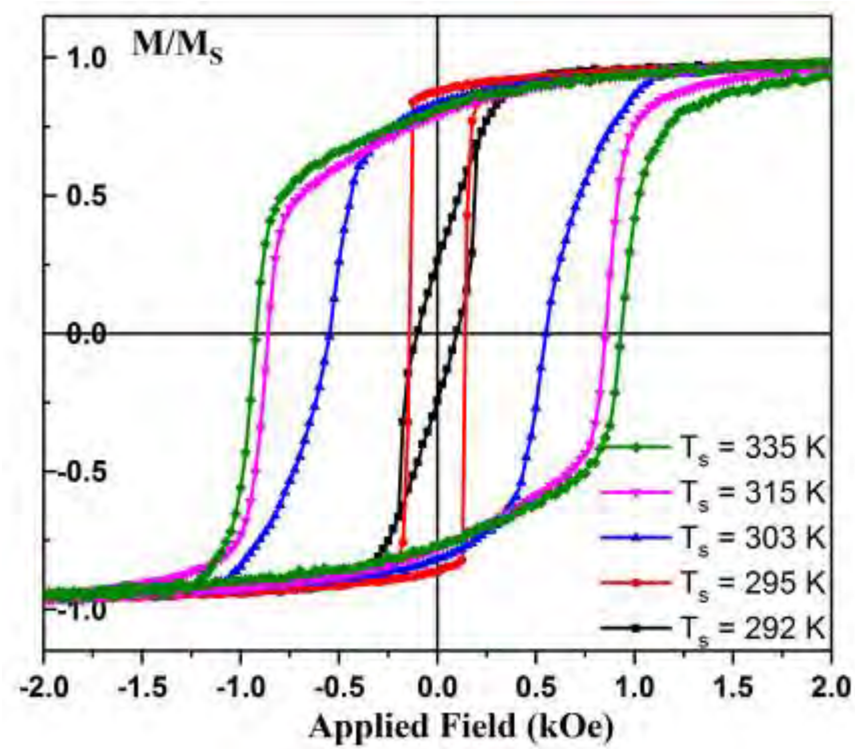

* W. Frost *et al.*, *J. Magn. Magn. Mater.* **484**, 100 (2019).

Device Measurements

$Co_2Fe(Al,Si)$ / Ag / $Co_2Fe(Al,Si)$ trilayers : *

- A 3 nm layer of Ag provided a loop with two distinct switches dependent on layer thickness.
- A small GMR of 0.025% was observed perpendicular-to-plane for device of (1 x 0.5) μm^2.
- Switching occurs at the same field as in the *M-H* loop, confirming layer thickness dependent switching.

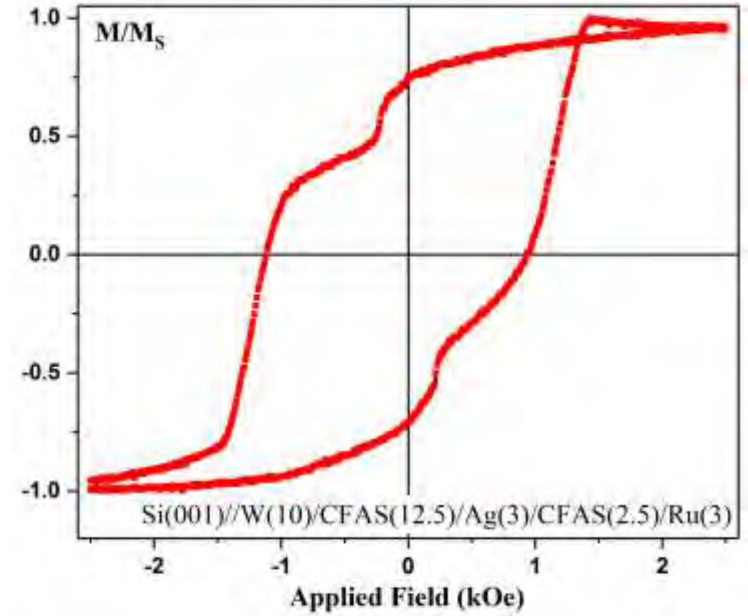

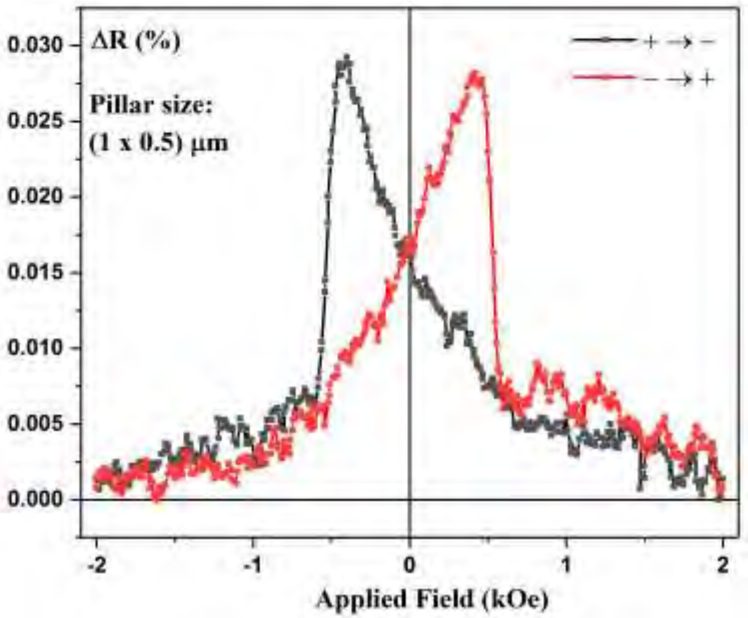

* A. Hirohata *et al.*, *Materials*, **11**, 105 (2018).

Requirements for Spintronic Devices

Resistance-area product (*RA*) and magnetoresistance (MR) ratios : *

- Giant magnetoresistive (GMR) junctions reuire further increase in their MR ratios.
  - → Higher spin polarisation
  - → Smaller temperature dependence

- Magnetic tunnel junctions (MTJs) require further reduction in *RA*.
  - → Thinner tunnel barrier
  - → Smaller temperature dependence

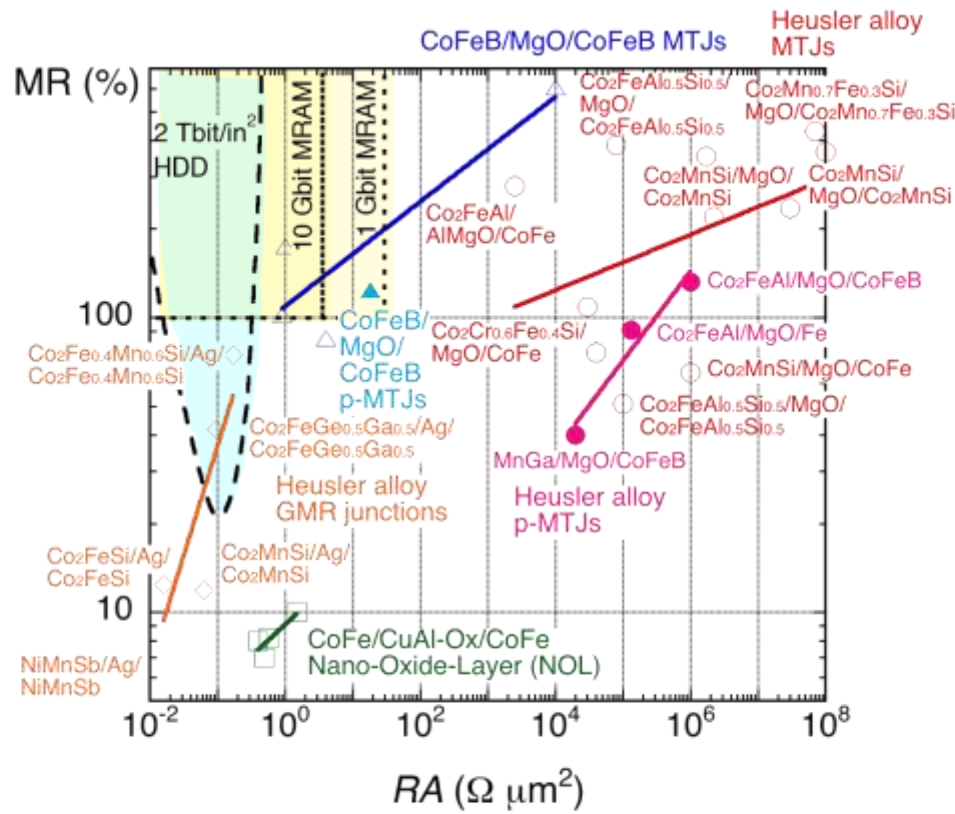

* A. Hirohata *et al.*, *Materials* **11**, 105 (2018).

Recent Development in TMR ratios

Tunnel magnetoresistance (TMR) ratios : *

- Amorphous barriers achieved TMR ratios of < 100% at room temperature (RT).
- Epitaxial barriers improved TMR ratios up to ~ 600% at RT due to the coherent tunnelling.
- Half-metallic Heusler alloys show similar TMR ratios at RT.

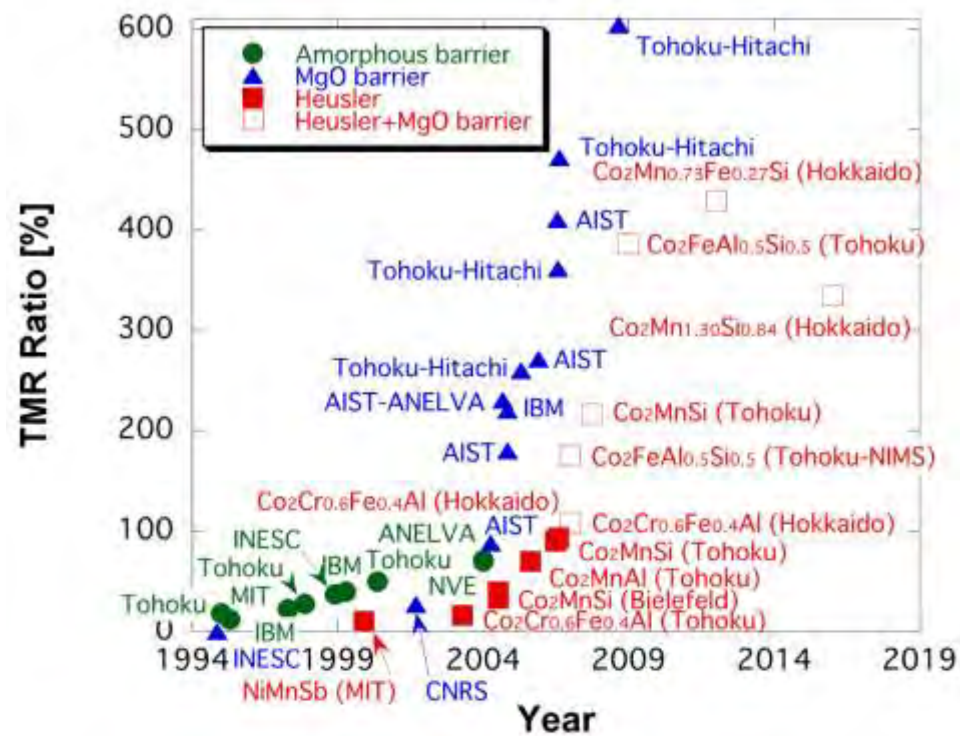

* A. Hirohata *et al.*, *J. Magn. Magn. Mater.* **509**, 166711 (2020).

Temperature Dependence of TMR ratios

Tunnel magnetoresistance (TMR) ratios : *

- Amorphous barriers follow the empirical law of $T^{3/2}$.
- Epitaxial barriers show faster decrease than the empirical law of $T^{3/2}$.

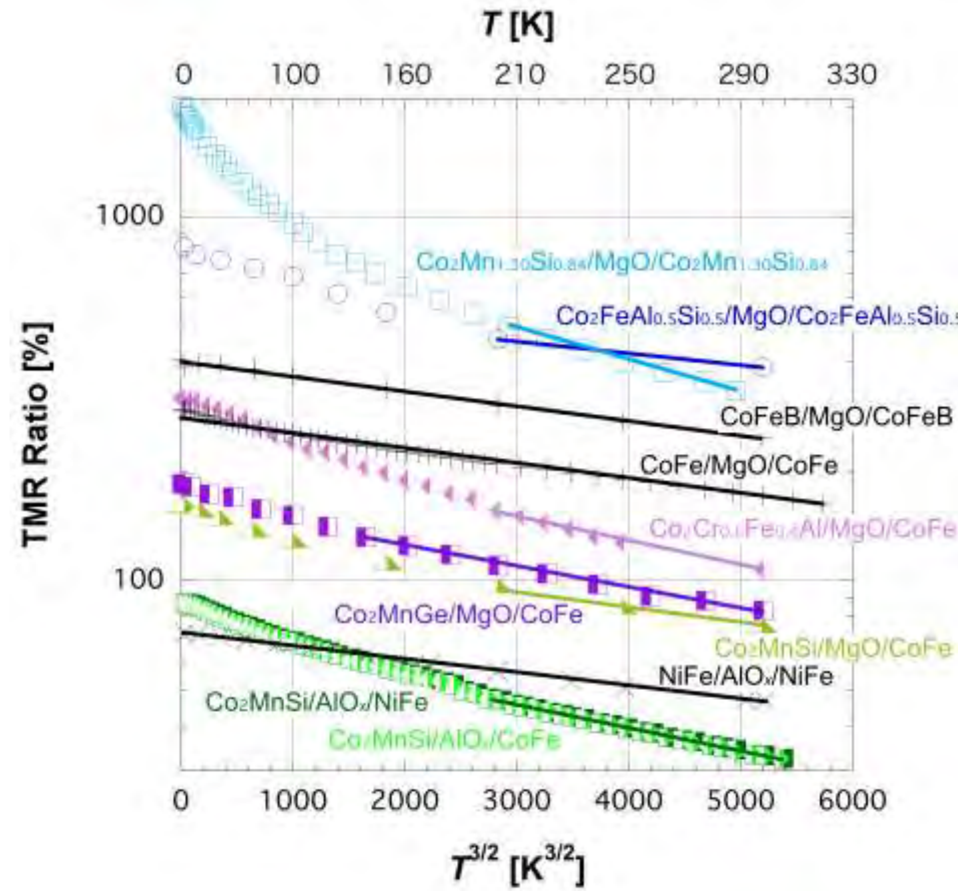

* A. Hirohata *et al.*, *J. Magn. Magn. Mater.* **509**, 166711 (2020).

Metastable bcc Co-Mn Alloys

In Co_xMn_{100-x} alloys : *

- A body-centred cubic (bcc) phase can be obtained above approximately x = 75.
- By reducing x, the crystalline phase of Co_xMn_{100-x} becomes face-centred cubic (fcc) or hexagonal closed packing (hcp) below x = 60 ~ 70.
- The lattice constant of CoMn was evaluated to be controlled approximately between 0.285 nm and 0.290 nm.
- Enhanced moments in bcc $Co_{1-x}Mn_x$ on MgO(001). **

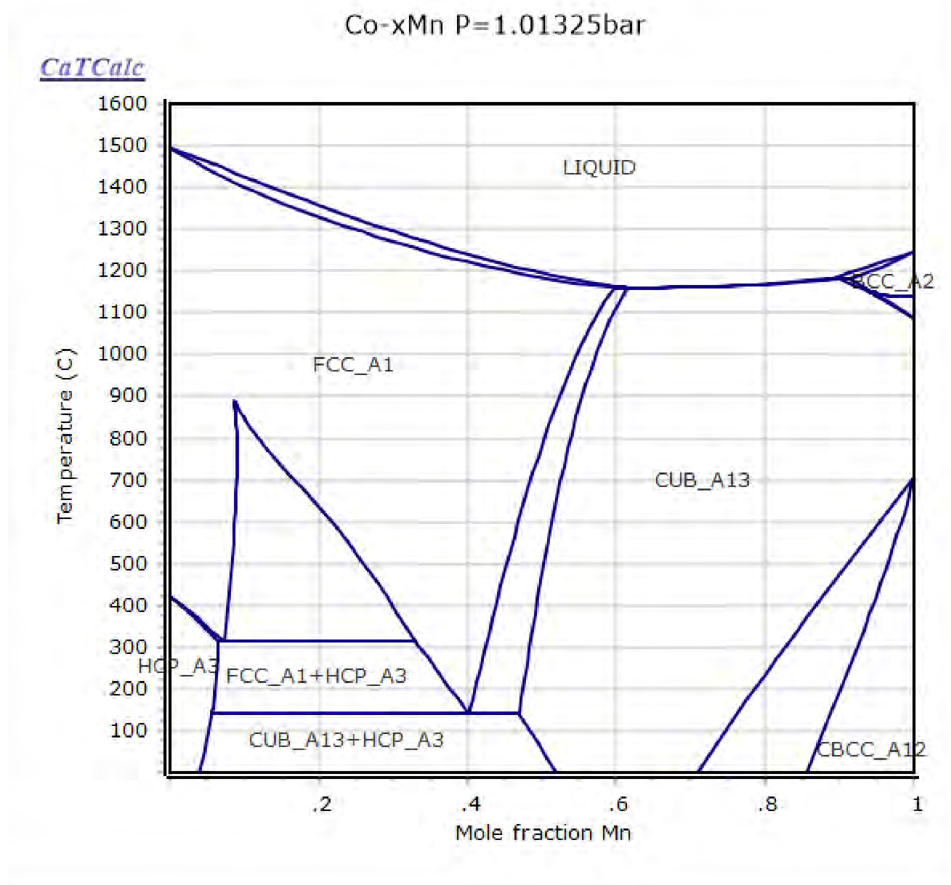

* J K. Ishida and T. Nishizawa, *Bull. Alloy Phase Diagrams* **11**, 125 (1990); https://sites.google.com/site/catcalcphase/metal/co/co-mn-1

** R.J. Snow *et al.*, *J. Magn. Magn. Mater.* **419**, 490 (2016).

MTJ Fabrication

Ultrahigh vacuum sputtering to grow CoMn-based MTJ multilayers : *

- MgO(001) // Cr (40) / Co_xMn_{100-x} (10) / MgO (2.4) / Co_xMn_{100-x} (4) / Co_3Fe(1.5) / IrMn (10) / Ru (5) (thickness in nm).
- Four different compositions of x = 66, 75, 83 and 86 were employed, allowing to control the lattice constants of the bottom and top electrodes precisely.
- Ti and Au top electrodes used for MTJ patterned by photolithography.
- In order to achieve crystalline engineering in MTJ, *in-situ* annealing was carried out after the deposition of the Cr seed layer and Co_xMn_{100-x} electrodes at 700°C and 200°C, respectively.

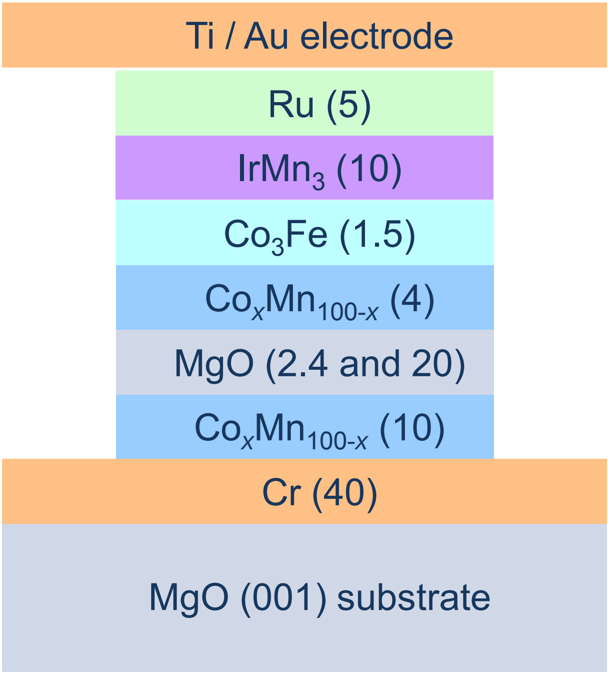

* K. Kunimatsu *et al.*, *Jpn. J. Appl. Phys.* **58**, 080908 (2019); *App. Phys. Exp.* **13**, 083007 (2020)

Tunnelling Magnetoresistance

Co_xMn_{100-x} MTJs (x = 66, 75, 83 and 86) :

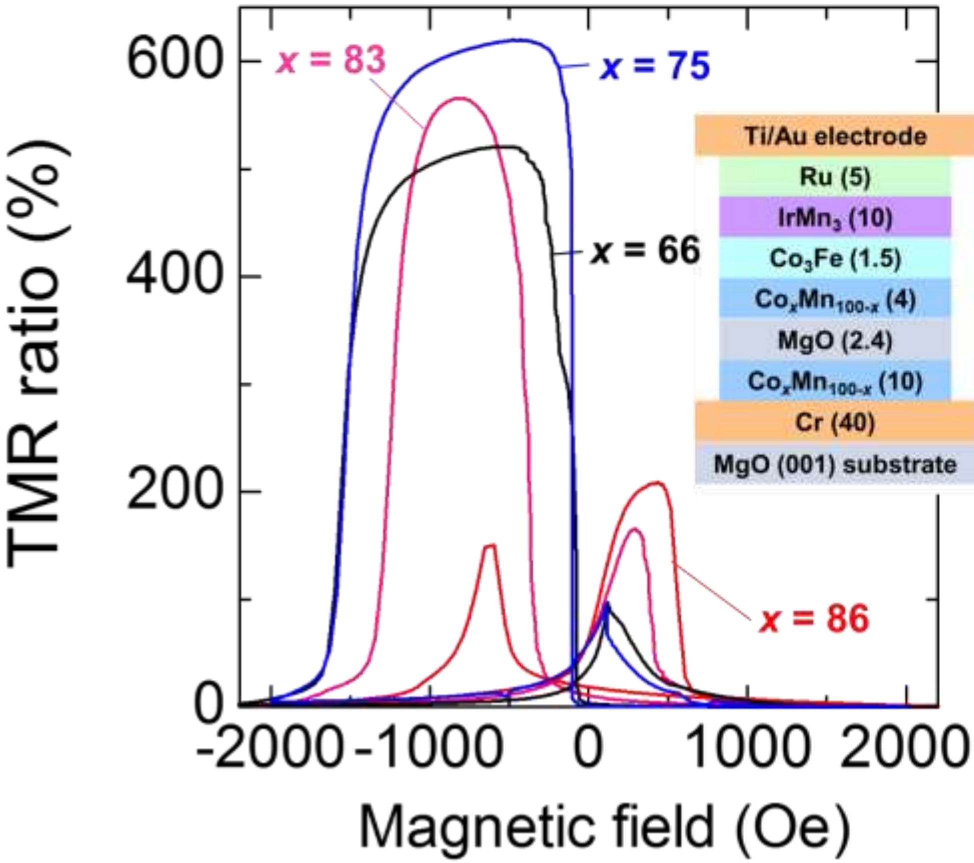

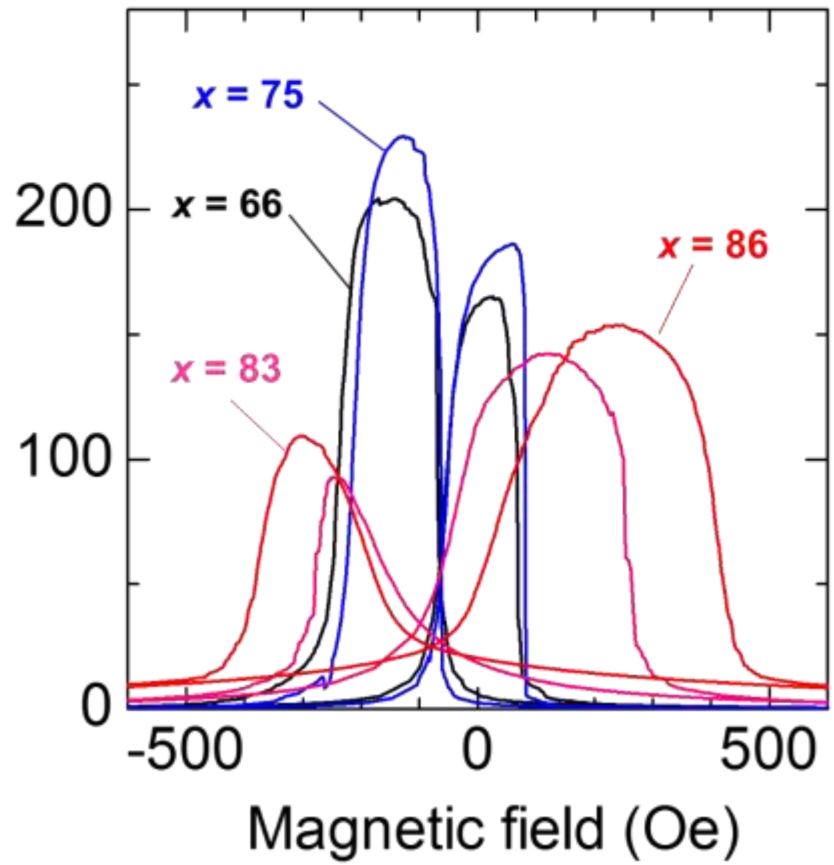

TMR Measurements

Conventional four-terminal measurements were used to evaluate TMR ratios :

- By fitting the data with Shang's model, * the TMR ratio are also found to satisfy the following relationship :

  $$G_{\mathrm{p\ (ap)}} = G_0(T)[1 + (-)P_0^2 m^2(T)] + G_{\mathrm{hop}}(T)$$

  where G_0 : mean conductance, P_0 : tunnelling spin polarisation, m : reduced magnetisation, G_{hop} : spin-independent conductance due to the two-step hopping via defect states in a MgO barrier.

  P_0 = 0.87 ($\times$ 2 of Fe/MgO/Fe MTJs)

  A = 1.7 $\times$ 10^{-5} $K^{-3/2}$

- Thus, the temperature dependence of the TMR ratios is mainly induced by

  spin fluctuation at the CoMn/MgO interfaces

  spin-independent hopping within the MgO barrier.

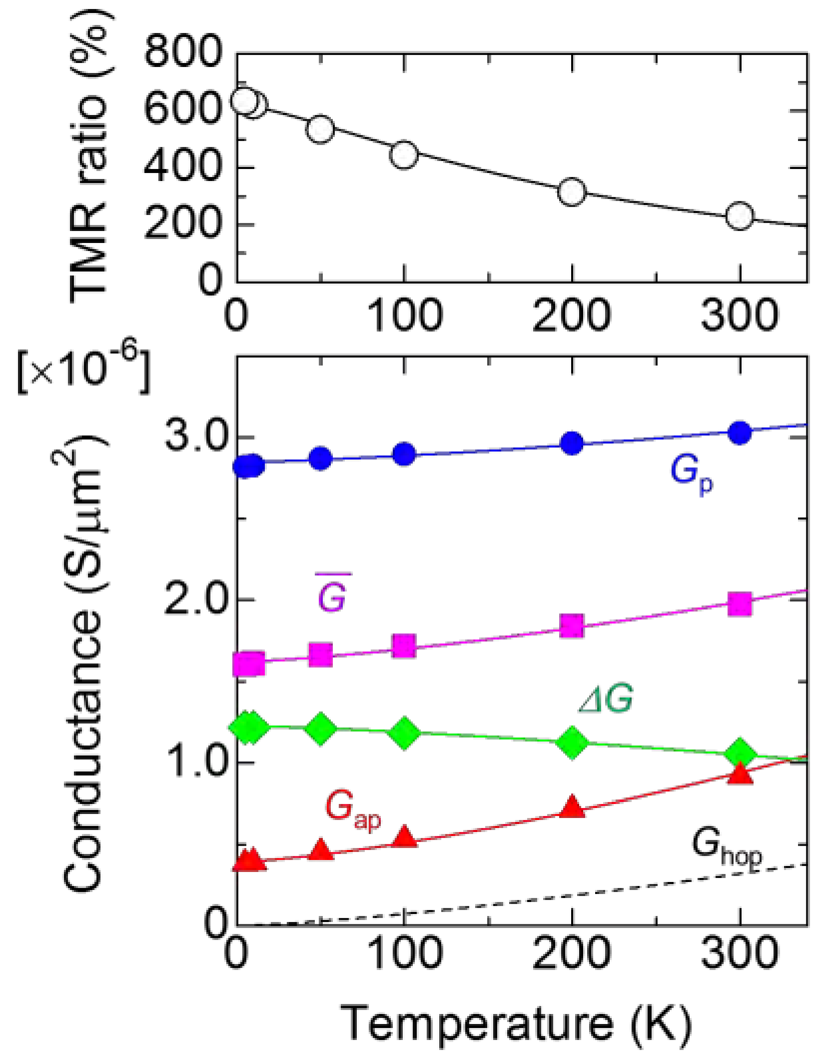

* C. H. Shang *et al.*, *Phys. Rev. B* **58**, R2917 (1998).

Cross-Sectional TEM Images

$Co_{86}Mn_{14}$ MTJs (x = 86) :

- The period of the lattice dislocation is calculated to be (8.9 ± 0.3) nm^{-1} for TMR ratio = 120%.

- Dark regions near dislocations are not fully crystallised (origin of spin fluctuation).

  Typically observed at the bottom CoMn/MgO interface.

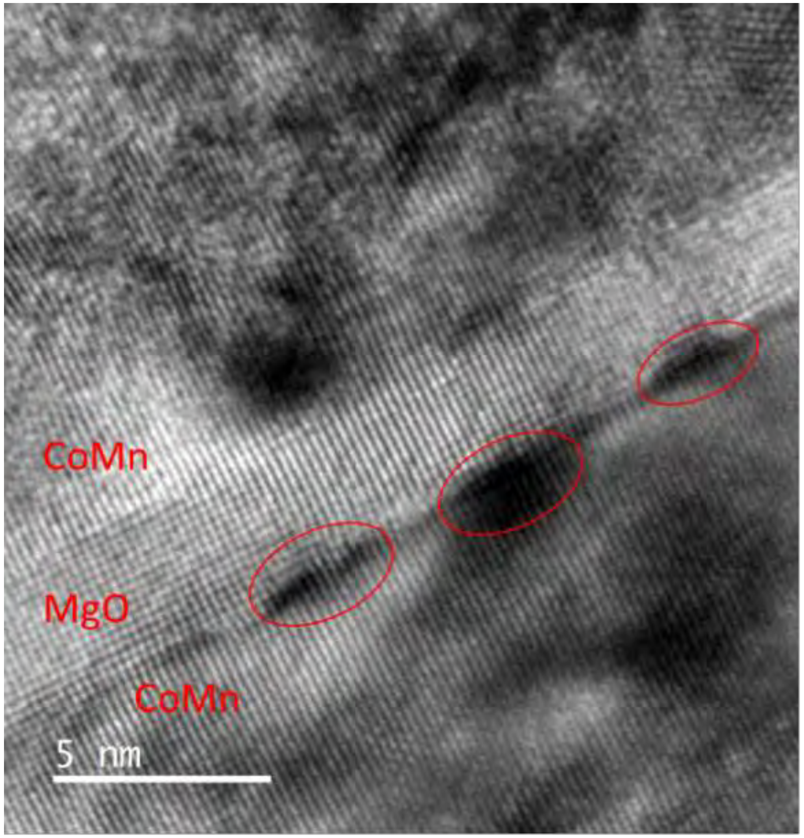

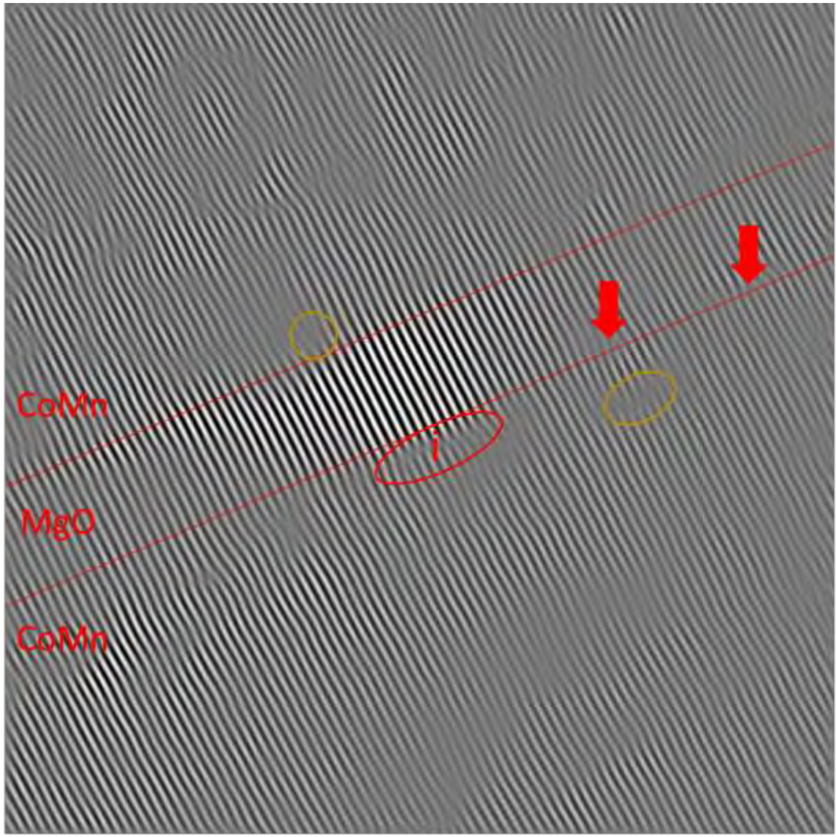

Cross-Sectional TEM Images

$Co_{75}Mn_{25}$ MTJs (x = 75) :

- The period of the lattice dislocation is calculated to be (11.4 ± 0.3) nm^{-1} for TMR ratio = 240%.

- Dark regions near dislocations are not fully crystallised (origin of spin fluctuation).

  Typically observed at both CoMn/MgO interface and within the CoMn layer.

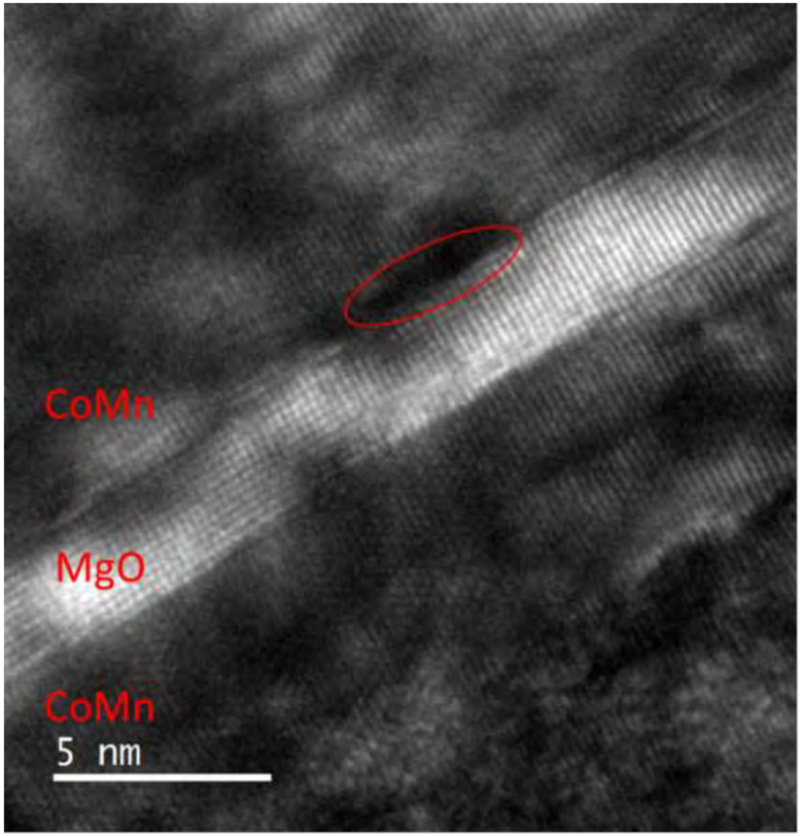

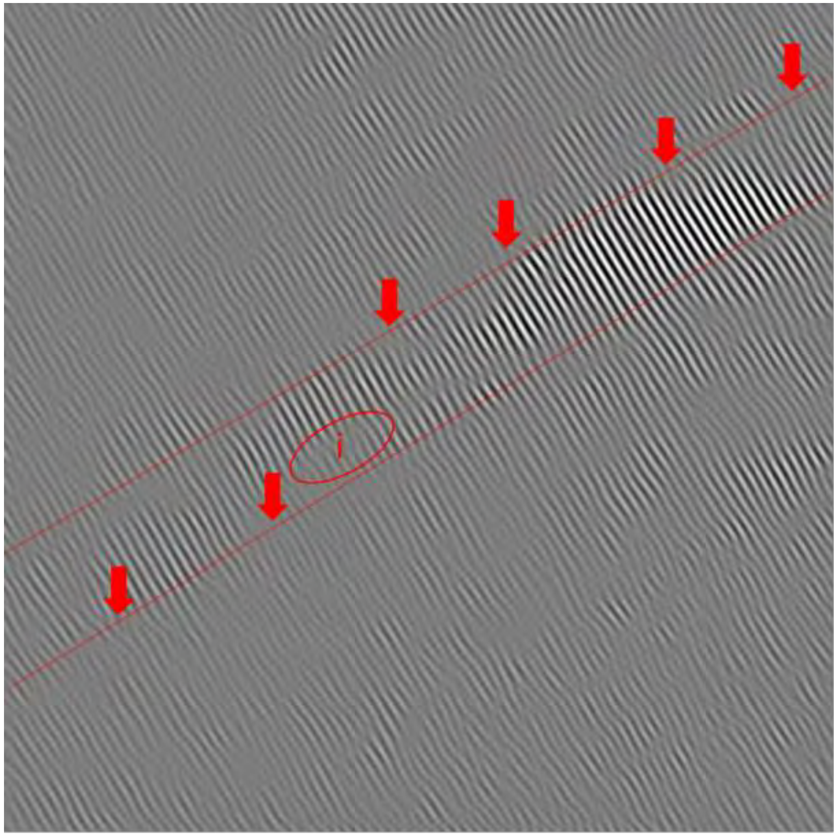

Cross-Sectional TEM Images

$Co_{75}Mn_{25}$ MTJs (x = 75) :

- There are stretched MgO regions found.

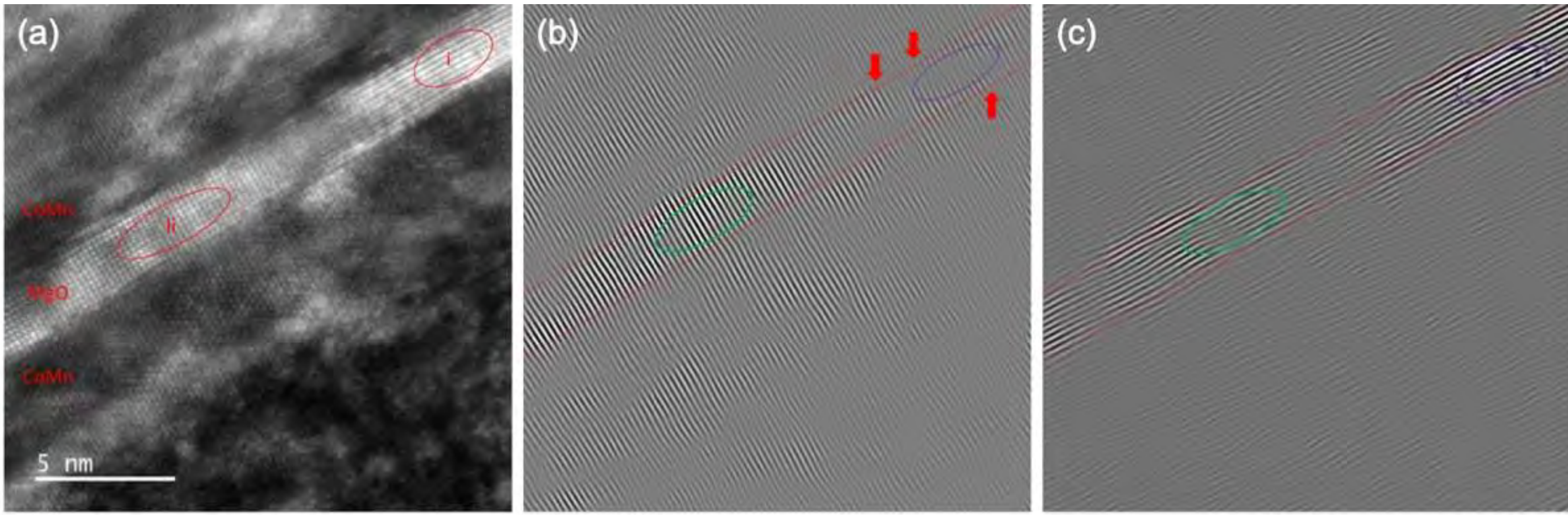

MgO [001]   MgO [100]

MgO Barrier Quality

MgO substrate/Cr (40)/CoMn (10)/MgO (20)/CoMn (4)/CoFe (1.5)/IrMn (10)/Ru (5) (thickness in nm) :

- Three distinctive regions in the MgO barrier :

  a : crystallised along the [100] direction.

  b : crystallised with different orientations (spin-independent hopping).

  c : partially crystallised (spin-independent hopping).

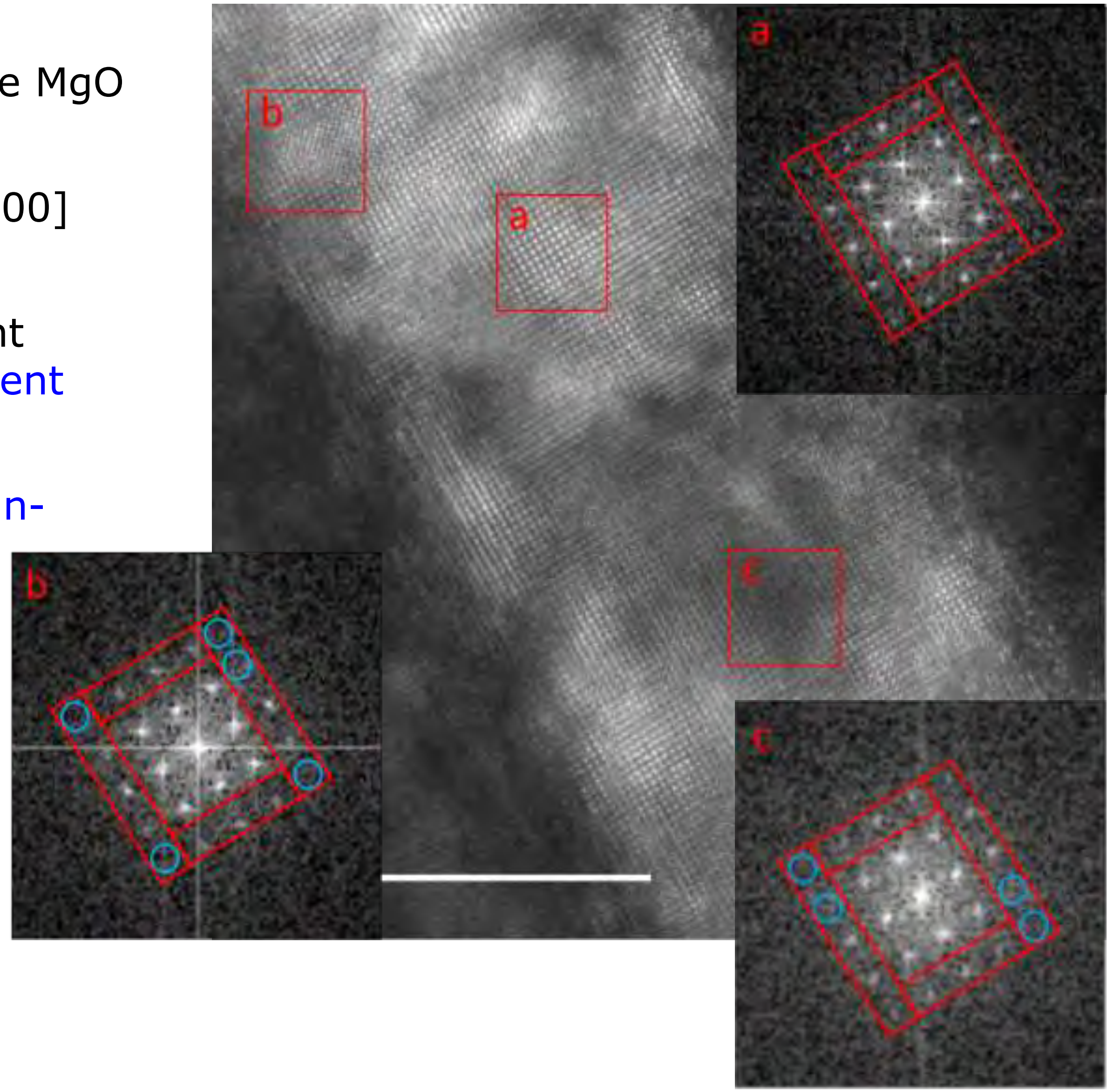

CoMn Lattice Constants

The lattice constants are calculated by measuring the averaged fringe distance across 20 layers in the corresponding TEM images :

- Apart from the *x* = 86, the top CoMn lattice constant is about 3.5% larger than the bottom layer across MTJs.

  The largest difference is 4.3% in *x* = 75.

  Almost constant lattice constants for the bottom CoMn layers except for that with *x* = 86.

  Dislocations may require to release the strain induced at the bottom CoMn/MgO interface as seen in TEM images.

  The number of dislocations almost stays the same except for *x* = 86.

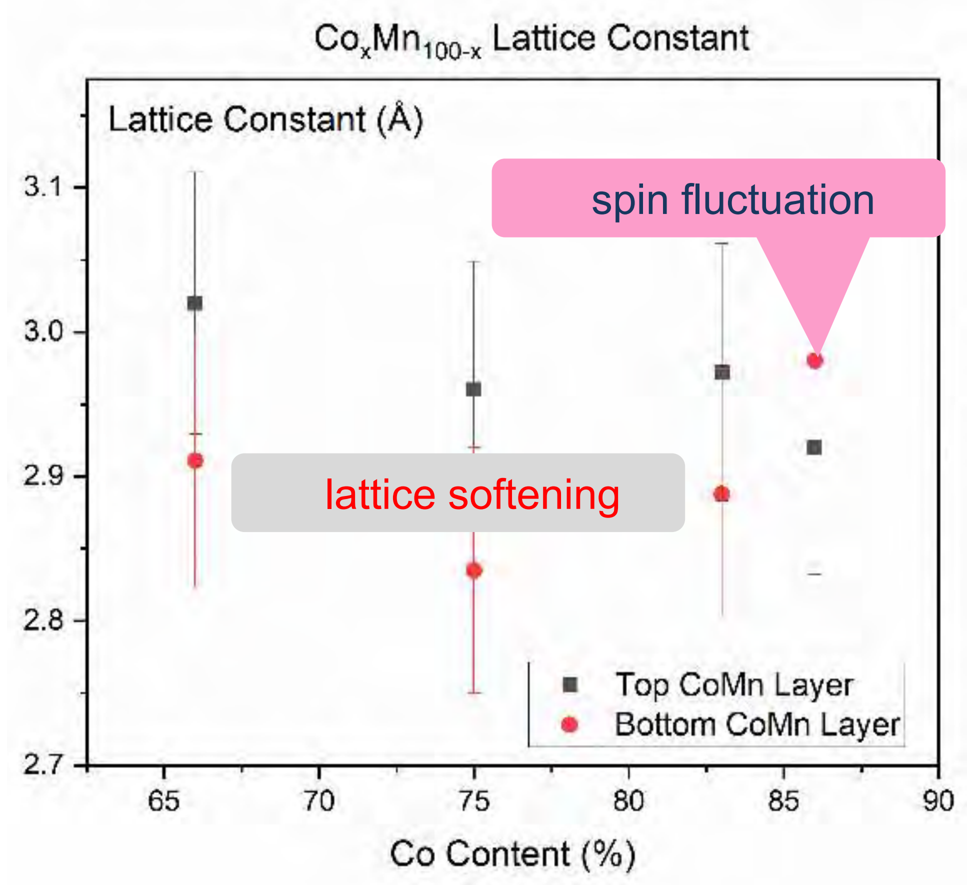

MgO Lattice Constants

The lattice constants are calculated by measuring the averaged fringe distance across 20 layers in the corresponding TEM images :

- Apart from x = 86, the MgO lattice constant is almost constant.
- The MgO lattice constant decreases only for x = 86.

  This agrees with the increase in the bottom CoMn lattice constant.

  This may induce more grains in the MgO barrier.

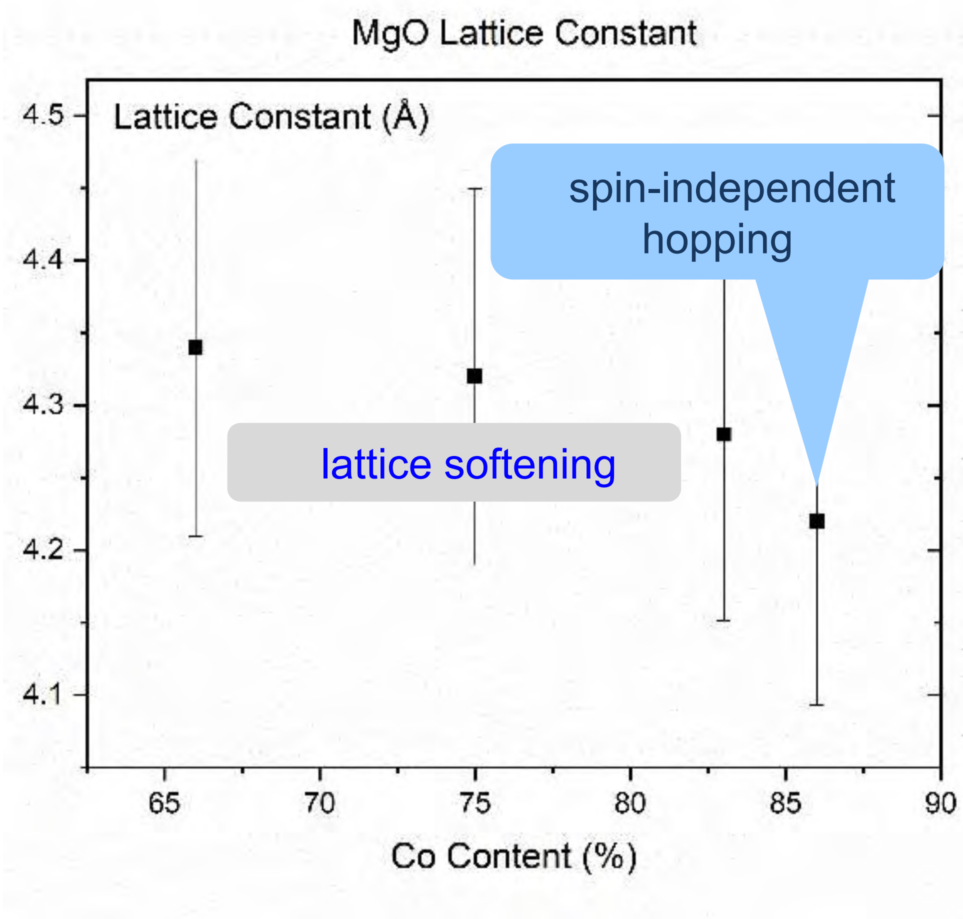

Ab-initio Calculations on Elasticity

Total energies of Co_xMn_{100-x} alloys are calculated as a function of the strain δ for tetragonal distortion :

- The bcc structure corresponds to $\delta = 0$.

- The use of a soft ferromagnetic layer can offer the precise lattice matching of a tunnel barrier with the neighbouring ferromagnets.

- A spinel barrier, of which lattice constant can be precisely controlled by its composition to match with that of the neighbouring ferromagnetic layers.

  TMR ratio = 342% at RT for a $Co_2FeAl/MgAl_2O_4/Co_2FeAl$ MTJ. *

- By employing $MgAl_2O_4$ tunnel barrier, further improvement in a TMR ratio can be expected.

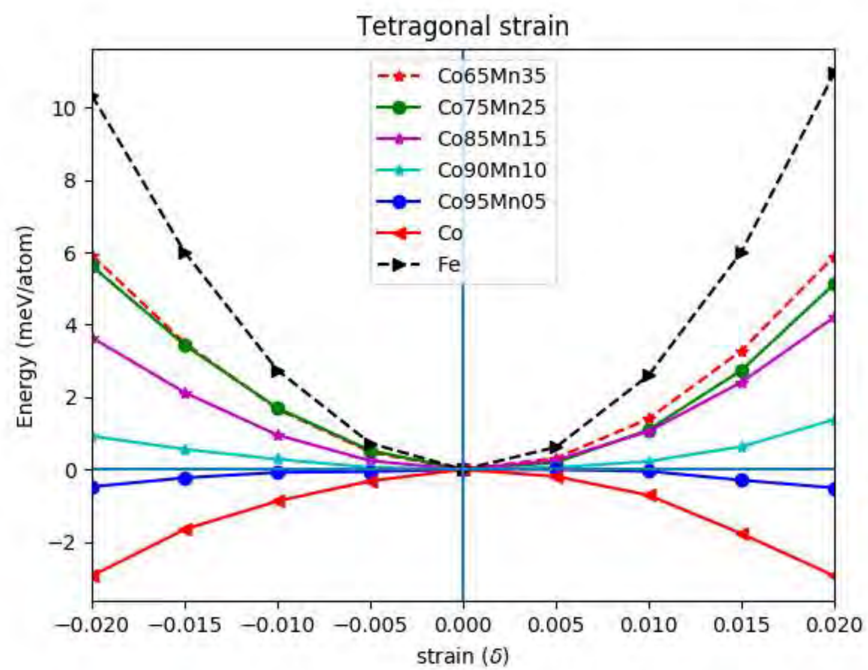

* M. Belmoubarik *et al.*, *Appl. Phys. Lett.* **108**, 132404 (2016).

Ab-initio Calculations on CoMn Lattice Softening

Tetragonal shear moduli C′ of ferromagnetic Co_xMn_{100-x} alloys as a function of the Co composition x :

- Softening of bcc Co_xMn_{100-x} becomes prominent near the boundary of the metastable bcc phase.

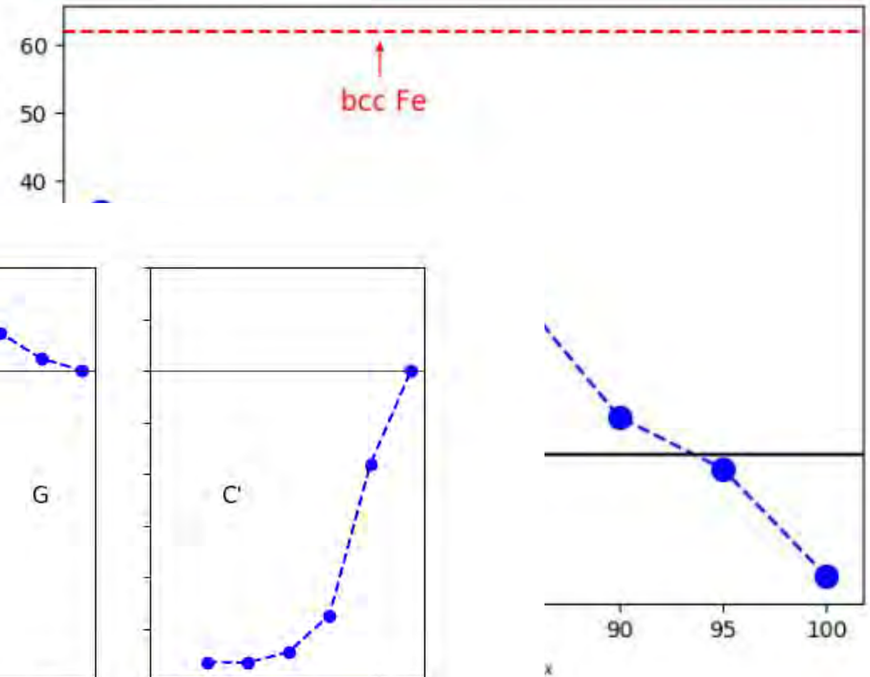

- Although the expected for stabilise a bc of MTJ.

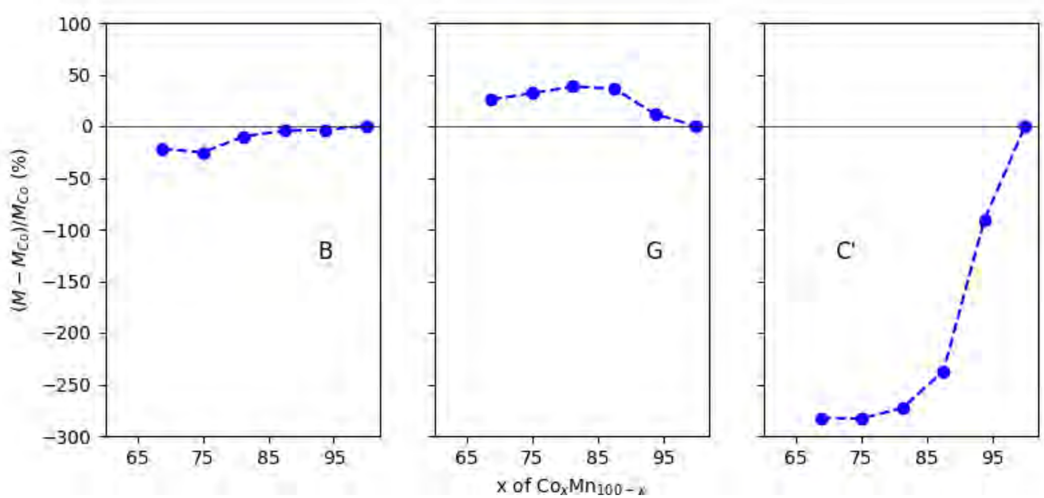

- This may lea potential of t improvemen magnetic tra

Ab-initio Calculations on CoMn Lattice Softening

Percentage change of the elastic modulus *M*, *i.e.*, the bulk modulus *B*, shear modulus *G* and tetragonal shear constant *C′*, with respect to that of Co M_{Co} : $(M - M_{Co}) / M_{Co}$ as a function of Co composition *x*.

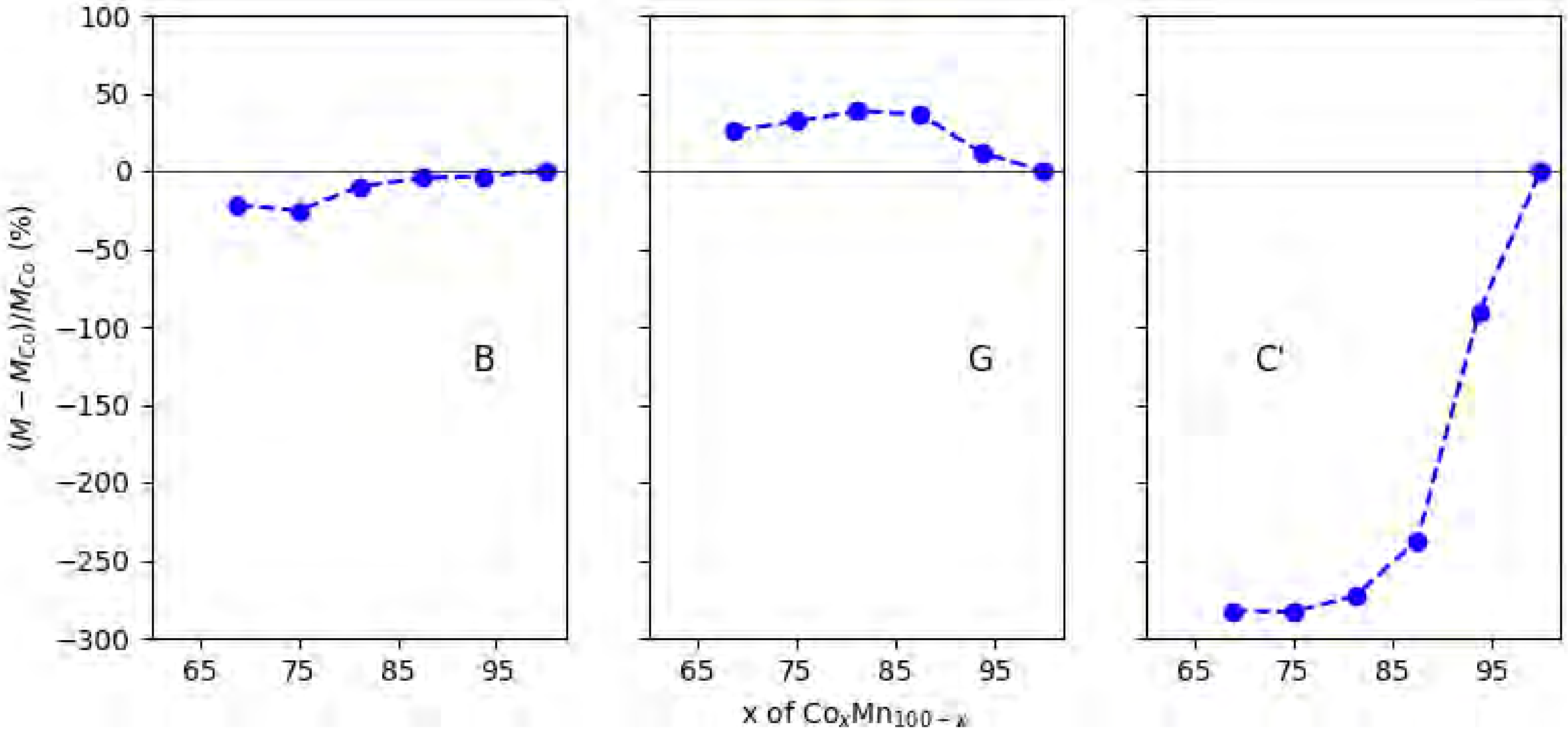

Current-Induced Magnetisation Reversal

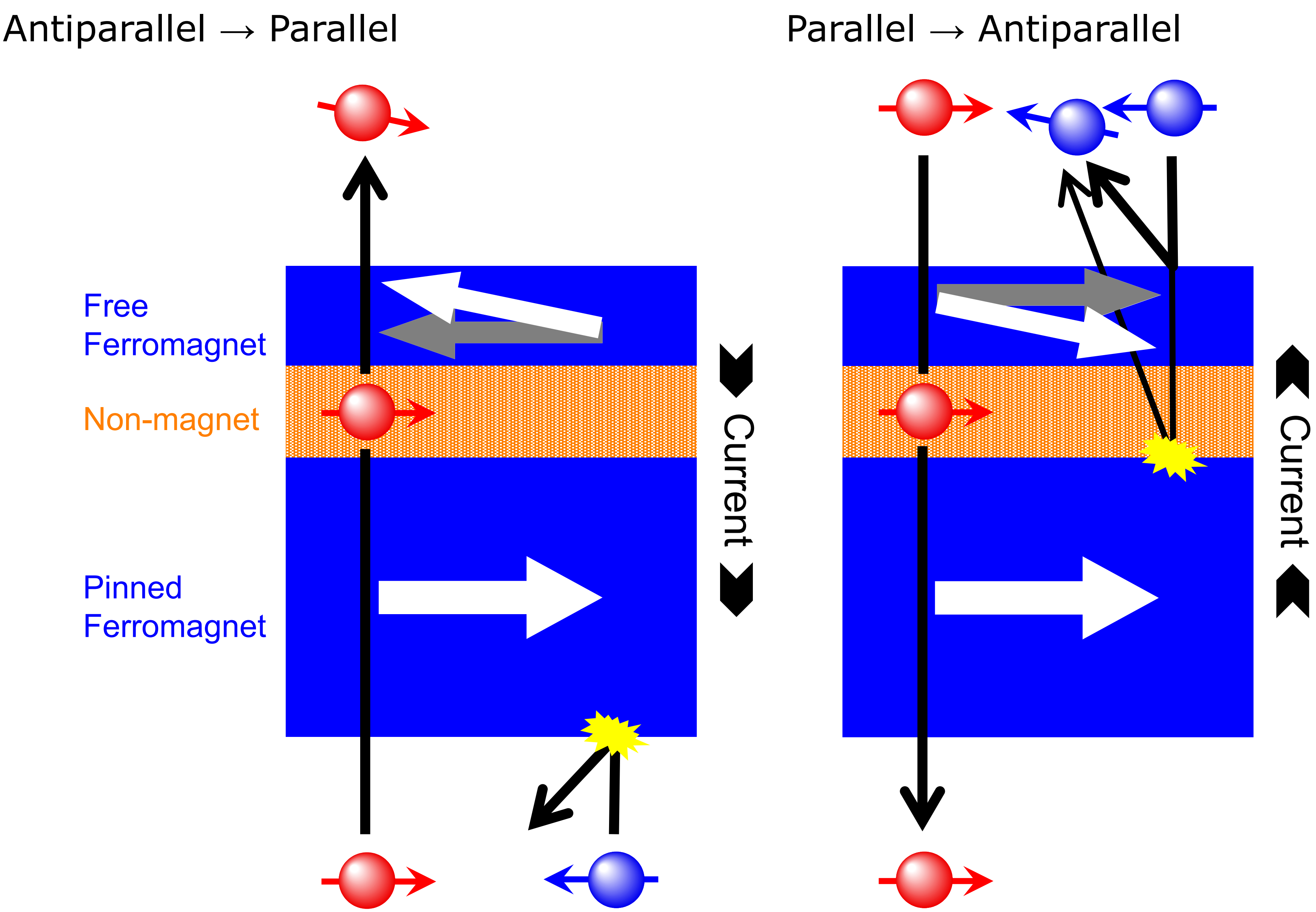

Current-Induced Magnetisation Reversal with Spin Wave

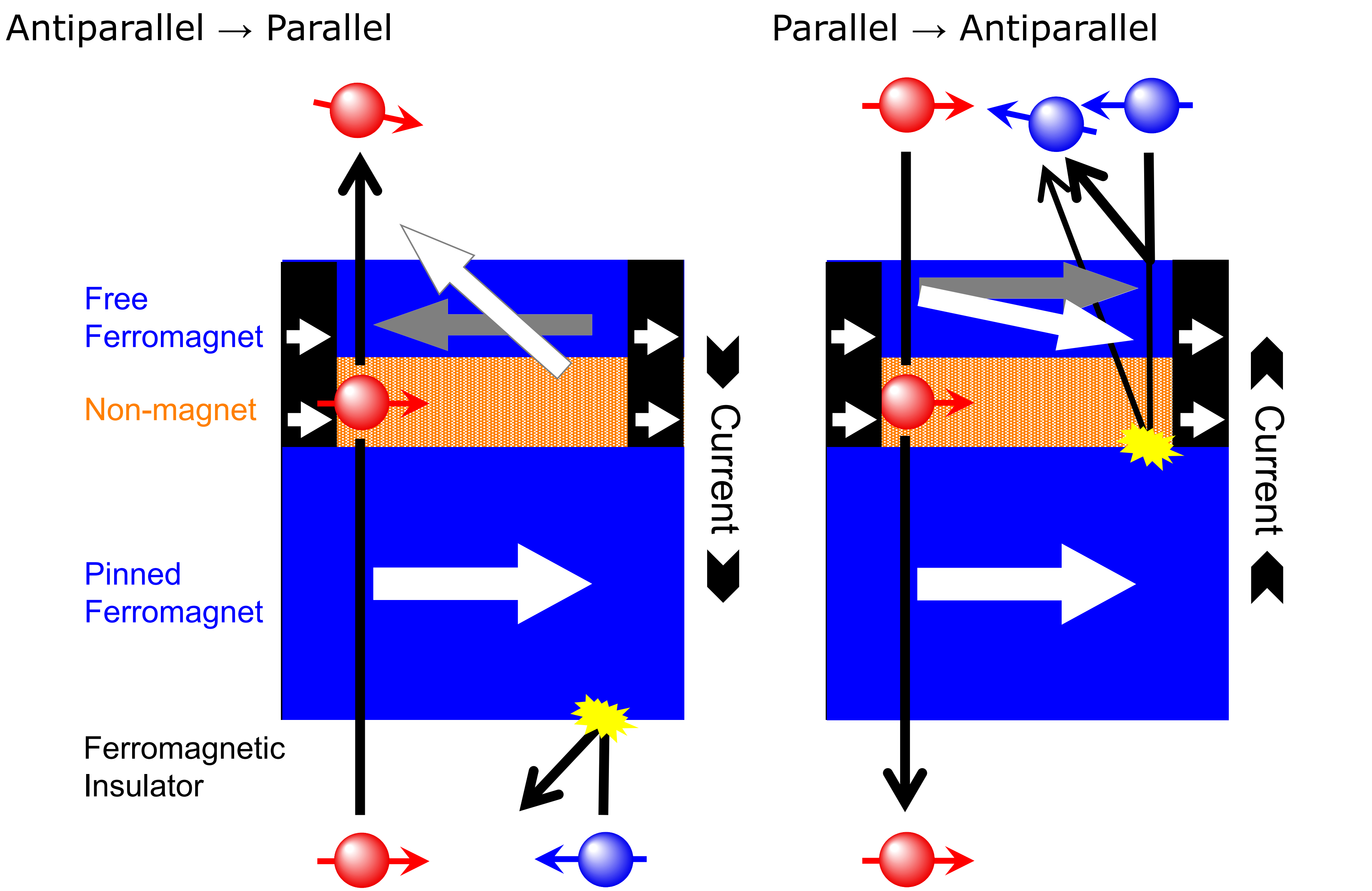

Heusler-Based Giant Magnetoresistive Junctions

$Co_2Fe_{0.4}Mn_{0.6}Si$ (CFMS) / $Ag_{0.78}Mg_{0.22}$ / CFMS junctions with Fe_2O_3 layers : *

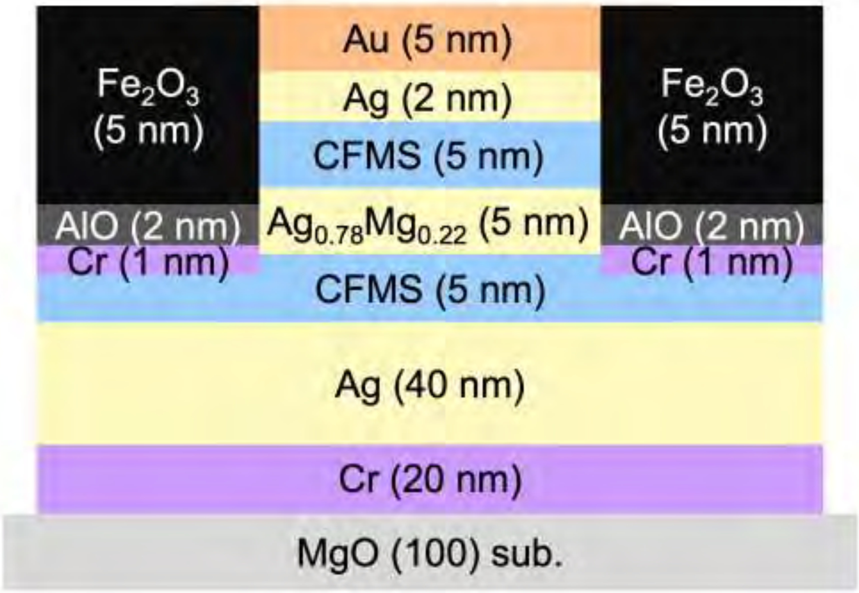

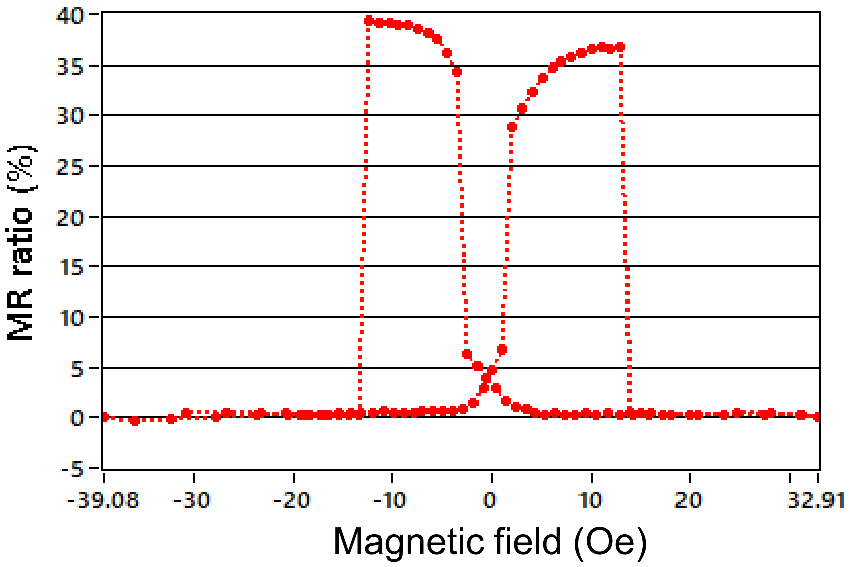

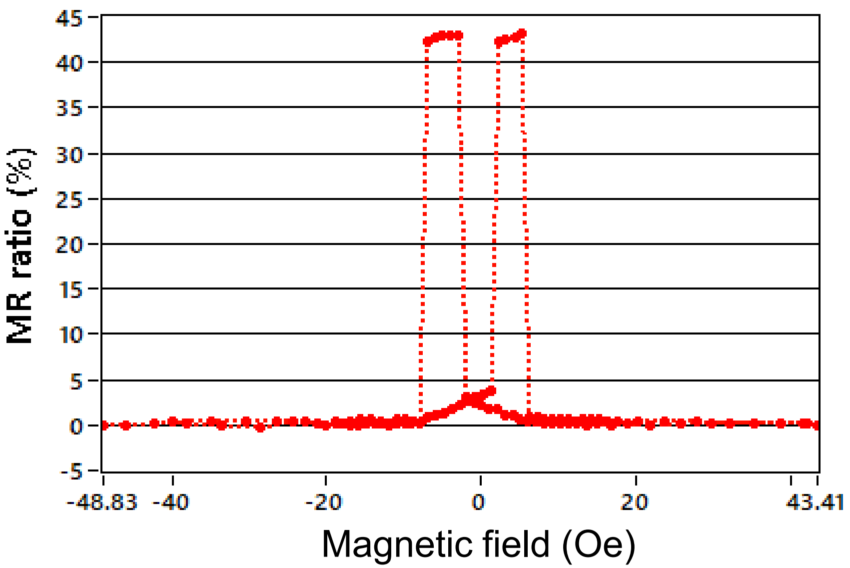

* T. Kubota *et al.*, *Phys. Rev. Mater.* **1**, 044402 (2017).

GMR Behaviour 1

CFMS / $Ag_{0.78}Mg_{0.22}$ / CFMS junctions with Fe_2O_3 layers :

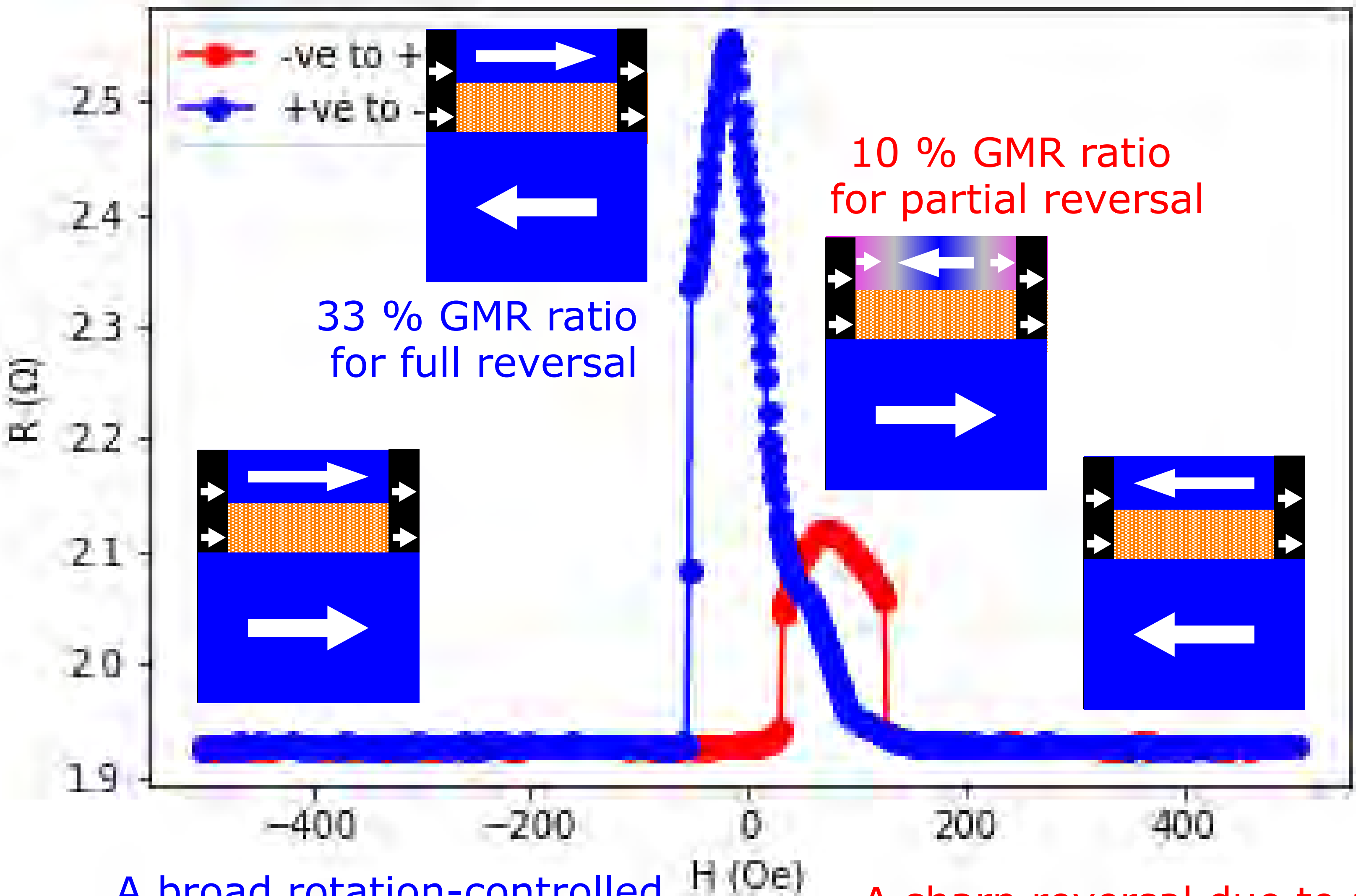

A broad rotation-controlled reversal followed by a sharper nucleation reversal.

A sharp reversal due to a single activation volume.

GMR Behaviour 2

CFMS / $Ag_{0.78}Mg_{0.22}$ / CFMS junctions with Fe_2O_3 layers :

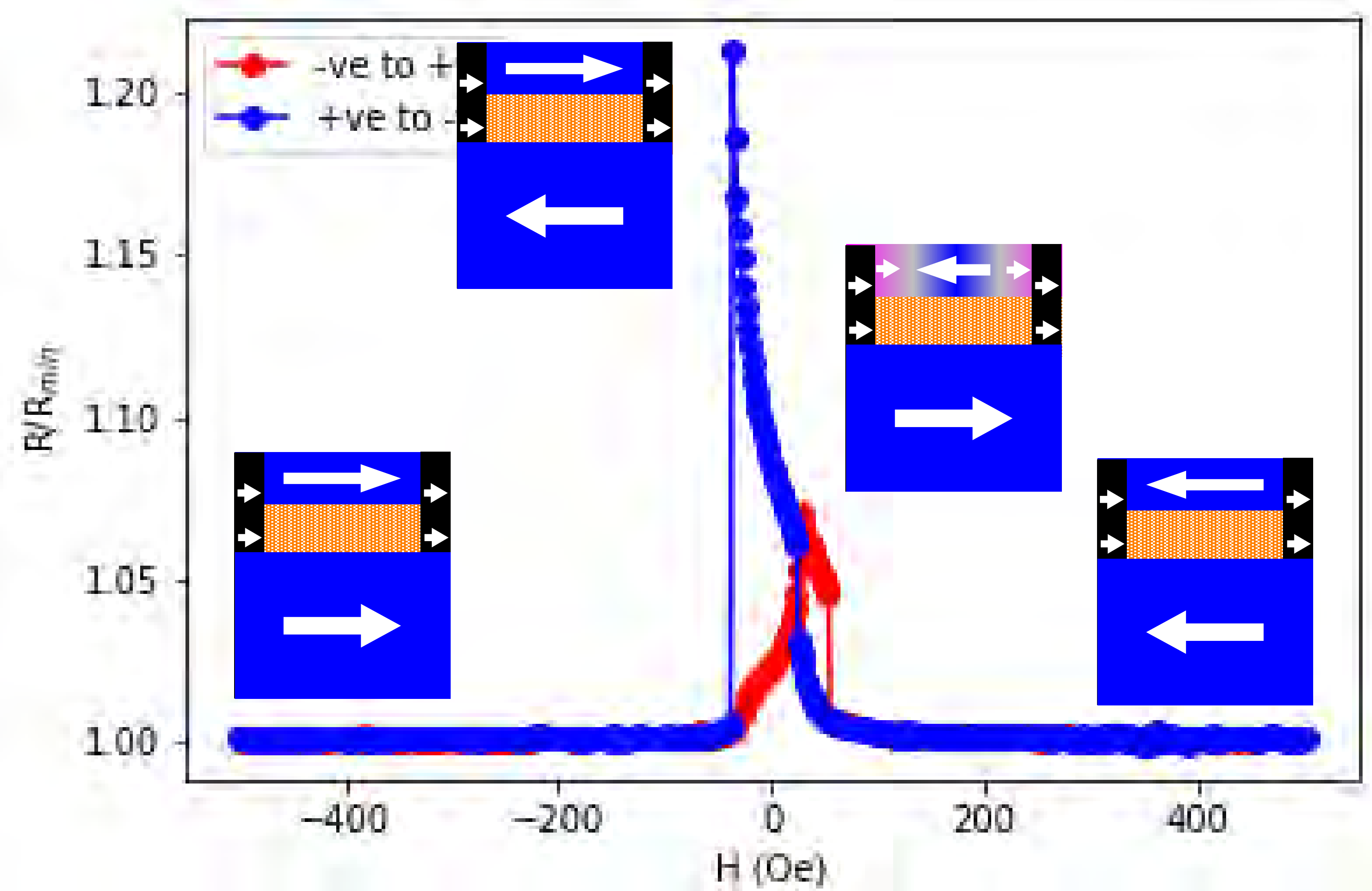

Current-Induced Magnetisation Reversal : Full AP → P

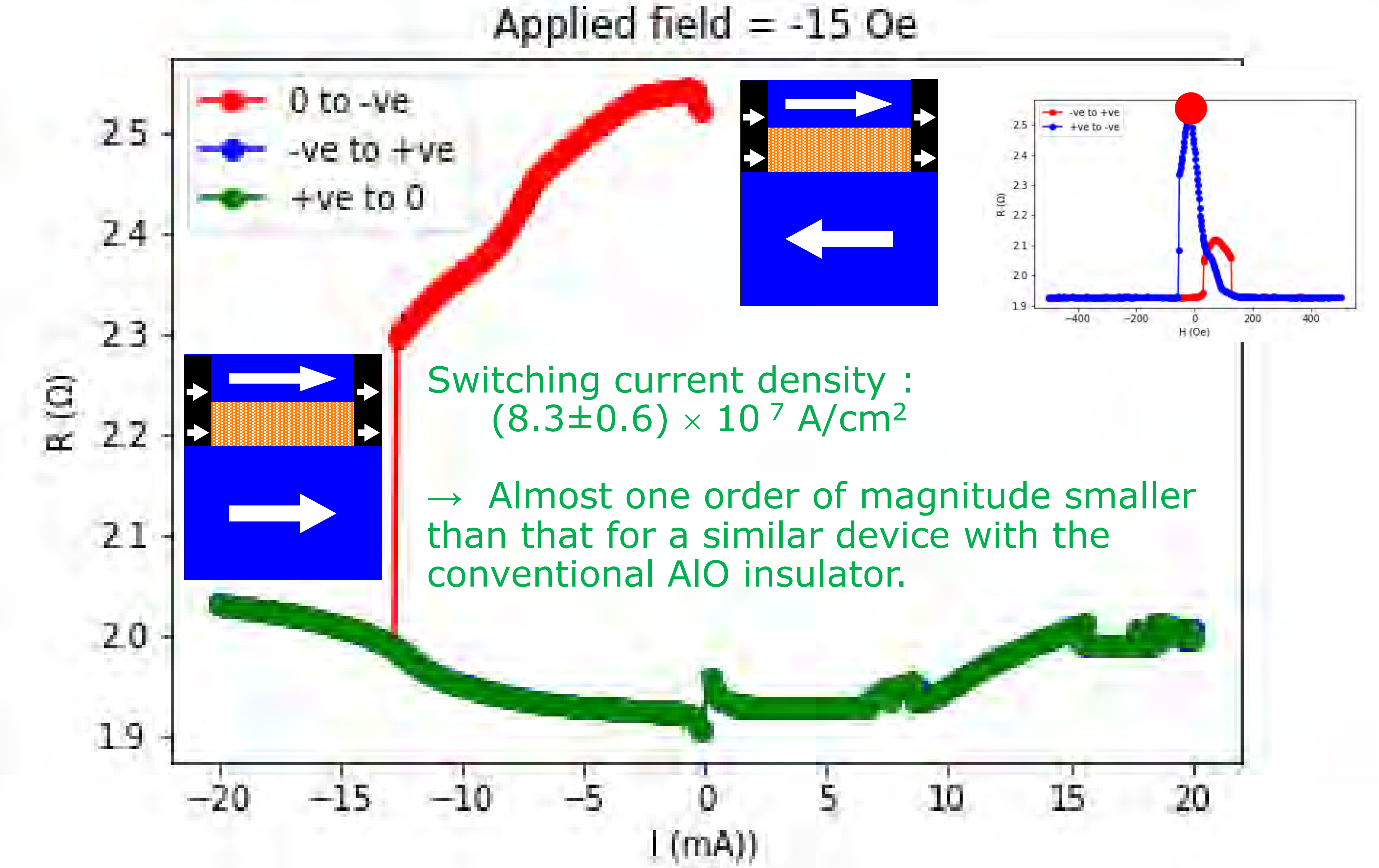

Switching current density :
(8.3±0.6) × 10 [7] A/cm²

→ Almost one order of magnitude smaller than that for a similar device with the conventional AlO insulator.

Current-Induced Magnetisation Reversal : Partial AP → P